UNIVERSITÀ DEGLI STUDI DI PADOVA

DIPARTIMENTO DI FISICA E ASTRONOMIA "G. GALILEI"

Corso di laurea Magistrale in Astronomia

Tesi di Laurea Magistrale

SEARCH FOR DARK MATTER ASSOCIATED WITH b QUARKS IN THE CMS EXPERIMENT

Relatore: Prof. Marco Zanetti

Laureando: Sara Leardini
Matricola: 1157071

Anno Accademico 2017/2018

Contents

Abstract

The quest for Dark Matter has become a paramount field of research in the last decades, which involves both astrophysicists and cosmologists, and particle physicists. Over the years, evidences from different cosmological and astrophysical sources added up to point out that something is missing from our theories: the flat rotational curves of spiral galaxies, the velocity dispersion of galaxies inside clusters, the flatness of the universe and many other phenomena show discrepancies between observations and current theories. The explanation for this discrepancy could either be that there must exist some extra matter, or that gravitational theories must be modified to account for all the unexplained phenomena. Both hypotheses are being investigated by scientists, however in this work the first assumption will be considered; in fact, the possiblity of extra matter existing opens an exciting window on the opportunity of discovering *new physics* beyond the Standard Model of Particle Physics. Following this direction, there are many particle candidates to investigate: WIMPs (weakly interactive massive particles), which remarkably provides the right relic density to explain astrophysical and cosmological observation at the right energy scale to solve SM gauge hierarchy problem; SuperWIMPs, Sterile Neutrinos, Axions, whose existence was postulated to solve other problems of the Standard Model. Next to the efforts of theorists to provide suitable particle candidates, a lot of experiments have blossomed, which try to attack the problem from different approaches: the search for DM collisions against ordinary matter (direct detection experiments, such as DAMA/NaI, XENON1T, CoGeNT, ADMX), the search for DM annihilations (indirect detection experiments, such as PAMELA, Amanda, IceCube), or the attempt to produce Dark Matter through collisions of SM particles (goal that is pursued at LHC). In this spirit, this work focuses on the research for Dark Matter through production at the LHC collider, operating at CERN, whithin the CMS experiment.

This work aims to analyze data from 2016 run at a center of mass energy of 13 TeV, conveniently selected to be good candidates for a DM production event: indeed, the signature that was looked for was a large amount of missing transverse momentum, since DM is supposed not to leave a signal in the CMS detector, leading to an imbalance in the sum of all the detected

particles' momenta. More in details, only events associated with the production of one or two bottom quarks were selected, in order to exploit possible Yukawa interactions between SM particles and the mediator which couples them to DM: in fact, Yukawa interactions are known to be stronger with heavy quarks than with light ones. What was practically performed was an additional selection among the collected events other than the preliminary one made by CMS's triggers; after normalizing the MonteCarlo samples simulating the backgrounds of the probed process with the help of some control regions, suitable candidates for the production of Dark Matter were compared with SM predictions, in order to look for possible deviations.

In Chapter 1 physical motivations behind Dark Matter will be explained, both from the Astrophysics/Cosmology's and the Particle Physics's point of view. Moreover, the main candidates to be Dark Matter particles will be described, together with the experimental techniques that are exploited. Chapter 2 will focus on the CMS experiment, providing an insight into the hardware and software components of the detector and a review of analyses performed by the CMS group on previous datasets. Finally, in Chapter 3 and in the Conclusions, the analysis of events collected in 2016 run associated with beauty quarks will be reported, and the results will be discussed.

Chapter 1

An introduction to Dark Matter

In this Chapter, the evidences for Dark Matter in different branches of Physics will be presented: there are indeed open problems in Cosmology, Astrophysics and Particle Physics which could be solved through the discovery of Dark Matter. This will be the main focus of Section 1.1. After discussing the scientific motivations, some possible candidates for Dark Matter particles will be presented (Section 1.2) and the experimental attempts to discover them will be described (Section 1.3). It must be mentioned that there are alternative hypotheses to explain the cosmological and astrophysical anomalies which modify the Theory of gravity instead of postulating the presence of extra matter (e.g. MOND). However, they have some troubles in accounting for all the phenomena and to describe them would go beyond the scope of this thesis. For these reasons, the description below will be limited to solutions that require the presence of extra matter.

1.1 Motivations for Dark Matter

1.1.1 Evidences from Astrophysics and Cosmology

The first evidence for the possible presence of a large amount of non-luminous matter dates back to 1933, when Fritz Zwicky noticed that the velocity dispersion of galaxies in the Coma Cluster was too large to be related only to the observable matter. In fact, he applied the virial theorem to the galaxy of the cluster

$$E_K = -\frac{1}{2}E_P \Rightarrow \frac{1}{2}Mv^2 = \frac{3GM^2}{2 \cdot 5R} \tag{1.1}$$

setting the mass M equal to the amount of observed luminous matter ($1.6 \cdot 10^{45}$ g) and the radius R equal to 10^{24} cm. This way he obtained for the velocity dispersion $v = 80$ km/s, a value more than an order of magnitude

smaller than the observed value of 1500-2000 km/s (Zwicky, 1933).

Clusters of galaxies provide another evidence for the presence of Dark Matter if we consider the strong lensing effect: light coming from far sources is bent if it crosses clusters of galaxies, producing effects such as arcs, rings, magnification of the images and multiple images. The magnitude of this bending allows to estimate the amount of matter contained in the cluster: if we consider a source that is aligned with the lens (the cluster in this case) with respect to the observer, it will be transformed into a ring by the strong lensing effect; hence, we can define the *Einstein radius* θ_E as the angular radius of the ring. The mass distribution of the cluster can be obtained by inverting the relation:

$$\theta_E = \sqrt{\frac{4GM}{c^2 D}} \tag{1.2}$$

where $D = D_{OS}D_{OL}/D_{LS}$ depends on the distances between the observer and the lens (D_{OL}), between the observer and the source (D_{OS}), and between the lens and the source (D_{LS}). This kind of study has been enhanced by the high-quality images provided by the Hubble Space Telescope (see Fig. 1.1 for an example of lensed galaxies). It is clear from the study of strong lensing that clusters are dominated by the presence of dark matter.

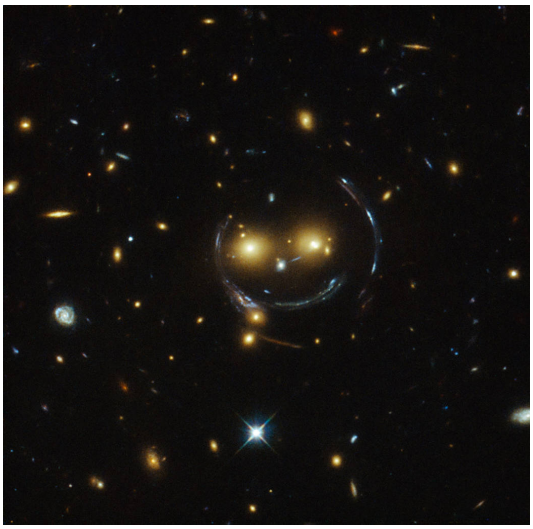

Figure 1.1: Image by the HST of the "Cheshire Cat": background galaxies are lensed by the galaxy cluster SDSS J1038+4849. Image Credit: NASA/ESA.

Another hint for the existence of extra matter, on the galactic scale, came with the study of the rotation curve of the Andromeda galaxy (M31): if the rotation followed a keplerian law, in the outer parts of the galaxy the velocity should decrease as $r^{-1/2}$; what is observed instead is a flat rotation curve (Fig. 1.2).

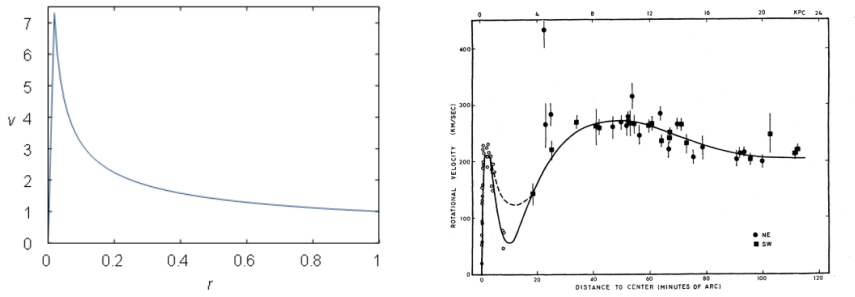

Figure 1.2: On the left, simulated rotation curve of a galaxy with a keplerian law at large radius (image by Schwarzmeier). On the right, observed rotation curve for M31 (Rubin & Ford, 1970).

Such flat rotation curve could be obtained if there existed a mass distribution with a density $\propto r^{-2}$ of non-luminous matter.

Cosmology provides other reasons to postulate the existence of Dark Matter. At present days, the Standard Model in Cosmology is the ΛCDM model, that is, a model with Dark Matter and a cosmological constant Λ, which is responsible for the accelerated expansion of the Universe (also known as the Dark Energy). The density parameters for the universe, according to the ΛCDM model, are (see Planck collaboration, 2016):

- Density parameter for baryonic matter: $\Omega_B = 0.0486 \pm 0.0010$
- Density parameter for dark matter: $\Omega_{DM} = 0.2589 \pm 0.057$
- Density parameter for dark energy: $\Omega_\Lambda = 0.6911 \pm 0.0062$

Within this model the presence of Dark Matter can be inferred from the study of the Cosmic Microwave Background (CMB) anisotropies. Indeed, the CMB is a perfect black body spectrum only at a first approximation; actually small temperature fluctuations $\Delta T/T$ can be observed (Figure 1.3, left), whose magnitude is of the order of 10^{-5}, varying slightly with the angular scale considered. In order to study the fluctuations, since they are seen as projected on the celestial sphere, we can write them as:

$$\frac{\Delta T}{T}(\theta, \phi) = \sum_{l=0}^{\infty} \sum_{m=-l}^{l} a_{l,m} Y_{lm}(\theta, \phi) \tag{1.3}$$

where $Y_{lm}(\theta, \phi)$ are the spherical harmonics, while θ and ϕ are respectively the polar and the azimuthal angle; $l \geq 0$ and $m = -l, ..., l$; l is called *multipole moment* and is inversely proportional to the angular scale under consideration. If we assume gaussianity for the temperature fluctuations,

given a value for the multipole l, the average of $|a_{l,m}|^2$ over every possible value of m yelds the temperature fluctuation amplitude A_l as a function of l, that is, the power spectrum; usually what is shown is the product $A_l \cdot l(l+1)/2\pi$ against l (Figure 1.3, right). The fit of the power spectrum provides a remarkable evidence for the existence of Dark Matter: by changing the density of dark matter in the universe, which enters as a parameter into the fit, the best-fit confirms the predictions for Ω_{DM} of the ΛCDM model (see Figure 1.4): indeed, the ratio between the amplitude of the second and the third peak provides the ratio between the mass density of ordinary and Dark matter. The analysis of the power spectrum is also a remarkable constrain to the curvature of the universe, which is consistent with the hypothesis of a flat universe ($\Omega_B + \Omega_{DM} + \Omega_\Lambda = 1$).

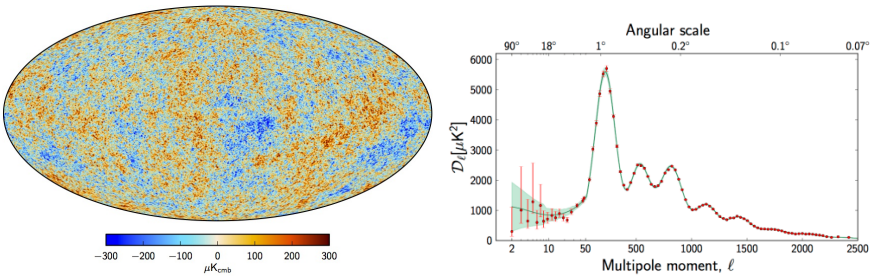

Figure 1.3: On the left, a map of the CMB, as observed by the Planck satellite; the temperature fluctuations that are shown are relative to the average temperature of the CMB. On the right, the power spectrum of the CMB as a function of the multipole l (Planck collaboration, 2015).

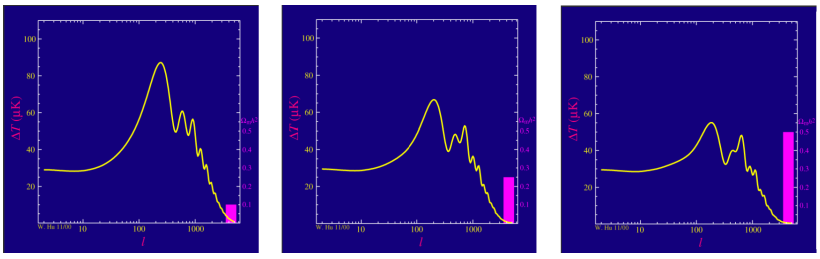

Figure 1.4: Variation of the CMB power spectrum when the physical density of Dark Matter is changed: when the density increases, the peaks diminish their intensity; moreover, the position of the first peak switches towards the right, indicating that the universe decreases its curvature (images from Hu, http://background.uchicago.edu/∼whu/intermediate/driving2.html).

Moreover, from a cosmological point of view Dark Matter is necessary to explain the formation of structures in the universe. Up-to-date theories explain the formation of the large scale structure of the universe as the consequence of small density perturbations in the primordial cosmic fluid. Nevertheless, baryons could not grow perturbations before the recombination era, at

redshift z $\sim$ 1100. Since in the present universe the density fluctuations $\delta\rho/\rho \gg 1$, if we consider that $\delta\rho/\rho \propto (1+z)^{-1}$ and that $\delta T/T \propto \delta\rho/\rho$, to account for the formation of structure only with baryonic matter we should have temperature fluctuations of the order of 10^{-3}, much greater that the ones which are observed!

Another constraint for baryonic abundance, and consequently for DM abundance, comes from Big Bang Nucleosynthesis, one of the biggest successes of ΛCDM mode (developed first by Wagoner et al., 1967); this theory basically explains what happened in the era between the decoupling of hadrons from the cosmic fluid until the formation of the first light elements. The main phases are the following ones: when the universe is cool enough (T$\sim 10^{13}$ K) hadrons decouple from photons, starting the so-called *lepton era*. The remaining protons and neutrons keep being in equilibrium through weak reactions, but as temperature decreases, protons start to outnumber neutrons, because of their mass difference, which favors reactions that turn neutrons into protons. When leptons decouples from photons, too, weak reactions are also suppressed, with the exception of β decay of neutrons; nevertheless, the temperature becomes low enough (T$\sim 10^9$ K) to start trapping neutrons into atomic nuclei, through the reactions:

1. n+p$\rightarrow{}^2$D+γ
2. ^{2}D+^{2}D$\rightarrow{}^3$He+n
3. ^{3}He+n$\rightarrow{}^3$H+p
4. ^{3}H+^{2}D$\rightarrow{}^4$He+n

The efficiencies of these reactions depend on the baryon density which, therefore, affects also the abundances of some light elements, e.g. Lithium, Deuterium, ^{3}He: if the universe is very dense, the efficiencies are very high, and we expect to see all the deuterium to be turned into ^{4}He; vice versa, in a low-density universe we should observe some residuals of light elements other than ^{4}He (Figure 1.5). By measuring the abundances of these elements in the present universe, the baryon density can be estimated, leading to a value of $\Omega_B \sim 0.04$ (Undagoitia & Rauch, 2017), very low with respect to the estimated value of $\Omega \sim 0.3$ for gravitating matter.

To conclude this excursus about Astrophysics and Cosmology, it is worth to mention a remarkable evidence for the existence of Dark Matter which comes from the *Bullet Cluster*: Clowe et al. (2006) observed a cluster merger both in optical and in x-ray light. The optical observations showed lensing effects on the background galaxies, allowing to estimate the amount and the distribution of mass in the clusters, while the x-ray images revealed the

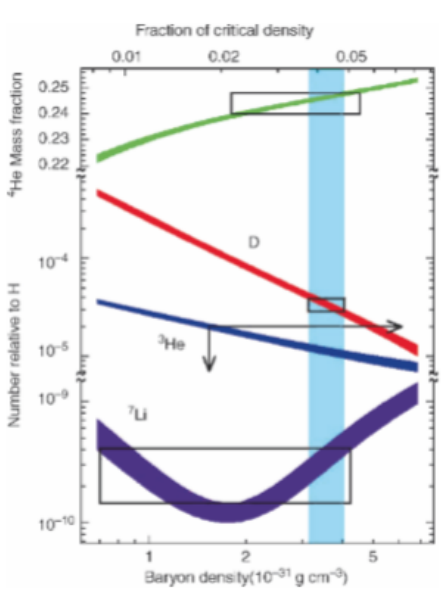

Figure 1.5: Variation of light elements' abundances as a function of baryonic density: red, blue and violet curves are relative to the abundance of, respectively, Deuterium, ^{3}He and Lithium, with respect to the abundance of Hydrogen; the green line shows the trend of ^{4}He mass fraction (Schneider, 2006).

presence and the position of plasma clouds belonging to the two clusters. The amount of matter constituting the plasma (and the galaxies) is not enough to explain the observed lensing effect; hence, what can be inferred is that the clusters are made of two main components: the hot gas, that slowed down due to electromagnetic interactions, and Dark Matter, which could cross the other cluster quite unperturbed (Fig. 1.6). The behaviour of Dark Matter in crossing Bullet Cluster allows to set an upper limit to self-interaction of DM particles, that is a cross section $\sigma_{self}/m_{DM} = 2$ barn/GeV (Gelmini, 2015).

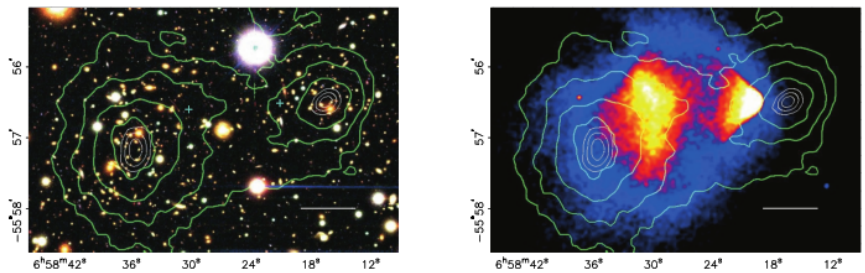

Figure 1.6: On the left, optical image of the bullet cluster. On the right, x-ray image of the same cluster (Clowe et al., 2006).

1.1.2 Motivations from Particle Physics

Even if not directly related to the search for Dark Matter, there are some open problems in Particle Physics that require physics beyond the Standard Model (SM). Some of the solutions proposed could, at the same time, provide the new particle that explains the astrophysical and cosmological observations presented in the previous Section. Following the paper by Feng (2010), here follows a list of the open problems, specifying whether the phenomena cannot be explained by the SM, or they could be explained within the SM with an "unnatural" choice of parameters:

- The gauge hierarchy problem: the existence of gravity provides a universal regulator scale. Indeed, to have a quantum elementary particle, its Compton wavelength must be bigger than its gravitational radius; this limit depends, for General Relativity, on the Planck Mass $M_P \sim 10^{19}$ GeV: no elementary particle can have a mass which exceeds this value (Dvali, 2013). The existence of this limit raises the question: why is the mass of the Higgs boson so much smaller than M_P? Moreover, the mass of the Higgs is the sum of the tree-level mass and the corrections at the loop level: $m_h^2 = m_{h,tree}^2 + m_{h,loop}^2$, where $m_{h,loop}^2$ depends quadratically on the energy scale Λ at which the SM ceases to be valid. If the energy scale is of the order the Planck mass, a fine-tuning would be required to obtain the Higgs mass $m_h = 125$ GeV. The possible solutions (e.g. some energy scale $\Lambda \ll E_P$ at which the SM is not valid anymore, or considering the Higgs boson a composite particle) require a physics beyond the SM at the weak scale (Feng, 2010).

- The new physics flavor problem: an interaction is *flavor changing* if the flavor numbers of the particles involved at the end of the interaction are different from the flavor numbers at the beginning. Charged currents, which involve at the same time up-type and down-type quarks, or charged and neutral leptons, can change flavor at the tree level; on the contrary, flavor changing neutral currents (FCNC), which couple only up-type or down-type quarks, and only charged or neutral leptons, were observed only at the loop level. Some diagrams of FCNC processes are reported in Figure 1.7. If there exists new physics at the weak scale to fix the gauge hierarchy problem, in principle it may produce FCNC processes at the tree level, but in fact it does not: why do such processes not occur?

- The neutrino mass problem: in the SM neutrinos appear only with left chirality. To get a mass through the Higgs mechanism, though, the right- and left-handed terms have to be coupled: hence, in the SM neutrinos are massless particles. Nevertheless, the discovery of

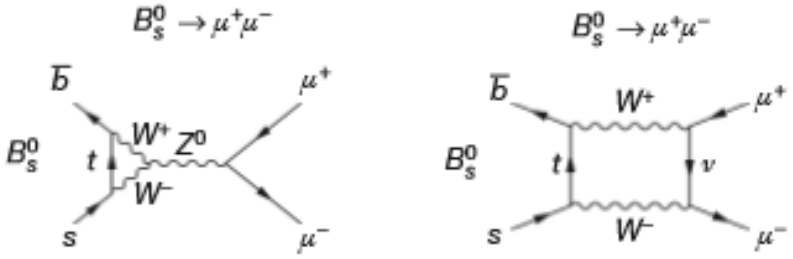

Figure 1.7: Feynman diagrams of two FCNC processes: as every FCNC process observed so far, they are loop suppressed (image from the CMS and the LHCb collaborations, 2015).

neutrino oscillations implied that neutrinos must be massive particles. In principle, the SM could be extended to include also the right-handed neutrino ν_R, which would show no electroweak interaction (it would be a sterile particle). Hence, to give mass to the neutrino in the same way as the other particles we could write a Yukawa term for the lagrangian

$$\mathcal{L}_{Yukawa} = f_\nu \overline{L}\tilde{\Phi}\nu_R + h.c. \tag{1.4}$$

In Formula 1.4 $L = (\nu_i \; e_i)$ is the lepton doublet with the i-th flavor, $\tilde{\Phi} = (\Phi^0 \; -\Phi^-)$ is linked to the Higgs doublet, while f_ν is the coupling constant. When the Higgs field obtains its vacuum expectation value v, the mass term for the neutrino becomes $-f_\nu v/\sqrt{2}$. However, to account for the mass constraints given by experimental and cosmological observations ($m_\nu < 1$ eV), f_ν should be smaller than 10^{-11}, which looks quite unnatural.
An alternative mechanism is also possible if neutrinos are Majorana particles: in this case, a certain number of sterile neutrinos N can be introduced and the Yukawa term becomes

$$\mathcal{L}_{Yukawa} = f_\nu \overline{L}\tilde{\Phi}N_R + B\overline{N}^c_R N_R + h.c. \tag{1.5}$$

After the spontaneous symmetry breaking, the Lagrangian becomes

$$\mathcal{L}_{Yukawa} = f_\nu \frac{v}{\sqrt{2}}\overline{\nu}_L N_R + B\overline{N}^c_R N_R + h.c. \tag{1.6}$$

In this case, the mass eigenstate for the lightest neutrino is $\propto v^2 f_\nu^2/B$. For a certain range of values for f_ν, the sterile neutrino can be a candidate for Dark Matter.

- The strong CP problem: while weak interactions violate P and C symmetries, strong interactions are parity and charge conserving. Nevertheless, when the whole lagrangian is written, it can be noticed that

the fourth term does violate CP:

$$\mathcal{L}_{QCD} = -\frac{1}{4}G_{\mu\nu a}G_a^{\mu\nu} + \sum_{flavors} i\bar{q}\gamma^\mu D_\mu q - \bar{q}mq + \frac{\alpha_s\theta}{8\pi}G_{\mu\nu a}G_a^{\mu\nu} + h.c. \tag{1.7}$$

(here α_s is the coupling of the strong interaction, and G is the field strength). To conserve CP, θ should be set equal to zero (the current upper bound is $|\theta| < 10^{-10}$). This raises the question, known as "the strong CP problem": why is θ so small?

1.2 Candidates for Dark Matter

To solve the issues in the Standard Model described in the previous Section, several particles have been proposed. Some of the theorized solutions for Particle Physics issues are also suitable candidates for the Dark Matter; in this Section the most promising alternatives are described. For the sake of completeness, the possibility that Dark Matter is constituted by MACHOs (massive astrophysical compact halo objects) is also included, but it must be kept in mind that this solution would not fix any problem in the SM.

There are features that are common to every candidate for DM; indeed, to be a valid solution for the DM puzzle, a particle must have some basic characteristics:

1) it must not interact electromagnetically or strongly with SM particles;

2) it must be stable, or have a decay time τ greater than the life of the Universe;

3) it must be collisionless enough to account for its abundance in the Universe;

4) it must be cold or warm. To understand if a particle is to be considered *cold*, *warm* or *hot*, it must be considered that, right after the Big Bang, all particles were coupled. A particle decouples when its interaction rate Γ becomes comparable to the Hubble rate H. If at this moment (also called *freeze-out*) the mass of the particle m_{DM} is much smaller than the temperature T of the Universe, the particle is relativistic and is said to be a *hot relic*; if, on the contrary, $m_{DM} \gg T$, the particle is non-relativistic and is said to be a *cold relic*; *warm relics* constitute the intermediate case in which the particle is becoming non-relativistic at the time of freeze-out. Hot Dark Matter would lead to the damping of the density fluctuations that led to formation of structures smaller than clusters. Within this scenario galaxies could form

only after fragmentation of clusters, but this would not be consistent with the observation of small structures at high redshifts, therefore the hypothesis of a hot Dark Matter has to be ruled out.

In principle, there is no reason to postulate weak or very weak interactions of DM with SM particles; nevertheless, the solutions proposed below assume DM particles to have interactions other than the sole gravitational one.

1.2.1 WIMPs

WIMPs are particles with an expected mass at the weak scale (tens of GeV-TeV); they are one of the most studied candidates for Dark Matter, their appeal residing in the fact that there exists a mechanism which produces them with the right amount in the primordial universe, and in the fact that a particle with a mass at the weak scale could satisfy the astrophysical/cosmological need of DM and solve the hierarchy problem at the same time.
To understand how WIMPs could be produced with the right amount, one must consider what happens to WIMPs in the primordial universe:

- when the universe is hot enough, there is chemical equilibrium, hence the more DM particles are created by SM particles interactions, the more DM particles annihilate into SM particles; in this situation, the Boltzmann equation reads

$$\frac{dn}{dt} + 3Hn = (n_{eq} - n) < \sigma v >= 0 \tag{1.8}$$

  where the left-hand side accounts for the changes of the DM number density in a comoving volume, and the right-hand side terms are, respectively, the annihilation and production rate of DM particles, which sum up to zero in equilibrium.

- when the temperature of the universe drops below the WIMP mass (supposing it is the heaviest particle under consideration), DM production from SM particles is not possible anymore, while DM particles keep annihilating; the number density of WIMPs is then Boltzmann-suppressed by the factor $e^{-m_{DM}/kT}$.

- DM number density keeps dropping until the freeze out moment, that is, the decrease of WIMPs annihilation rate below the expansion rate H of the universe: $n < \sigma v >= H$. By taking $H^2 \sim T^4/m_P^2$, we get for the number density of DM particles at the freeze out moment:

$$n_{f.o.} \sim \frac{T_{f.o.}^2}{m_P < \sigma v >} \tag{1.9}$$

If we now consider the density parameter, by inverting the expression

$$\Omega_m = \frac{m_{DM} n_{DM,0}}{\rho_C} \sim \frac{m_{DM} n_{DM,f.o.} T_0^3}{\rho_C T_{f.o.}^3} \sim \frac{m_{DM}}{\rho_C T_{f.o.} m_P < \sigma v >} \sim 0.3 \tag{1.10}$$

and by taking $< \sigma v > \sim g_{weak}^4 / 16\pi^2 m_{DM}^2$, we get for the WIMP mass the value $m_{DM} \sim 100$ GeV - 1 TeV, right at the weak scale!

The astounding result of finding the correct relic abundance with a weak scale mass is known as "the WIMP miracle".
Some of the main candidates to be the WIMP particle come from the supersimmetry theories, which predict a supersimmetric partner for every SM particle, with all the same quantum numbers of the SM partner except for the spin, which would differ by 1/2. Feng (2010) lists the neutral supersymmetric particles to be:

- Spin 3/2 (fermion): gravitino
- Spin 1/2 (fermion): 4 neutralinos
- Spin 0 (scalar): 2 sneutrinos

However, he points out that sneutrinos have too large cross sections to be a DM candidate, while the gravitino cannot be considered a WIMP (see Subsection 1.2.2); instead, the lightest neutralino is a good candidate to be the WIMP particle.

1.2.2 SuperWIMPs

SuperWIMPs are particles which differ from WIMPs both for the kind of interactions (which are supposed to be much weaker than WIMP's) and the production mechanism. In fact, SuperWIMPs would be generated by the decay of an unstable WIMP particle (see Figure 1.8; this would remove the constrain on the WIMP candidate to be a neutral particle (hence it could be also, for example, a charged slepton).
The main candidates for superWIMPs are the gravitino (the superpartner of gravitons) and the axino (the superpartner of axions, see Subsection 1.2.5).

1.2.3 Sterile Neutrinos

The sterile neutrino, hypothesized to solve the neutrino mass problem (Section 1.1.2), could solve at the same time the DM problem, if its mass is in a certain range below the Grand Unification Scale; unfortunately, this scale is currently far beyond experimental reach. Another possibility is to consider the electroweak scale, obtaining a sterile neutrino of mass $m \quad \mathcal{O}\,10$

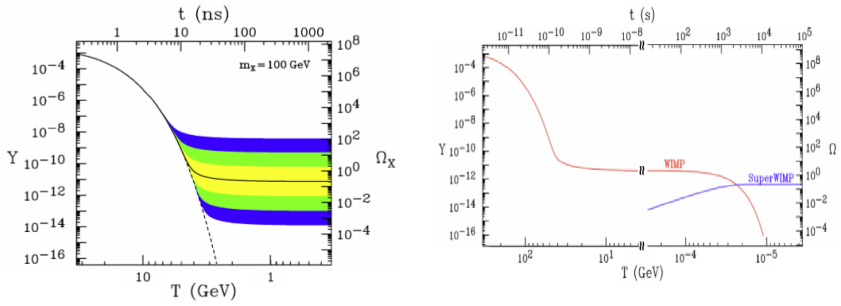

Figure 1.8: On the left, WIMP freeze out scenario for different values of $< \sigma v >$; on the right, superWIMP scenario: the left part of the graph is the same as the WIMP scenario, but at later cosmic times WIMP particles decay into superWIMPs (Feng, 2010).

keV, which could even explain Dark Matter, neutrino oscillations and baryon asymmetry at once (Bertone, 2010).This kind of sterile neutrino would be a warm dark matter candidate, whose production may be explained by different mechanisms: for example, oscillations or decay of heavy particles (Feng, 2010). Astrophysical observations and considerations constrain the possible mass and mixing angle of this sterile neutrino to be a viable candidate for Dark Matter, as shown in Figure 1.9.

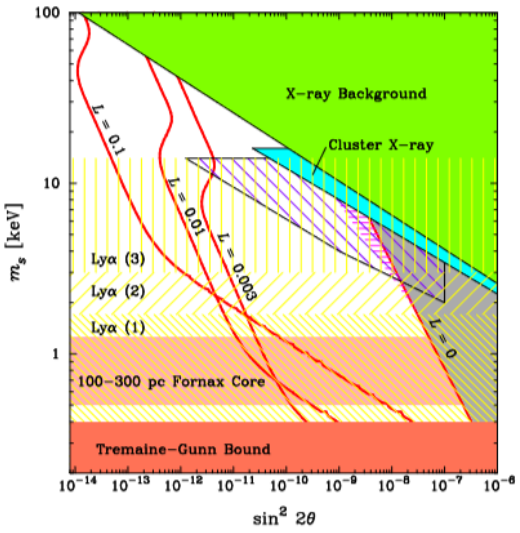

Figure 1.9: Phase space for the sterile neutrino of mass m $\mathcal{O}$10 keV; the constraints are given by astrophysical observations (Abazajian & Koushiappas, 2006).

Over the years, neutrino experiments have reported some anomalies, which could be hints for one or more sterile neutrinos, that would add to the three known electron, muon and tau neutrino flavors. The anomalies that were

found are the following:

- **Gallium anomaly**: two experiments probing solar neutrinos, GALLEX and SAGE, when tested with radioactive sources recorded a short-baseline deficit of ν_e (Figure 1.10, left).

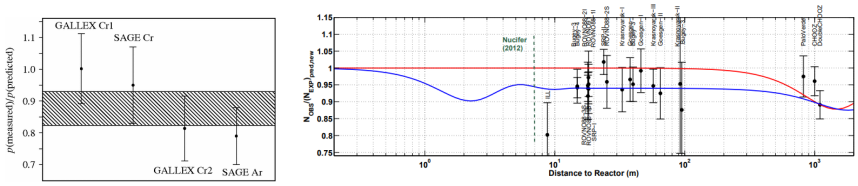

Figure 1.10: Left: plot relative to the Gallium anomaly, showing the ratio between observed and expected events for the two experiments GALLEX and SAGE, and different radioactive sources (Abdurashitov et al., 2006). Right: plot relative to the reactor anomaly, showing the ratio between experimentally observed and expected events as a function of the distance from the reactor; the number of expected events is taken assuming no oscillation; the red line is relative to a model with three mass states, while the blue line represents a model with an extra state (Abazajian et al., 2012).

- **Reactor anomaly**: it is a deficit of electron antineutrinos in the energy range 1 - 10 MeV; although the anomaly could be due, perhaps partly, to the fuel composition varying with time, another promising explanation is the existence of a sterile neutrino (Figure 1.10, right).

- **Accelerator anomalies**: two different anomalies were discovered by two different experiments; LSND (Liquid Scintillator Neutrino Detector) was an accelerator experiment operating with a baseline $L \sim 30$ m and a beam of muon antineutrinos, which observed an excess of $\bar{\nu}_e$ with respect to the predictions (Figure 1.11, top). MiniBooNE, on the other hand, while studying LSND anomaly with different baseline and beam energy, found out another anomaly, the *Low Energy Excess*: it is an excess of $\bar{\nu}_e$s at lower energies than LSND's excess when dealing with antineutrinos; since MiniBooNE operated also with neutrinos, it observed a similar excess of ν_e (Figure 1.11, bottom).

Albeit these anomalies would be explained by a sterile neutrino of mass $m^2 \quad \mathcal{O}\,1\ \mathrm{eV}^2$, pointing to a sterile neutrino of different nature than the ones aforementioned, there are some works, such as Bringmann et al. (2014) and Tang (2016), which try to identify Dark Matter, or at least a part of it, with a possible sterile neutrino linked to one of these anomalies.

1.2.4 Hidden Dark Matter

Hidden Dark Matter is based on the hypothesis that the DM particles have no gauge interactions with SM particles, hence they could interact with

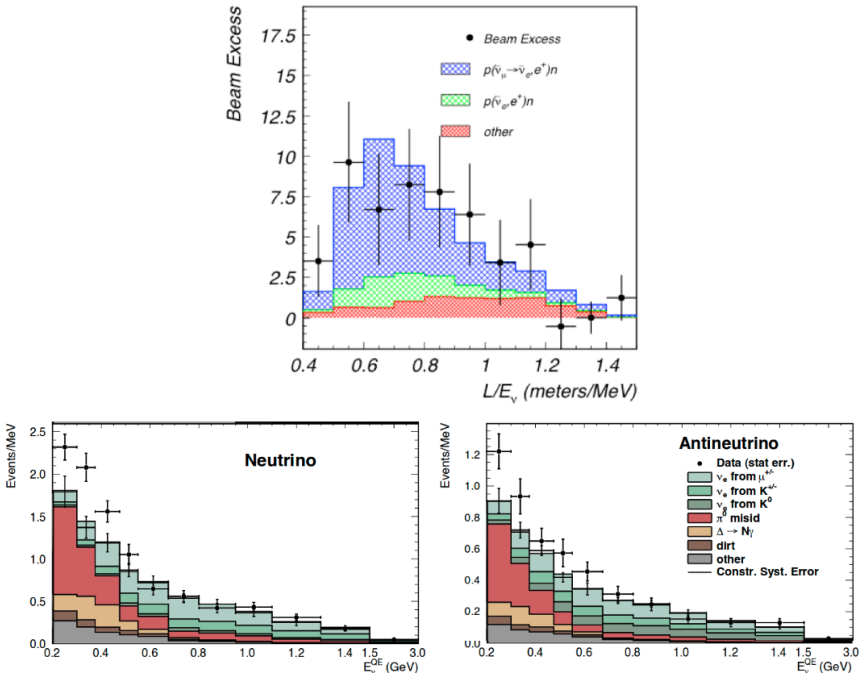

Figure 1.11: Top: electron antineutrino excess observed by LSND Collaboration (2001). Bottom: electron neutrino (left) and antineutrino (right) excess observed by MiniBooNE (2013).

them only through gravitational and, potentially, Yukawa interactions. The correct relic density of this kind of particle would be obtained through a "WIMPless miracle"; in fact, by remembering that $\Omega_m \propto \frac{1}{<\sigma v>} \sim \frac{16\pi^2 m_{DM}^2}{g^4}$, in principle any combination of the DM mass and the coupling constant g which yields the right value for Ω_m would work.

1.2.5 Axions and ALPs

Axions are particles that were theorized by Peccei and Quinn to solve the strong CP problem (Peccei & Quinn, 1977). They pointed out that the θ term appearing in Equation 1.7 could be seen as related to a field, instead of a static term, with a new global $U(1)$ symmetry (called *PQ symmetry*). Through a spontaneous symmetry breaking, the field assumes the minimum vacuum energy value and a Goldstone boson, the axion, acquires mass. It turns out that the value $\theta = 0$ also corresponds to the minimum for the QCD vacuum energy, hence whatever the initial value of θ is, it will go to zero after some time (Weinberg, 1978; Wilczek, 1978). By writing θ as the ratio between the field a and a mass scale f_a (the *axion decay constant*), one can write the Lagrangian relative to axions that substitutes the term with θ in Equation 1.7:

$$\mathcal{L}_{axions} = \frac{\alpha_s}{8\pi} G_{\mu\nu a} \tilde{G}_a^{\mu\nu} \frac{a}{f_a} + \frac{1}{2}(\partial_\mu a)(\partial^\mu a) \tag{1.11}$$

where it is clear that this kind of particle would show interactions also with gluons; moreover, it is theorized that at loop level axions would show interactions also with photons through a term

$$\mathcal{L} = -g_\gamma \frac{\alpha_{e.m.} a}{\pi f_a} \vec{E} \cdot \vec{B} \tag{1.12}$$

and with fermions through a term (see Asztalos et al., 2006)

$$\mathcal{L} = i g_f \frac{m_f}{f_a} a \bar{f} \gamma_5 f \tag{1.13}$$

where g_γ and g_f are model-dependent parameters.
Depending on whether inflation or PQ symmetry breaking happened first, two scenarios are possible: if the symmetry breaking happened before inflation, the latter would have stretched a small region of space, providing a uniform value for a in our observable universe; if, on the other hand, inflation happened first, a could assume different values from one point to another, generating topological defects such as strings or walls (Figure 1.12). Defining an *initial misalignment angle* α, for which the initial value of a is $a_i = f_a \alpha$, it can be shown that the density parameter for axions would depend on α for the former case (Bertone, 2010):

$$\Omega_a \sim 0.15 \left(\frac{f_a}{10^{12} GeV} \right)^{7/6} \left(\frac{0.7}{h} \right)^2 \alpha^2 \tag{1.14}$$

while for the latter case it would simply be:

$$\Omega_a \sim 0.7\left(\frac{f_a}{10^{12}GeV}\right)^{7/6}\left(\frac{0.7}{h}\right)^2 \tag{1.15}$$

As aforementioned, when the axion acquires mass, θ will eventually oscillate around zero; the oscillations have frequency given by the mass of the axion, and they will damp as the universe expands. Nevertheless, until the Compton wavelength of the axion is larger than the Hubble scale, the axion field remains constant (Wantz & Shellard, 2010); only when $m_a \sim 3H(t)$ there is the onset of damped oscillations; this implies that high mass axions, which would oscillate very fast, would enter the horizon when the universe is radiation dominated, and evolve as $1/R^4$, becoming rapidly negligible in the cosmic scenario: only low mass axions, which are unrelativistic, could enter the horizon during the matter dominated era, evolving as $1/R^3$ and being able to contribute significantly to the DM amount. Thus, low-mass axions would be a form of cold dark matter, produced by a non-thermal mechanism. For the sake of completeness, it is necessary to mention that axion mass is also assumed to be evolving with time, as the temperature of the universe changes.

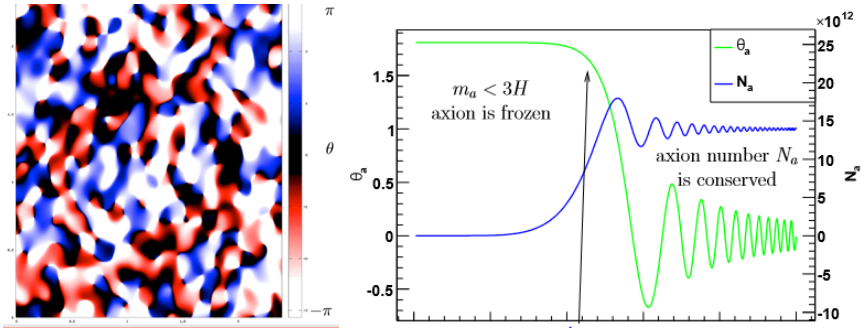

Figure 1.12: Left: section of space for a scenario in which inflation happened before PC symmetry breaking. Different colors correspond to different values of a; points in which a assumes different values at the same time correspond to strings in a 3D space, lines with different values of a are walls in the 3D space. From a slide of J. Redondo at ICTP Summer School on Particle Physics (2017). Right: in green, evolution of axion field oscillations; when $m_a < 3H(t)$ there is no oscillation, while when $m_a \sim 3H(t)$ damped oscillations start. In blue, the correspondent axion comoving number density is shown, assuming both $H(t)$ and m_a evolving slowly (Wantz & Shellard, 2010).

Axions can be generalized to *axion-like particles* (ALPs), which are generated with similar mechanisms as axions, but not by the PC symmetry breaking, and are not related to the strong CP problem (Irastorza & Redondo, 2018). Whatever the nature of axions or axion-like particles is, astrophysical probes supply constrains for their masses as shown in Figure 1.13: axions, for example, would affect stellar evolution, modifying the duration of the different

stages of stars' life (Turner, 1990); moreover, other hints to exclude some mass ranges are given by the SN 1987a neutrino burst duration, by the solar neutrino flux and by the sound-speed profile of the Sun (Raffelt, 2008). Similar considerations can also be made for ALPs in general. Experiments looking for axions and ALPs provided other constraints for the mass of these particles.

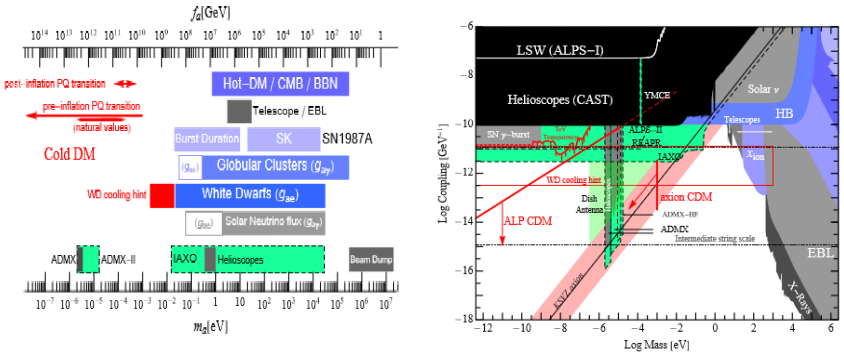

Figure 1.13: On the left, parameter space (f_a and mass) for the axions; on the right, parameter space for ALPs: grey, blue and dark green areas indicate the exclusion regions due respectively to astronomical observations, astrophysical/cosmological arguments, and experiments. Both plots are from Essig et al. (2013).

1.2.6 MACHOs

Another possibility that involves the presence of unseen matter, yet this time composed of SM particles, is that DM is simply made of black holes and other dark, compact objects, the so-called MACHOs (Massive Astrophysical Compact Halo Objects); these objects could be, for example, white dwarfs, black holes, neutron stars or brown dwarfs. However, a DM composed exclusively of this kind of objects would contradict the Big Bang Nucleosynthesis predictions (Parker, 1989). IN 2015, LIGO collaboration observed the merging of two massive black holes with masses of ~ 30 $M_\odot$ (LIGO Scientific Collaboration & Virgo Collaboration, 2016); further observations discovered other massive BH mergers, such as GW170104 (LIGO Scientific Collaboration & Virgo Collaboration, 2017). Thanks to these discoveries, the hypothesis that DM could be made of primordial black holes (PBH) regained popularity (Bellomo et al., 2018): for example, Bird et al. (2016) suggested that the first mergers observed by LIGO, GW150914, could be two primordial black holes. PBH are black holes that formed during the early phases of the Universe, possibly even before the Big Bang Nucleosynthesis (Parker, 1989); this could avoid the constraints given by its predictions.
One way to probe the hypothesis of MACHOs/PBHs is to exploit the phenomenon of microlensing: a MACHO that crossed the line of sight between an observer and a background star would produce a characteristic change in

the luminosity curve of the star. The luminosity curve would present two unique features:

1) the change in luminosity would be the same for every wavelength that is observed, since the lensing is an achromatic effect;

2) the luminosity curve would be perfectly symmetric with respect to the maximum (see Figure 1.14, left).

Several collaborations (e.g. MACHO, EROS, OGLE) have looked for the microlensing effect in the Milky Way halo, detecting a number of events that led to rule out the hypothesis of MACHOs constituting the 100% of mass in the MW halo at 95% confidence level (Alcock et al., 2000): hence, although some fraction of Dark Matter could be made of collapsed objects, a large part should exist also in other forms. In Figure 1.14, on the right, the most likely values for the fraction of MW halo constituted by MACHOs, and for the MACHOs mass, is reported.

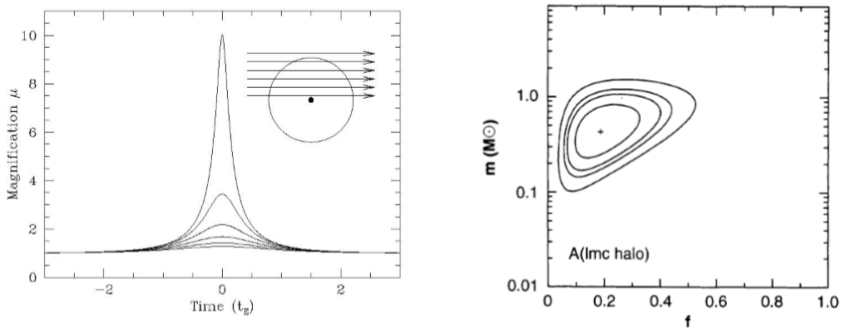

Figure 1.14: On the left, the typical light curve in the case of a microlensing event (Wambsganss, 2006); on the right, contours enclosing the 68%, 90%, 95% and 99% probability of having a certain fraction of MACHOS of a certain solar mass (Alcock, 2000).

This analysis, anyway, holds only for objects smaller than 30 $M_\odot$ (Alcock et al., 2001); if we consider primordial black holes, other constraints can completely exclude masses below $\sim 10^{-15}\ M_\odot$ and above $\sim 10^2\ M_\odot$ (see Figure 1.15, and Green, 2014), some of them being the (non-)observation of Hawking radiation produced by evaporated low-mass PBH, of perturbations in the CMB, or of femtolensing of Gamma-Ray Bursts. So far, there exist some possibilities for DM to be entirely constituted of MACHOs of Moon-like masses.

1.3 Experimental search for Dark Matter

Having assumed an extra interaction apart from gravity in Section 1.2 between DM and SM particles, there exist three different Feynman diagrams

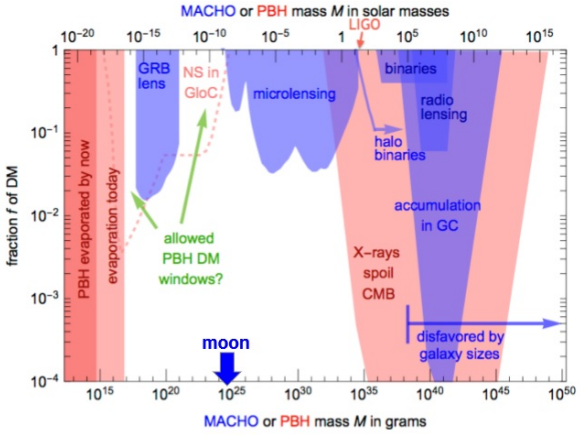

Figure 1.15: Range of masses and fraction of DM allowed for primordial black holes (Cirelli, from darkuniverse.uni-hd.de/pub/Main/WinterSchool12Slides/CirelliDM_1.pdf).

that could be written for a tree-level interaction between two DM and two SM particles; they are reported in Figure 1.16.

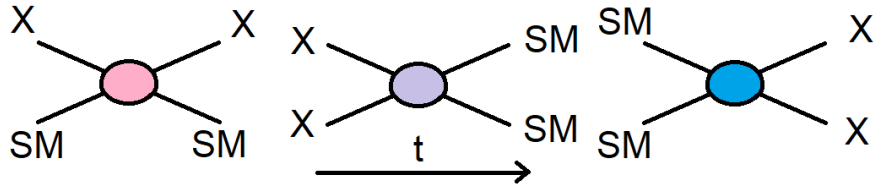

Figure 1.16: On the left, Feynman diagram of a collision between a DM and a SM particle, the process observed in direct detection. In the middle, annihilation of two DM particles into two SM particles, the process searched for in indirect detection. On the right, creation of two DM particles after a collision between two SM particles, the event that is sought in colliders.

The existence of three different Feynman diagrams open the possibility to search for DM with three different approaches, which offer complementary ways to probe DM particles: direct detection, indirect detection, and search at colliders, which are describer more in details in the following paragraphs.

1.3.1 Direct detection

Direct detection experiments attempt to detect DM particles recoiling against atomic nuclei as the Earth moves along its orbit. In fact, it is estimated that the local density of DM is $\rho_{DM} = 0.3 \pm 0.1$ GeV/cm^3 (Bovy & Tremaine, 2012), hence the detectors should receive a "Dark Matter wind" that modulates its velocity with respect to the Earth during the year (having its maximum in June).

Despite the large expected flux of DM particles (10^{11} (GeV/m$_{DM}$) m^{-2}s^{-1}), the event rate is very low ($\sim$ 0.01 event kg^{-1} day^{-1}), as well as the transferred energy: if we define in the center-of-mass frame q as the momentum that is gained by the nucleus, θ as the scattering angle, μ as the reduced mass, and v as the velocity of the DM particle, then the maximum recoil energy is

$$E_{R,max} = \frac{2v^2\mu^2}{M_{nucleus}} = \frac{q^2_{max}}{2M_{nucleus}} \tag{1.16}$$

where $q^2 = 2\mu^2 v^2(1 - \cos\theta)$ and $\theta = \pi$. Putting into the formula typical values for $v \sim 200$ km s^{-1} and a mass for the DM particle $m_{DM} \sim 100$ GeV, one obtains a recoil energy of the order of 10s of KeV.
Because of the small fluxes and recoil energies involved, it is necessary to have a very low background, in particular the shielding from cosmic rays is fundamental: this is the reason why direct detection experiments are located underground. The concept of the experiments is to detect the events generated by Dark Matter recoils against target nuclei by measuring one or two of these effects: heat, photons or ionization electrons. The technology and material that is used as a target varies a lot among the experiments: for example, a dual phase TPC with Xenon is used for the LUX and the XENON1T experiments, Sodium iodide crystals are exploited for DAMA/NaI and DAMA/LIBRA experiments, germanium and silicon bolometers are employed for the CDMS experiment (Undagoitia & Rauch, 2017). Different technologies allow to extract different information from the signal (Figure 1.17). In Figure 1.18 the schematic view of two direct detection experiments (XENON1T and DAMA) are reported as an example.

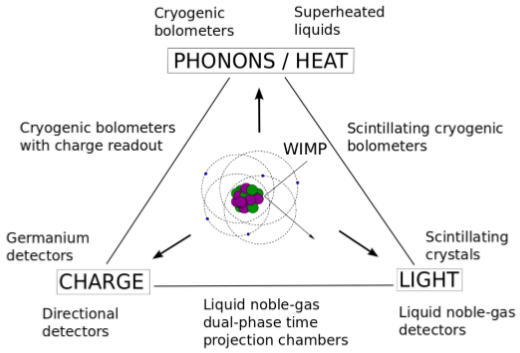

Figure 1.17: Scheme of the different information that can be obtained by using different technologies for direct detection experiments (Undagoitia & Rauch, 2017).

Direct detection experiments have been used so far to set upper limits to the cross section of DM particles against nucleons (Figure 1.19); there have

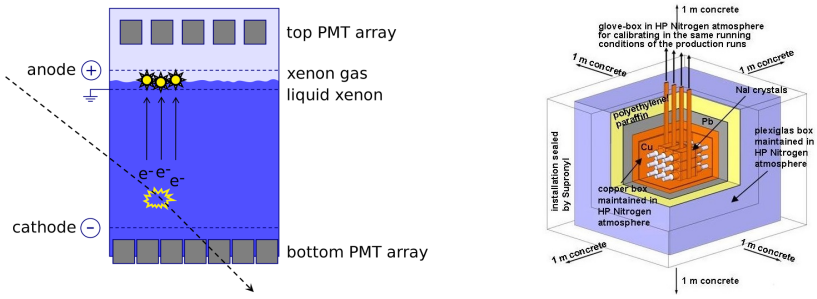

Figure 1.18: Schematic view of XENON1T (on the left) and DAMA (on the right) experiments. For the Xenon1T experiment, liquid and gaseous xenon are used in a dual-phase time projection chamber (TPC); when a DM particle interacts with nuclei of liquid xenon, a flash of light and a delayed charge signal are produced. The two signals are detected by photomultipliers put at the bottom and at the top of the TPC; for the charged signal, there exists an electric field which attracts electrons towards the liquid/gas part (image by the XENON collaboration/Rafael Lang, http://www.xenon1t.org/). The DAMA/NaI experiment, on the other hand, exploits nine radiopure NaI scintillators, doped with Thallium, to detect the signals; light guides take the scintillation light to photomultipliers. The apparatus is shielded from external sources of noise through several layers of different materials (such as copper, lead, polyethylene, paraffin). For more details see Bernabei et al. (2003). Image from http://people.roma2.infn.it/dama/web/ind_nai.html.

also been some claims for a possible discovery from the DAMA collaboration: during Phase 1's years of observations, they observed a modulation with a period of (0.998 ± 0.002) yr, and a maximum at (144 ± 7) days (Bernabei et al., 2013). Phase 2's analysis confirmed the presence of the signal (Figure 1.20, left), without finding any systematic or side reaction which could explain the modulation in another way (Bernabei et al., 2018). Nevertheless, no other experiments have confirmed the signal (Messina, 2017). For example, Xenon100 compared collected data with the expected signal if DAMA/LIBRA modulation was due to DM (Figure 1.20, right), but the analysis led to exclude the hypothesis at $4.8\,\sigma$ (XENON collaboration, 2015). A possible explanation, if we were to exclude a spurious signal, could be a spin-dependent coupling between DM and protons, which would favor couplings to Sodium iodide over Xenon or Germanium (Gelmini, 2015).

Experiments such as MiniBooNE, which are in principle designed to probe neutrino oscillations, are also used to search for DM scattering against nuclei or electrons; in the case of MiniBooNE, however, DM is produced through the interactions of an accelerator's proton beam (MiniBooNE-DM Collaboration, 2018).

1.3.2 Indirect detection

Indirect detection search for the products of decay or annihilation of Dark Matter particles. The consequence of these processes range from effects on

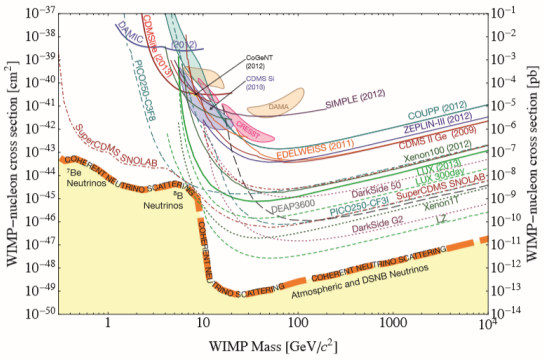

Figure 1.19: Limits on the cross section of DM particles against nucleons set by several direct detection experiments, as a function of the WIMP mass. Solid lines are used for performed experiments, dashed lines are expectations for the upcoming experiments at the time the plot was made; the orange line shows the limit under which neutrino background would dominate (Cooley, 2014).

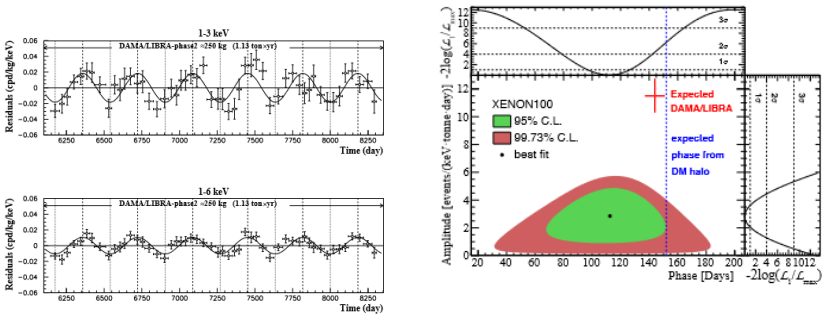

Figure 1.20: On the left, modulation detected by the DAMA/LIBRA experiment during Phase 2, as a function of time, in two different energy intervals (Bernabei et al., 2018). On the right, analysis by XENON collaboration which excluded DAMA/LIBRA modulation at 4.8 σ: in green and red are reported 95% and 99.73% contours for XENON100 best fit of data, while the red cross indicates the expected signal assuming the DAMA/LIBRA modulation as a signal due to DM (XENON collaboration, 2015).

astrophysical or cosmological phenomena (e.g. they could affect the temperature of stars and planets, the Big Bang Nucleosynthesis, the CMB), to the production of an excess of charged cosmic rays (protons, antiprotons, electrons, positrons...) and of neutral particles (neutrinos and gamma rays); while charged particle are easily deviated along their path from the production point to the detector, making it difficult to identify the original source, neutrinos keep the whole directional information. Some of the (either ongoing or concluded) most relevant experiments for indirect detection are: the Fermi Large Area Telescope (LAT), part of the Fermi gamma-ray space telescope, antimatter satellites such as Pamela and AMS-02, ground based cherenkov telescopes such as Magic, Hess and Veritas, and neutrino telescopes such as IceCube.

Several claims about the possible detection of a DM annihilation signal has been made throughout the years: for example (see Gelmini, 2015) the satellite Integral and some balloon experiments have detected an emission line at a photonic energy of 511 keV, which seemed to be spherically symmetric, but it was then found to be produced by a population of binary stars; another line was detected by Fermi LAT at 130 GeV, and an excess of positrons in the positron fraction $N(e^+)/(N(e^+)+N(e^-))$ was reported by Pamela, Fermi LAT and AMS-02 (Figure 1.21); these claims could by explained by the presence of annihilating dark matter, but also by artifacts (for the former case) or by the presence of astrophysical sources (for the latter case).

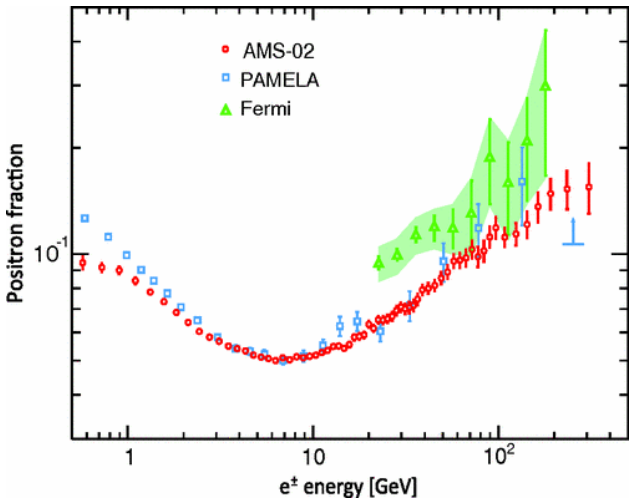

Figure 1.21: Measurements of the fraction of positrons over the sum of positrons and electrons $N(e^+)/(N(e^+)+N(e^-))$, from the experiments Fermi LAT, AMS-02 and Pamela (Aguilar et al., 2013).

1.3.3 Search at colliders

Researches at colliders have the peculiarity to be the only ones in which Dark Matter particles can be produced, and under controlled conditions. Several experiments of this kind have been conducted in the past, at LEP and at Tevatron, but the most recent is performed at Large Hadron Collider (LHC) at CERN. LHC is the largest particle collider in the world, being a 27-km-long circular ring, which currently makes proton collide with an energy in the center of mass frame of 13 TeV. A scheme of LHC is reported in Figure 1.22: protons are produced by separating hydrogen nuclei and their electrons through an electric field; the protons obtained this way are accelerated firstly in a linear accelerator and then in a series of circular accelerators of increasing sizes.

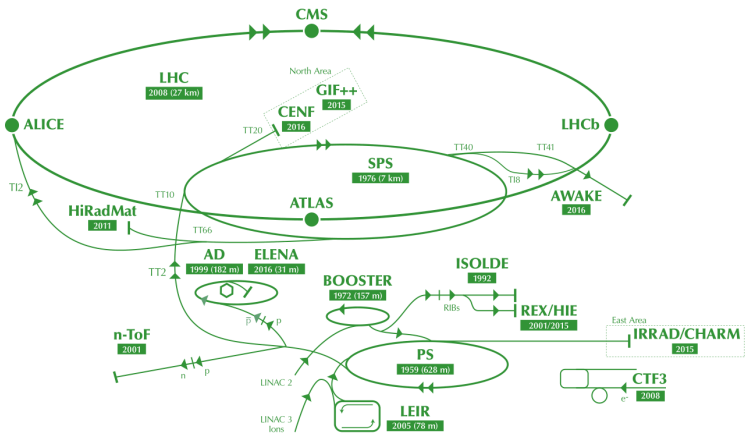

Figure 1.22: Scheme of LHC and the proton accelerator system (image from CERN).

There are four main experiments at LHC: ATLAS, CMS, LHCb and ALICE; ATLAS and CMS are multi-purpose experiments which, among several researches of physics beyond the Standard Model, are also looking for Dark Matter particles. The principle that is exploited to detect Dark Matter is the conservation of momentum in the plane perpendicular to the direction of the colliding protons (the *transverse momentum* p_T): indeed DM particles interact too weakly to produce a detectable signal; nevertheless, if a DM particle is produced, the transverse momentum of the detected signal will not sum to zero, as it should (Buchmueller et al., 2017). A scheme of this situation is reported in Figure 1.23.
The most promising channels to detect DM particles are the following:

- Monojets → events characterized by the production, together with the DM particle(s) (that is, large missing transverse momentum), of a quark or a gluon, which give rise to a hadronic jet (Figure 1.24, right).

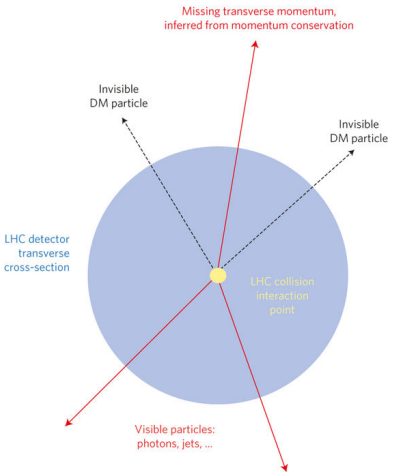

Figure 1.23: Scheme of a situation in which DM particles are produced, and their presence can be inferred thanks to the presence of unbalanced transverse momentum (Buchmueller et al, 2017).

Also two jets are allowed, as long as their transverse momentum is high; the main background sources in this case are the production of a Z boson which then decays into two neutrinos, and the production of a W boson which then decays into a neutrino and a misidentified charged lepton.

- Mono-V $\rightarrow$ events characterized by the production, together with the DM particle(s) (that is, large missing transverse momentum), of a Z or W vector boson which are recognized by detecting, respectively, two charged leptons or one charged lepton.

- Monophoton $\rightarrow$ events characterized by the production together with the DM particle(s) (that is, large missing transverse momentum), of a gamma photon γ (Figure 1.24, left). The main backgrounds in this case are the production of a Z boson, which then decays into two neutrinos, together with the photon, and several processes in which a hadronic jet or an electron mimic the photon.

- Mono-b$\rightarrow$ events characterized by the production together with the DM particle(s) (that is, large missing transverse momentum), of a heavy quark (beauty or top). This process is treated more extensively in Section 2.3.

As far as it concerns the theoretical model assumed to research for DM at colliders, different approaches are possible: one of them could be to assume a specific theoretical framework, e.g. Supersymmetry, to have a full predictive power; Buchmueller et al. (2017) point out that assuming a specific theoretical model helps to optimize the experimental searches, and makes it

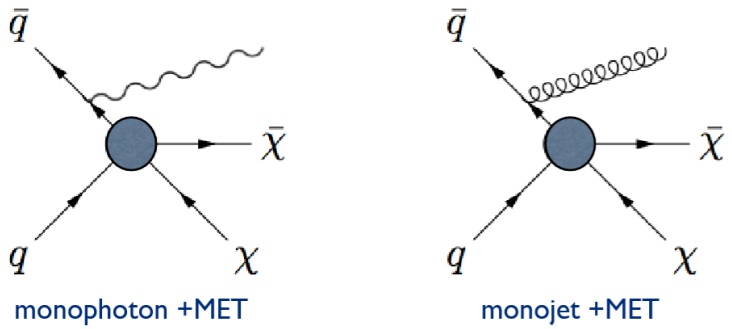

Figure 1.24: On the left, process in which DM and a monophoton is produced; on the right, process in which DM and a monojet is produced (From a talk of Sarah Alam Malik at Rencontres de Moriond, 2012).

possible to connect collider and non-collider searches. Nevertheless, model-agnostic approaches are also adopted, in the form of effective field theories and simplified models.

Effective field theories (EFTs) have their rationale on the idea that, to probe a phenomenon at a certain energy scale, one could consider only the most relevant processes, and ignore those which are characterized by an energy scale that is too high or too low with respect to that phenomenon. With this approach the interaction between SM and the DM particles is considered a four-point contact interaction (Buchmueller et al., 2017). Nevertheless, it is important to remind that effective field theories can be used only until the mass of the mediator is very heavy (Abercrombie et al., 2015).

Simplified models, differently from EFTs, introduce into the description also a mediator, which could be for example a boson from the SM, or with the same couplings as SM particles (see Buchmueller et al., 2017, and Albert et al., 2017). Albert et al. 2017 enumerate the four parameters that are required for basic simplified models to research for DM-SM interaction mediated by a boson:

- In the case of vector or axial-vector mediators, the four parameters are the mass of the DM particle, m_{DM}, the mass of the mediator, M_{med}, the coupling at the mediator-DM-DM vertex, g_{DM}, and the coupling at the mediator-SM-SM vertex, where g_q is the same for all the quarks.
- In the case of scalar or pseudo-scalar mediators, the four parameters are the same, but Yukawa couplings change the value of g_q for the different quarks.

Chapter 2

Search for Dark Matter at CMS

In this Chapter, the main focus will be the research for Dark Matter at the CMS experiment, conducted at the Large Hadron Collider (LHC). In particular, in 2.1 the CMS detector will be described; in Sections 2.2 and 2.3 the latest studies from the CMS collaboration will be presented, respectively for monojet and mono-V final states, and for events with b-jets and missing transverse energy.

2.1 The CMS detector

CMS (Compact Muon Solenoid) is a multi-purpose detector that operates at CERN and is located 100 m underground along the ring of LHC. In Figure 2.1 a scheme of CMS is reported. In order to understand how the detector operates, it is important to define a pseudorapidity η and the coordinate system used by CMS, which assigns the z coordinate to the direction of the beam propagation, and the x and y coordinates to the perpendicular plane; the x axis points towards the center of the LHC ring, while the y axis points vertically upward. Considering this coordinate system, and defining θ as the polar angle with respect to z, the *pseudorapidity* is then $\eta = -\ln\tan(\theta/2)$; this quantity is the parameter which is used to describe the acceptance of the several parts of CMS. The angle in the perpendicular plane with respect to the proton beam is marked as Φ. Here follows a description of the main components of the detector, written with the help of the CERN website *cms.web.cern.ch/news/detector-overview* and its subsections, starting from the innermost layer and going towards the outer layer:

1) Inner tracking system $\rightarrow$ the main purpose of this layer is to measure accurately the position of the particles multiple times, in order to reconstruct their trajectories, curved by the magnetic field; this allows

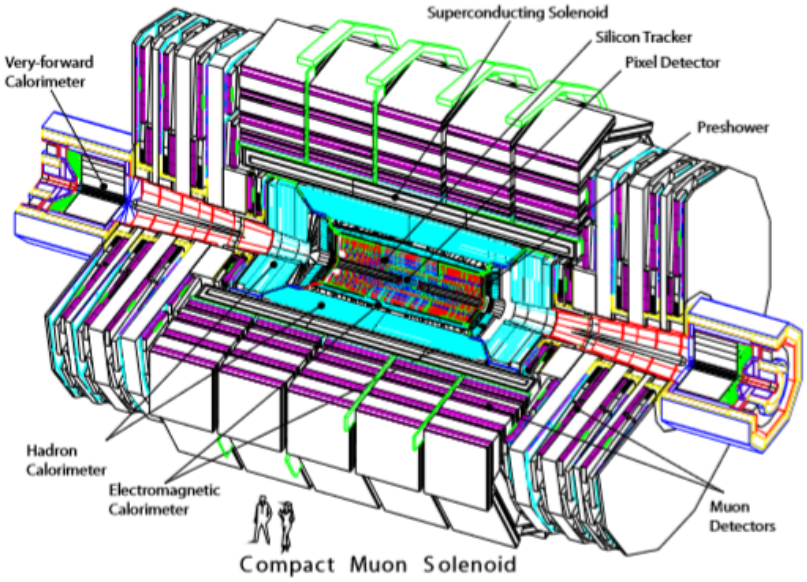

Figure 2.1: Scheme of the CMS detector (image from CMS collaboration, 2008).

to compute their momenta. A great challenge was posed by the need to perturb the particle as little as possible, which led to a lightweight tracker able to measure the position of the particle so accurately that only few measurements are required. The tracking system is made of two different components, both made of silicon: the part composed of pixels and the part composed of strips.

The first one has 3 different pixel layers, each one few centimeters far from the beam pipe; at such close distance this part must withstand an enormous amount of particles coming from the collisions. The 65 million pixels are of dimension 100 μm by 150 μm, and being mounted on three different layers they allow to perform a 3-D reconstruction of the particle's trajectory; to prevent overheating, cooling tubes are also present.

The strip part is, in turn, divided into an inner barrel (TIB) and an outer barrel (TOB); the inner barrel contains four strip layers, while the outer barrel consists of six strip layers, reaching a 130 cm distance from the beam. This part is kept at a temperature of $\sim$ 250 K to avoid serious damages, and exploits tens of thousands of optical fibers to transmit the signal, in order to analyze it.

2) Electromagnetic calorimeter (ECAL) → for the purposes of LHC, it is very important to measure the energies of the particles produced in the collisions; this is the reason why CMS is provided with an electromagnetic calorimeter, and a hadronic calorimeter. The former is used to study electrons and photons. ECAL is made of ~ 80000 lead tungstate crystals; this material is transparent and dense at the same time, and the presence of oxygen makes it scintillate when a photon or an electron crosses a crystal; due to the characteristics of lead tungstate, the result are electromagnetic showers which maintain a high velocity, are small and can be detected with high precision, yet without needing a bulky calorimeter. The scintillation light is collected by photodetectors, and then amplified and digitized.
While the majority of crystals are used for the barrel part, ECAL is also provided with two endcaps; moreover, two preshower detectors have been mounted in front of the endcaps, in order to distinguish between high-energy and low-energy photons. To complete the structure of this part, a cooling system was constructed, to keep the crystals at a temperature no higher than ~ 273.3 K, which guarantees the desired characteristics of the scintillation light mentioned above.

3) Hadron calorimeter (HCAL) → this layer is used to detect hadrons, in particular CMS calorimeter allows to measure not only the energy of the particles, but also their position and their time of arrival, thanks to a succession of absorbing layers and scintillating layers; the hadron produces secondary particles when it passes through an absorbing layers, and these secondary particles then produce scintillation light in the scintillating layers (which is collected by optical fibers) and other particles in the next absorbing layers, creating a cascade. The scintillating layers are divided into smaller pieces (tiles), each of it connected to an optical fiber; together, the signals collected from the different tiles give a hint of the hadron's path, energy, and/or type. The HCAL barrel is partly contained inside the superconducting solenoid, while another part surrounds it; an endcap and a forward component complete the calorimeter.

4) Superconducting solenoid → the huge magnetic field of CMS (4 Tesla) is obtained by 7 meter diameter long coils crossed by electricity, which are kept at a temperature of 4.65 K to be superconductive; the magnetic field bends the path of the particle, the curvature depending on the particle's momentum.

5) Muon trackers → since the muons can penetrate matter very effectively before interacting, this layer is the most external one; it is composed of four layers (called "stations") alternated with iron layers that act as return yoke for the magnetic flux, and exploits different techniques to

detect muons: drift tubes and resistive plate chambers for the barrel region, while for the endcap region, together with the resistive plate chambers, cathode strip chambers are used.

In addition to these components, there are also two forward detectors:

1) CASTOR → it is both an hadronic and electromagnetic calorimeter, which probes the very forward region of the detector ($-6.6 < \eta < -5.2$) collecting the Cherenkov light produced by particles (Gunnellini, 2013).

2) Zero degree calorimeter (ZDC) → it is made of two parts, an electromagnetic and a hadronic calorimeter, whose purpose is to study heavy ion collisions, detecting and measuring the energy of forward neutrons and photons (Grachov et al., 2006).

2.1.1 Events management, reconstruction and simulation

Since during the running periods LHC produces a huge number of events inside the detector (about 10^9 events per second, CMS Collaboration, 2017), a selection is required. For this purpose, there is a *trigger system* which reduces the number of events to be stored to about 400 events per second. The trigger system operates in two steps:

1) Level-1 (L1) trigger → it is a trigger system implemented in the hardware described above; its purpose is to operate a first selection of events which could be of physical interest. To do that, it analyzes the data coming from the ECAL, the HCAL, and the muon chambers, without considering data from the tracker, trying to reject events which look physically uninteresting. With this amount of information the L1 is capable of roughly distinguishing signatures of photons, leptons and jets, together with global quantities such as missing transverse energy. The processed information from the calorimeters and the muon chambers is then put together in the *global trigger*, where it is studied through different L1 algorithms.

2) High Level trigger (HLT) → the data that passed the L1 triggers are sent to the HLT, a software based trigger system which further discards some data: the incoming rate is $\sim$ 100 kHz, while the outgoing rate is the aforementioned $\sim$ 400 Hz. It uses algorithms for particle reconstruction similar to the offline analysis, but with looser requirements, in order to keep the selection process fast enough; moreover, while the offline reconstruction looks at the event globally, putting together the information from all the parts of the detector, the HLT studies the event near the regions where the L1 trigger found some interesting signatures. At this level all the information is available, data from the inner tracker included. The HLT firstly confirms, or disproves,

the L1 analysis, discarding a large fraction of candidate events. The remaining events are then filtered through two further passages: the reconstruction of leptons and that of the full track.

A nice insight about triggers is Bocci's lecture at Summer Student Lecture Programme Course (2016), from which most of the above information is taken.

Event reconstruction

The raw data that are selected by the HTL undergo a process of reconstruction, that is, extrapolating the nature of detected particles and their physical characteristics from the detectors output (e.g. voltages). To do this, Particle Flow algorithms are used (see for example Beaudette, 2014); they exploit the fact that different particles leave different energy with peculiar paths in specific parts of the CMS detector (Figure 2.2). The algorithms collect the information from the different parts of the detector to understand what kind of particle could leave that kind of signal: for example, a photon (neutron) would not leave a signal in the tracker, and deposit energy in the ECAL (HCAL), while an electron (charged hadron) would be detected both in the tracker and in the ECAL (HCAL).
All the gathered information is used to reconstruct the particle's trajectories and vertices, and finally compute its characteristics, such as transverse momentum, origin point, direction (η, Φ). Other characteristics that are computed are: quality tags (soft, or loose, Id, medium Id, tight Id), which is useful to distinguish leptons produced by the weak decays of Z and W bosons from leptons coming from other sources, e. g. the decay of a heavy flavor hadron, or of a pion/kaon (CMS Collaboration, 2017); isolation, that is aimed to distinguish objects in jets from those without significant amount of other energetic tracks within a narrow cone.
Other than single particles, other objects and quantities can be reconstructed: jets and missing transverse energy.

- jets $\rightarrow$ they are formed by the processes through which a gluon or quark produced in the collision undergoes, since due to confinement they cannot be isolated: instead, they will give rise to a hadronic shower,boosted in the direction of the original quark, until final states are produced. In a jet, on average, the 65% of energy is carried by charged hadrons, 10% by neutral hadrons, while the remaining energy is given by photon: when the muons, the electrons and isolated photons are identified, it is possible to look for the jets' charged and neutral hadrons and photons (CMS Collaboration, 2017). Once the jets are reconstructed, a further step is looking for heavy flavor quarks (charm and beauty) inside the jets. For this purpose there are specific algorithms, such as CSVv2, and also a flourishing research in the deep

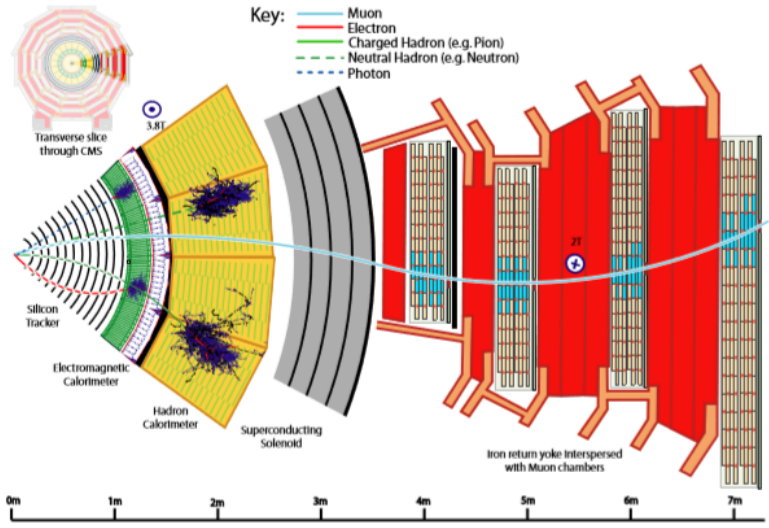

Figure 2.2: Tracks left from the different particles in the CMS detector (CMS Collaboration, 2017).

learning field. The main idea for heavy flavor tagging algorithm is that hadrons with b quarks or c quarks produced in the collision decay very rapidly: hadrons with b quarks have a lifetime of ~ 1.5 ps, hadrons with c quarks of $\lesssim 1$ ps (CMS Collaboration, 2018). For this reason a secondary vertex (SV) is produced at a typical distance from the primary vertex, and can be exploited for the flavor tagging (Figure 2.3).

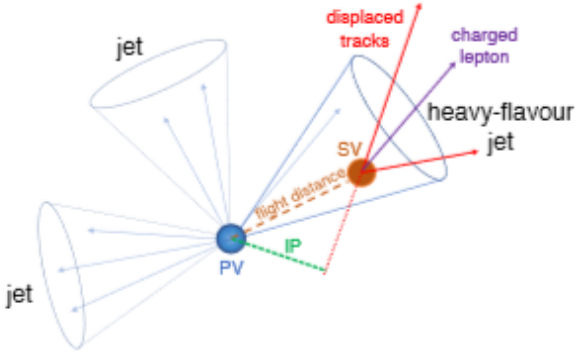

Figure 2.3: (Cartoon of a heavy flavor jet: the secondary vertex produced by the decay of the b or c quark is displayed (CMS Collaboration, 2018).

- Missing transverse energy → as mentioned in Section 1.3.3, the total

momentum perpendicular to the beam direction should sum to zero; however, some undetected particles (such as neutrinos, and maybe new physics particles) may carry away some momentum from the detector: the resulting unbalance for the momentum is the missing transverse energy E_T^{miss} (or MET), also called missing tranverse momentum. This quantity is defined as the vector sum of all the particles' transverse momenta with opposite sign:

$$\vec{E}_T^{miss} = - \sum_{i}^{nparticles} \vec{p}_{T,i} \tag{2.1}$$

If the contribution from reconstructed charged leptons (and photons) is removed, the *hadronic recoil* HR is obtained:

$$HR = -\vec{E}_T^{miss} - - \sum_{i}^{n_{e,\mu\,\tau,\gamma}} \vec{p}_{T,i} \tag{2.2}$$

The so-reconstructed quantities about the identified particles, missing energy and jets, together with information from the HLT triggers are stored into .root files containing several events, in the form of trees whose branches are the different measured quantities; the data format that is currently used at CERN is the NANOAOD format.

Simulations

A common way to look for new physics from the LHC data is to compare events, selected according to criteria chosen specifically for the analysis that is wanted to be performed, with Montecarlo simulations of the possible backgrounds. The simulations are produced with different softwares, which perform different tasks, due to the complexity of the events that have to be reproduced. The description of the simulation process that follows is written mainly with the information from Marshall (2014) and Webber (2017).
The first necessary phase is to generate the event, that is, the proton-proton collision and the following processes of hadronic shower. For this purpose, there are softwares, such as MADGRAPH, GRACE, ALPGEN, which are able to compute the final states of partons given their distribution; the information has to be integrated with the help of hadron level event generator, like PYTHIA, HERWIG++ and Sherpa, which are specialized in reproducing high energy collisions, hard processes, parton showers (Figure 2.4, left); to improve the functionality of these event generators, methods such as POWHEG or MC@NLO can be implemented to compute next to leading order (NLO) corrections (see Sjöstrand et al., 2014, and Frixione et al., 2007).
Once the event is generated, the interaction with the different parts of the detector has to be simulated: for this step the software "Geant4" is used (see

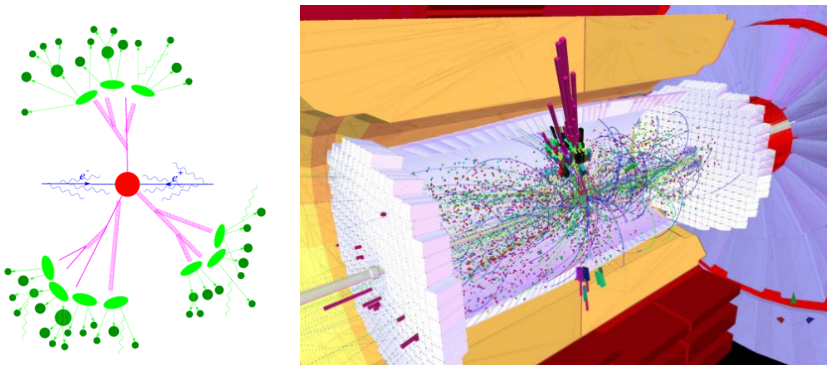

Figure 2.4: Left: simplified picture of an event generated with Sherpa (image taken from Marshall, 2014). Right: simulation of an event at CMS with Geant4 (from Fermilab website, https://web.fnal.gov/organization/SCS/SitePages/Home.aspx).

geant4.web.cern.ch/). Inside the Geant4 framework the detector's parts have to be built, balancing the need of a faithful reproduction and of an acceptable computation time. In this reproduced detector the generated particle interact with the different materials, producing a situation such as that in Figure 2.4 (right), and yielding a list of data regarding the position of the particles in the detector, energy deposits, times of flight...
Finally, the produced information has to be put in the same form of actual LHC data: this process is called *digitization*. In this phase, effects of pileup and noise are added; after that, physical quantities are translated into detectors output. At this point simulated data can be treated as actually detected data, reconstructing the events and storing the related variables into Root trees.

2.2 Search for Dark Matter in monojets

Data collected during 2016, with an energy of the center of mass $\sqrt{s} = 13$ TeV and an integrated luminosity of 12.9 fb^{-1}, were analyzed considering monojet final states and mono-V final states (CMS collaboration, 2016). The mediator could be either a scalar, pseudoscalar, vector or axial vector boson.
To be considered, an event had to possess a missing transverse momentum $p_T^{miss} > 200$ GeV, and at least one jet with transverse momentum $p_T > 100$ GeV. The main sources of background are the processes $Z(\nu\nu)$+jets and $W(l\nu)$+jets, which constitute the 90% of background; the first contribution was estimated by considering that the branching fraction of $Z \to \nu\nu$ is 3 times larger than that of $Z \to e^+e^-$ and $Z \to \mu^+\mu^-$, hence the events with a dilepton were counted; to eliminate the second contribution, events with at least one energetic charged lepton were excluded ($p_T > 10$ GeV for electrons and muons, $p_T > 18$ GeV for taus).

The number of events with missing transverse energy were then compared to the estimated number of background events (Figure 2.5), and the result shows no deviation from the SM predictions.

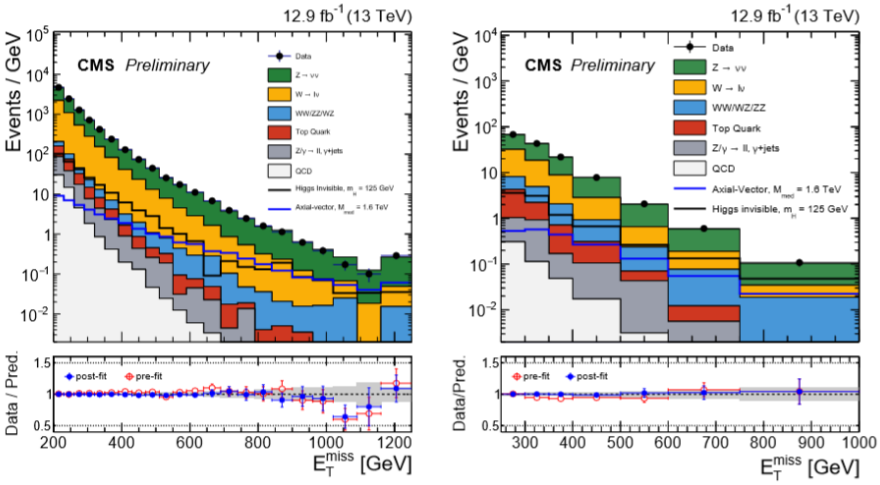

Figure 2.5: Comparison between estimated background signals and observed signals in the case of monojet signals (left) and mono-V signals (right), as a function of missing transverse energy; the two quantities are in agreement (CMS collaboration, 2016).

The study allowed to set lower limits to the masses of mediators both with spin 1 (masses lower than 1.95 TeV are excluded at 95% CL) and with spin 0 (masses lower than 100 GeV for scalar bosons and 430 GeV for pseudo-scalar bosons are excluded at 95% CL); moreover, the upper limit for the branching ratio of the Higgs boson decaying into invisible particles was found to be 0.44 at 95% CL. For more details, the reader can refer to the paper of the CMS collaboration (2016).

2.3 Search for Dark Matter associated with $b\bar{b}$ jets in 2015 data

The CMS collaboration analyzed the data collected during proton-proton collisions at the energy of the center of mass $\sqrt{s} = 13$ TeV in 2015, using the dataset of integrated luminosity of 2.17 fb^{-1} (CMS collaboration, 2016). What was looked for was the production of $\Phi b\bar{b}$, where Φ is a scalar or pseudoscalar boson which after the production decays into DM particles $\Phi \to \chi\chi$; the search was also sensitive to $\Phi t\bar{t}$ production (Figure 2.6).
The motivations for this kind of analysis reside on the fact that scalar or pseudo-scalar mediators have Yukawa-style couplings to the SM particles, which are larger for heavy quarks.

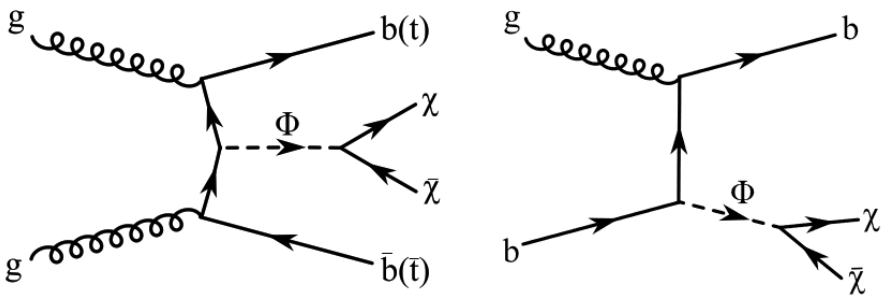

Figure 2.6: Feynman diagrams of two possible mechanisms for DM production from the decay of a scalar or pseudoscalar boson, associated with b jets (image from CMS collaboration, 2016).

The study required to recognize the presence of missing energy E_T^{miss} and to reconstruct the jets produced by beauty (or top) quarks; however, it must be pointed out that one of the two produced quarks usually has a transverse momentum much smaller than the other quark's, or an angle which is too large for the detector acceptance: hence, the signature of a b quark together with a large missing E_T was seeked. The analysis of the events proceeded in three steps:

1) Event reconstruction: the particle-flow algorithm was used to identify all the particles that were produced during the event. Several criteria are used to distinguish one particle from another, such as in which part of the detector the energy of the particle was released.

2) Event selection and categorization: a veto is applied to reject events which satisfy specific conditions, in order to reduce the number of background events. Some examples of vetoed events are: events with missing $E_T^{miss} \leq 200$ GeV, or events with an isolated electron or muon with transverse momentum $p_T > 10$ GeV.

3) Signal extraction: signal is extracted through a fit of the data, considering together contributions from beauty and top quarks, and assuming a coupling $g_{DM} = 1$ between the Φ boson and the DM particles (Figure 2.7).

The study of 2015 data associated with the production of beauty quarks lead to set an upper limit to the cross section of $26 \cdot \sigma/\sigma(g_\chi, g_q = 1)$ in the case of a pseudoscalar mediator, and of $5 \cdot \sigma/\sigma(g_\chi, g_q = 1)$ in the case of a scalar mediator; the results are shown in Figure 2.8.

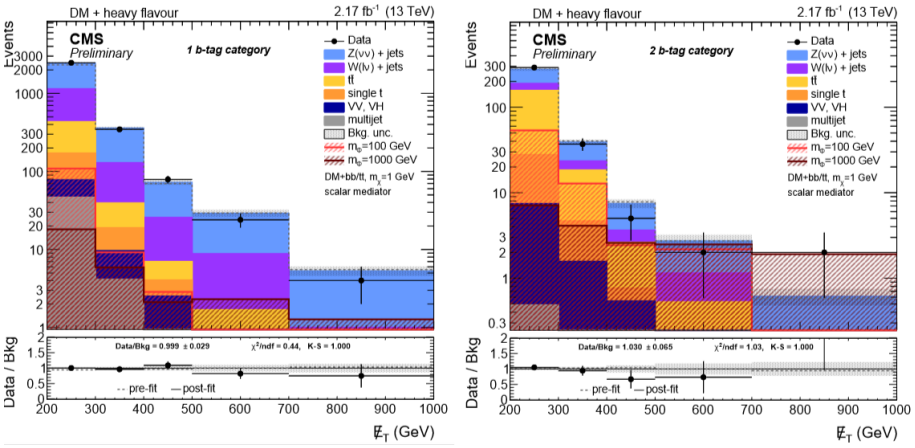

Figure 2.7: Observed and expected events in the case of single b tagged (left) and double b tagged (right) after the fit was performed (CMS collaboration, 2016).

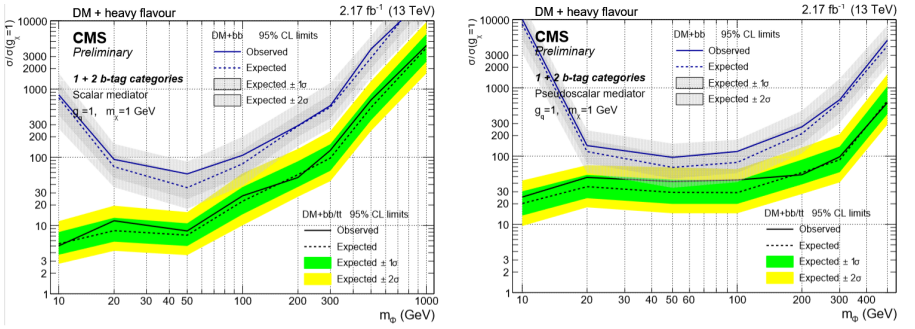

Figure 2.8: Exclusion limits for the cross section in the case of a scalar mediator (left) and a pseudoscalar mediator (right) varying the mass of Φ (CMS collaboration, 2016).

Chapter 3

Search for DM associated with b quarks in 2016 data

In this Chapter the methods and the results of the analysis of the 2016 data will be provided; firstly, the datasets that were used will be listed; then, the analysis on the control region and on the control region will be described; finally, the results are reported.
The data used for the analysis are from the 2016 run, and saved in the NANOAOD data format.

3.1 Datasets and simulations

The data that were analyzed in this work were collected during the 2016 B-H runs of LHC, with an energy of the center of mass $E_{CM} = 13$ TeV and an integrated luminosity of $L = 35.9\ fb^{-1}$. The datasets that were considered are those which contain events with a missing transverse energy trigger (the MET dataset); the complete list can be found in Table 3.1.

Dataset
METRun2016B-03Feb2017_ver2-v2
METRun2016C-03Feb2017-v1
METRun2016D-03Feb2017-v1
METRun2016E-03Feb2017-v1
METRun2016F-03Feb2017-v1
METRun2016G-03Feb2017-v1
METRun2016H-03Feb2017_ver2-v1
METRun2016H-03Feb2017_ver3-v1

Table 3.1: Datasets collected during 2016 run that were used for the analysis.

Every event that mimic the presence of large missing transverse momentum, together with the production of one or two b-quarks, is a source of background; in order to estimate the diverse sources of background, Monte Carlo simulations were used. The samples that were analyzed simulated the following processes:

- $Z \to \nu\nu+$ jets: it represents the major source of background, since if the Z boson decays into two neutrinos, it produces two particles that cannot be detected. The MC simulations were produced with MADGRAPH, generating different samples according to the sum of the hadronic transverse energy (HT).

- $Z \to e\bar{e}/\mu\bar{\mu}+$ jets: the Drell-Yan process can be a background if the two leptons are missed by the detector; moreover, it is a useful sample to normalize the $Z \to \nu\nu+$ jets background. The sample is a inclusive simulation, in which events were generated with MADGRAPH and Pythia8.

- $W \to \nu\, lep+$ jets: this kind of event, in the cases the charged lepton passes undetected, are the second source of background. The MC simulations were run in different intervals of HT, generating events with MADGRAPH and Pythia8.

- top-quark pair: since when the top decays, it produces b quarks and W bosons, it can contribute to the background for this analysis The simulations were produced with POWHEG and Pythia8.

- single top production: it can produce background events for the same reason as top-quark pairs; the simulations were produced with POWHEG and Pythia8, with the exception of the top decaying via the s-channel, generated with AMC@NLO and Pythia8.

- QCD: although QCD events have a huge cross sections, their contribution is very low if events with large E_T^{miss} are considered; nevertheless, for completeness also these samples were included in the analysis. QCD simulations were produced with MADGRAPH and Pythia8, in exclusive regions divided by HT.

The list of MC samples is reported in Table 3.2; all the listed samples were produced in specific campaign at CERN and are at disposal for the several analysis that are carried out.
For each sample, three parameters are specified: the number of contained events N_{ev}, the cross section σ and the k-factor correction[1]. These parameters are necessary in order to normalize the simulations to the data, since

[1] The k-factor is a correction needed when exclusive MC samples, divided by HT, are generated, computing also the NLO: in fact, the p_t of W and Z bosons is not perfectly reproduced, hence a correction is needed to take into account this flaw.

Dataset	N_{ev}	σ	k-factor
$Z \to \nu\nu +$ jets:			
ZJetsToNuNu_HT-100To200_13TeV-madgraph-v1	1839772	280.5	1.23
ZJetsToNuNu_HT-200To400_13TeV-madgraph-v1	1880005	77.7	1.23
ZJetsToNuNu_HT-400To600_13TeV-madgraph-v1	1020309	10.71	1.23
ZJetsToNuNu_HT-600To800_13TeV-madgraph-v1	1455893	2.562	1.23
ZJetsToNuNu_HT-800To1200_13TeV-madgraph-v1	2170137	1.183	1.23
ZJetsToNuNu_HT-1200To2500_13TeV-madgraph-v1	369514	0.286	1.23
ZJetsToNuNu_HT-2500ToInf_13TeV-madgraph-v1	405030	0.0006976	1.23
$W \to \nu lep +$ jets:			
WJetsToLNu_HT-70To100_TuneCUETP8M1_13TeV-madgraphMLM-pythia8-v1	10094300	1353	1
WJetsToLNu_HT-100To200_TuneCUETP8M1_13TeV-madgraphMLM-pythia8_ext2-v1	39617787	1343	1.395
WJetsToLNu_HT-200To400_TuneCUETP8M1_13TeV-madgraphMLM-pythia8_ext2-v1	19914590	359.6	1.526
WJetsToLNu_HT-400To600_TuneCUETP8M1_13TeV-madgraphMLM-pythia8_ext1-v1	5796237	48.85	1.679
WJetsToLNu_HT-600To800_TuneCUETP8M1_13TeV-madgraphMLM-pythia8_ext1-v1	14908339	12.05	1.442
WJetsToLNu_HT-800To1200_TuneCUETP8M1_13TeV-madgraphMLM-pythia8_ext1-v1	6069652	5.501	1.442
$Z \to e\bar{e}/\mu\bar{\mu} +$ jets:			
DYJetsToLL_M-50_TuneCUETP8M1_13TeV-madgraphMLM-pythia8_ext1-v2	49144274	5765.4	1
top-quark pair production:			
TT_TuneCUETP8M2T4_13TeV-powheg-pythia8-v1_1	8404893	831.76	1
TT_TuneCUETP8M2T4_13TeV-powheg-pythia8-v1	68676263	831.76	1
single top production:			
ST_s-channel_4f_leptonDecays_13TeV-amcatnlo-pythia8_TuneCUETP8M1-v1	1000000	3.34368	1
ST_t-channel_antitop_4f_inclusiveDecays_13TeV-powhegV2-madspin-pythia8_TuneCUETP8M1-v1	5922361	80.95	1
ST_t-channel_top_4f_inclusiveDecays_13TeV-powhegV2-madspin-pythia8_TuneCUETP8M1-v1	11108068	136.02	1
ST_tW_antitop_5f_inclusiveDecays_13TeV-powheg-pythia8_TuneCUETP8M2T4-v1	998276	35.85	1
ST_tW_top_5f_inclusiveDecays_13TeV-powheg-pythia8_TuneCUETP8M2T4-v1	992024	35.85	1
QCD:			
QCD_HT1000to1500_TuneCUETP8M1_13TeV-madgraphMLM-pythia8-v1	4767100	1207	1
QCD_HT100to200_TuneCUETP8M1_13TeV-madgraphMLM-pythia8-v1	6652304	27990000	1
QCD_HT1500to2000_TuneCUETP8M1_13TeV-madgraphMLM-pythia8-v1	3970819	119.9	1
QCD_HT2000toInf_TuneCUETP8M1_13TeV-madgraphMLM-pythia8-v1	323338	25.24	1
QCD_HT200to300_TuneCUETP8M1_13TeV-madgraphMLM-pythia8-v1	3053785	1712000	1
QCD_HT300to500_TuneCUETP8M1_13TeV-madgraphMLM-pythia8-v1	5062461	347700	1
QCD_HT500to700_TuneCUETP8M1_13TeV-madgraphMLM-pythia8-v1	6702397	32100	1
QCD_HT700to1000_TuneCUETP8M1_13TeV-madgraphMLM-pythia8-v1	2985805	6831	1

Table 3.2: Simulated samples used to estimate the number of background events; the name of the simulated sample, the number of simulated events N_{ev}, the cross section σ and the k-factor correction are reported.

the MC samples are not necessarily produced at the same luminosity: the normalization factor N_f to reweight the samples is computed as

$$N_f = \frac{L(pb^{-1}) \cdot \sigma \cdot k}{N_{ev}} \tag{3.1}$$

3.2 Preliminary operations

A lot of the events in the simulated and real datasets do not have characteristics which are interesting for the present study, and only slow down the analysis process; moreover, not all the branches contain interesting variables to look for dark matter. For this reason, the datasets were skimmed and slimmed: in order to slim the files, only the branches of the datasets' trees that were needed for the analysis were kept, that is the branches containing the variables for MET, jets, muons, electrons, taus and photons. In addition, a selection of events with missing energy triggers was operated. The triggers that were used for the analysis are reported in Table 3.3; events were kept if they had at least one of the triggers. The number of events before and after the selection can be seen in Table 3.4.

Trigger
HLT_PFMETNoMu90_PFMHTNoMu90_IDTight
HLT_PFMETNoMu110_PFMHTNoMu110_IDTight
HLT_PFMETNoMu120_PFMHTNoMu120_IDTight
HLT_PFMET110_PFMHT110_IDTight
HLT_PFMET120_PFMHT120_IDTight

Table 3.3: List of missing energy triggers used for the analysis.

Selection	W→ lep+ν + jets	Z→ $\nu\nu$ + jets	Z→ lep + jets	single t	$t\bar{t}$	QCD	Data
Without any selection	96400905	9140660	49144274	20020729	77081156	33518009	165216731
MET triggers	19170028	4140898	226761	836099	8849825	583538	71394823

Table 3.4: Number of events before and after the selection of events with at least one of the missing energy triggers of Table 3.3.

In this phase a definition of what a "*good*" object is was chosen and then applied to the different elements of an event; the conditions to request for the Id variables were found on the NANOAOD variables webpage (https://cms-nanoaod-integration.web.cern.ch/integration/master/mc80X_doc.html). Here follow the definitions:

- **MUONS**: a muon is *good* if it has a transverse momentum larger than 10 GeV, it is isolated and has at least a loose identification, that is if it satisfies the conditions of the left column of Table 3.5 with a logical "and".

Muon requirements	Electron and photon requirements
$p_t > 10$ GeV	$p_t > 15$ GeV
pfRelIso04_all < 0.25	pfRelIso03_all < 0.25
softId $= 1$	cutBased > 1

Table 3.5: Requirements for a muon (left column) and an electron/photon (right column) to be tagged as "*good*".

- **ELECTRONS**: an electron is *good* if it has a transverse momentum larger than 15 GeV, it is isolated and has at least a loose identification, that is if it satisfies the conditions of the right column of Table 3.5 with a logical "and".

- **TAUS**: a tau is *good* if it has a transverse momentum larger than 18 GeV and has at least a loose identification, that is if it satisfies the conditions of the left column of Table 3.6 with a logical "and".

Tau requirements	Jets requirements
$p_t > 18$ GeV	$p_t > 30$ GeV
idDecayMode $= 1$	jetId > 0
	$\lvert\eta\rvert < 2.5$
	$\Delta R \geq 0.4$ with respect of all good charged leptons and photons

Table 3.6: Requirements for a tau (left column) and a jet (right column) to be tagged as "*good*".

- **PHOTONS**: a photon is *good* if, like electrons, it has a transverse momentum larger than 15 GeV, it is isolated and has at least a loose identification, that is if it satisfies the conditions of the right column of Table 3.5 with a logical "and".

- **JETS**: a jet is *good* if it has a transverse momentum larger than 30 GeV, it is detected in the barrel part (pseudorapidity < 2.4) and has at least a loose Id (see right column of Table 3.6). The jets also required a cleaning operation to be kept as good: in fact, the NANOAOD format may misinterpret a signal as a hadronic jet, when it actually is leptonic; when this happens, the signal will be counted twice: once as a jet, and once as a lepton/photon. The consequence is that the jet distribution is severely shifted towards high numbers, compromising the selections, especially since further during the analysis a constraint on the number of jets will be set. In order to clean the jets, a cone of aperture ΔR between every good jet and each good lepton/photon is computed, as

$$\Delta R = \sqrt{\Delta\Phi^2 + \Delta\eta^2} \tag{3.2}$$

and jets are discarded if a lepton is inside a cone with $\Delta R < 0.4$. The operation was carried out for both MC and data samples; in Figure 3.1 the difference between the jets distribution before and after the cleaning for the data samples is shown: the events are already trigger-selected.

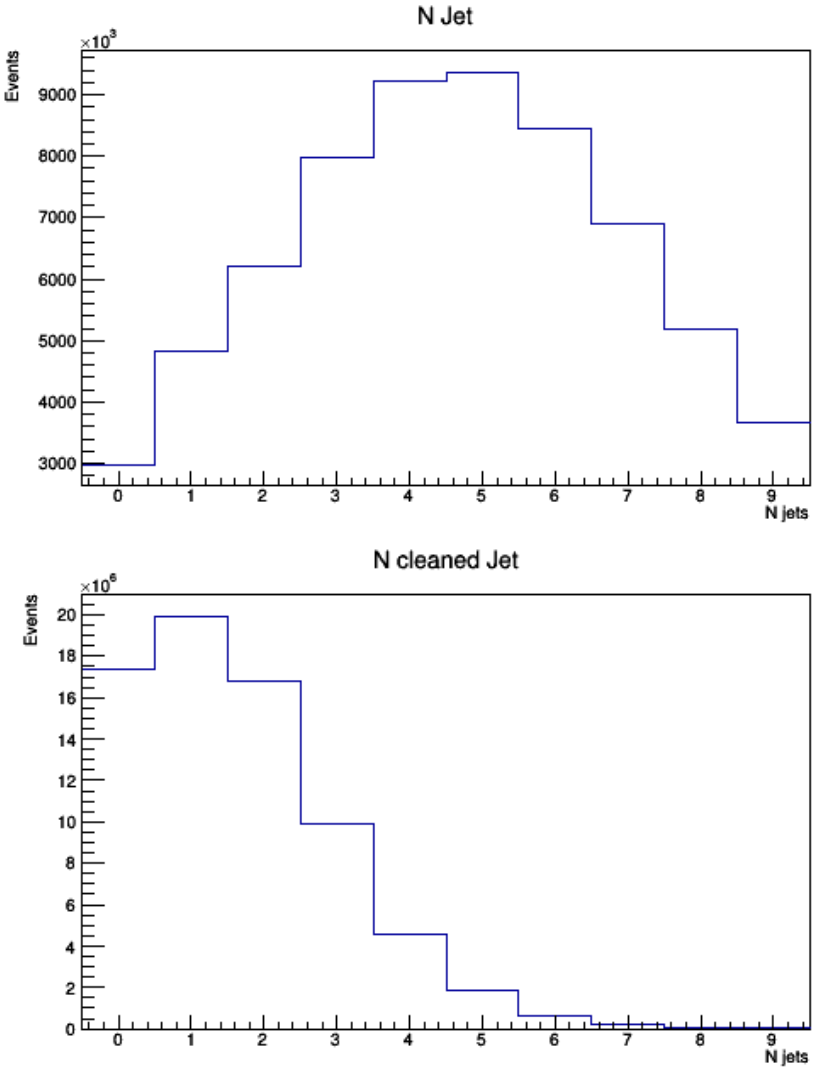

Figure 3.1: Above: distribution of jets before the cleaning; below: distribution of jets after the cleaning. The cleaning operation shifts the distribution towards low jet numbers, discarding leptonic jets. Both histograms are relative to trigger-selected events.

Finally, two regions are defined, depending on the number of jets and on the number of relative b-taggings:

- **Region 1 (R1)**: there must be one or two good jets; the leading

jet must have a transverse momentum $p_t > 50$ GeV, and the angular distance from the missing E_T must be $\Delta\Phi > 0.5$; the subleading jet, if present, has no further requirements than the ones aforementioned, apart from the angular distance from the missing E_T $\Delta\Phi > 0.5$. However, one and only one b quark must be present; the presence of a tagged b is expressed by the variable *btagCSVV2*; a medium tagging is required, that is *btagCSVV2*$>$0.8484.

- **Region 2 (R2)**: there must be two or three good jets; both the leading and the second jets must have a transverse momentum $p_t > 50$ GeV and $\Delta\Phi > 0.5$ from the missing E_T; if the third jet is present, it must also have an angular distance $\Delta\Phi > 0.5$ from the missing E_T. Overall there must be two and only two medium b-taggings.

The conditions for the two regions are summarized in Table 3.7.

	R1	R2
Leading jet	$p_t > 50$ GeV $\|\Delta\Phi(E_T^{miss}, jet)\| > 0.5$	$p_t > 50$ GeV $\|\Delta\Phi(E_T^{miss}, jet)\| > 0.5$
Subleading jet	$p_t > 30$ GeV $\|\Delta\Phi(E_T^{miss}, jet)\| > 0.5$	$p_t > 50$ GeV $\|\Delta\Phi(E_T^{miss}, jet)\| > 0.5$
Third jet	veto	$p_t > 30$ GeV $\|\Delta\Phi(E_T^{miss}, jet)\| > 0.5$
b tagging	1 CSV medium	2 CSV medium

Table 3.7: Requirements for jets in the Region 1 (R1) and Region 2 (R2).

3.3 Control regions

Despite MC are weighted in order to normalize them to the data luminosity, there may be different efficiencies for triggers, particle reconstruction or other effects that cause the MC distribution mismatch the data distribution. In order to check if the shape of the MC samples and of the data samples are the same, and to improve the comparison between them in the signal region, some known processes are studied before, looking for correction factors to apply to the simulations. For this reason, three different control regions were selected: the $Z \to \mu\mu$, the $W \to \mu\nu$, the top, and the multijet control regions. In the following Sections the characteristic and the rationale of each control region is explained.

3.3.1 $Z \to \mu\mu$ control region

It involves mainly the Drell-Yan process sample; despite in this control region the main source of background for the signal region, $Z \to \nu\bar{\nu}$ does not contribute, the two processes can be considered theoretically very similar. To correct also the $Z \to \nu\bar{\nu}$ samples, therefore, this control region is used; subtracting the two muons' contribution from the E_T^{miss}, in fact, the event becomes similar to a process where two neutrinos are produced.
An event is accepted if it satisfies the following requirements:

- There must be two good muons of opposite charge; the leading muon must have a transverse momentum $p_t > 30$ GeV, pseudorapidity $|\eta| < 2.4$ and a tight Id; the subleading muon is only required to have a pseudorapidity $|\eta| < 2.4$.
- When the two muons are identified, the hadronic recoil HR is computed subtracting their momenta from the E_T^{miss} (see Eq. 2.2), together with the Z invariant mass Z_m and its transverse momentum Z_{p_t}. These variables bring other constraints for the $Z \to \mu\mu$ control region, as it is required $70 < Z_m < 110$ GeV and $HR > 200$ GeV.
- A condition on the jets, chosen between the R1 and the R2 (Table 3.7).

The requirements for the $Z \to \mu\mu$ control region are summarized in Table 3.8.

	1 b tag	2 b tag
Leading muon	$p_t > 30$ GeV $\|\eta\| < 2.4$ tightId	$p_t > 30$ GeV $\|\eta\| < 2.4$ tightId
Subleading muon	$\|\eta\| << 2.4$ Opposite charge	$\|\eta\| << 2.4$ Opposite charge
Z_m	> 70 and < 110 GeV	> 70 and < 110 GeV
HR	$>$200 GeV	$>$200 GeV
Jets	R1	R2

Table 3.8: Requirements for the $Z \to \mu\mu$ control region.

Using the samples without the R1 or R2 filter, a first check on the shapes of MC samples and data samples was made, plotting Z_m and Z_{p_t}: the histograms can be seen in Figure 3.2. The shapes for the two sets look similar, but it is clear that a further normalization of the MC samples is needed before studying the signal region.

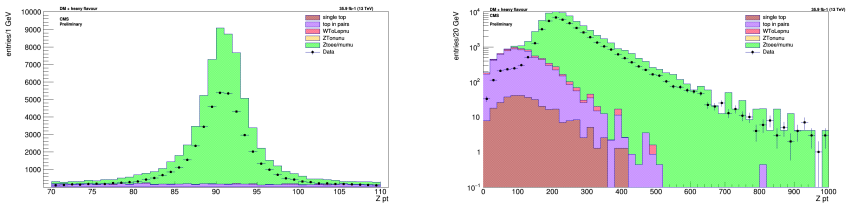

Figure 3.2: Left: comparison of the number of events as a function of Z_m for the data and MC samples; right: the comparison is made studying the distribution of Z_{p_t} . It is clear that, although the shapes are similar, a further normalization is needed.

3.3.2 $W \to \mu\nu$ control region

An event is accepted if it satisfies the following requirements:

- There must be one good muon with a transverse momentum $p_t > 30$ GeV, a tight Id and a pseudorapidity $\eta < 2.4$.

- The muon is subtracted from the E_T^{miss} to compute the hadronic recoil as in Eq. 2.2 and is used to reconstruct the W transverse mass (M_T^W), which must be greater than 50 GeV and smaller than 160 GeV, while the hadronic recoil is required to be greater than 200 GeV.

- A condition on the jets, chosen between the R1 and the R2 (Table 3.7).

The requirements for the $W \to \mu\nu$ control region are summarized in Table 3.9.

	1 b tag	2 b tag
Muon	$p_t > 30$ GeV $\|\eta\| < 2.4$ tightId	$p_t > 30$ GeV $\|\eta\| << 2.4$ tightId
M_T^W	> 50 and < 160 GeV	> 50 and < 160 GeV
HR	$>$200 GeV	$>$200 GeV
Jets	R1	R2

Table 3.9: Requirements for the $W \to \mu\nu$ control region.

Using the samples without the R1 or R2 filter, a check on the shapes of MC samples and data samples was performed also for this region, plotting M_T^W and HR: the histograms can be seen in Figure 3.3.

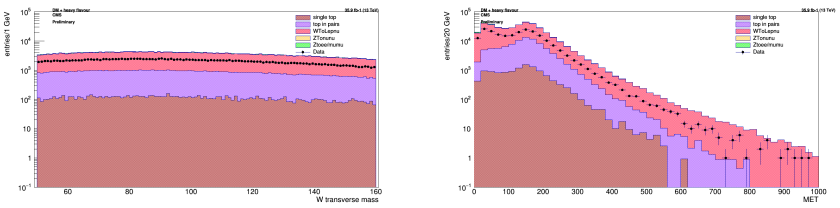

Figure 3.3: Left: comparison of the number of events as a function of Z_m for the data and MC samples; right: the comparison is made studying the distribution of Z_{p_t} . It is clear that, although the shapes are similar, a further normalization is needed.

3.3.3 Top control region

The top control region looks for tau decays $t \to \mu\nu e\nu b\bar{b}$. An event is accepted if it satisfies the following requirements:

- There must be one good muon with a transverse momentum $p_t > 30$ GeV, a tight Id and a pseudorapidity $\eta < 2.4$.
- There must be one good electron with a transverse momentum $p_t > 30$ GeV, a tight Id and a pseudorapidity $\eta < 2.5$ and opposite charge with respect to the muon.
- The muon and the electron are used to compute the hadronic recoil in an analog way as the other control regions. and which is then vetoed if ≤ 200 GeV.
- A condition on the jets, chosen between the R1 and the R2 (Table 3.7).

The requirements for the tau control region are summarized in Table 3.10.

	1 b tag	2 b tag
Muon	$p_t > 30$ GeV $\|\eta\| < 2.4$ tightId	$p_t > 30$ GeV $\|\eta\| < 2.4$ tightId
Electron	$p_t > 30$ GeV $\|\eta\| < 2.5$ tightId	$p_t > 30$ GeV $\|\eta\| < 2.5$ tightId
HR	>200 GeV	>200 GeV
Jets	R1	R2

Table 3.10: Requirements for the tau control region.

3.3.4 Multijet control region

The last control region contains mainly events from the QCD simulations; the events are selected in the following way:

- Events with at least one good charged lepton or photon are vetoed.
- There must be a missing transverse energy $E_T^{miss} > 200$ GeV.
- The condition on the jets differs from the R1 and the R2 selection, as the minimum angular distance between the jets and E_T^{miss} is required to be small ($\min \Delta\Phi < 0.5$). The other conditions on jets are the same as the R1 and the R2 selections.

The requirements for the multijet control region are summarized in Table 3.11.

	1 b tag	2 b tag
Charged leptons or photons	veto	veto
E_T^{miss}	>200 GeV	>200 GeV
Jets	R1 except: $\min \Delta\Phi(jet, E_T^{miss}) < 0.5$	R2 except: $\min \Delta\Phi(jet, E_T^{miss}) < 0.5$

Table 3.11: Requirements for the multijet control region.

3.3.5 Normalization

In each of the control regions a different kind of MC samples is the main source of signal, and can be studied, at first approximation, as if it was the only source: the DY sample for the region, the WjetsTolnu samples for the region, the TT and ST samples for the tau region, and the QCD samples for the multijet region. For the first three regions, an iterative process was carried out: 8 100-GeV-wide regions, separated in hadronic recoil, were defined, starting from a lower limit of $HR = 200$ GeV. The first region to be considered was the Ztonunu control region: the ratio between the number data events and DY weighted events was computed for every 100-GeV region, after having subtracted the contribution of all other MC samples (except the QCD samples, which were not considered during the iteration process) from the data. The ratios are reported in Table 3.12.
The DY and ZToNuNu samples were renormalized by multiplying the number of events, sorted by HT, by the right ratio. After that, the $W \to \mu\mu$ control region was considered, and the same procedure was applied: this time the ratio between MC and the data was computed for the WTolnu samples,

Hadronic recoil (GeV)	Weighted number of DY events	Number of data events after subtraction	Ratio data/MC
>200 and ≤300 GeV	52446.1	35899.5980	0.6845
>300 and ≤400 GeV	10091	6770.1139	0.6709
>400 and ≤500 GeV	2720.73	1731.7684	0.6365
>500 and ≤600 GeV	850.749	538.1829	0.6326
>600 and ≤700 GeV	282.18	223.0040	0.7903
>700 and ≤800 GeV	117.926	64.5216	0.5471
>800 and ≤900 GeV	42.1164	25.8330	0.6134
>900 and ≤1000 GeV	25.2698	15.2608	0.6039

Table 3.12: Comparison between the events in the DY sample and in the data samples (after substraction) in the first iteration.

Hadronic recoil (GeV)	Weighted number of DY events	Number of data events after subtraction	Ratio data/MC
>200 and ≤300 GeV	244414.8	101947.4960	0.4171
>300 and ≤400 GeV	40929.2990	15450.1668	0.3775
>400 and ≤500 GeV	9969.9940	3413.1726	0.3423
>500 and ≤600 GeV	2959.9130	903.8701	0.3054
>600 and ≤700 GeV	1012.8953	306.3698	0.3025
>700 and ≤800 GeV	432.1596	120.6689	0.2792
>800 and ≤900 GeV	192.5803	42.5649	0.2210
>900 and ≤1000 GeV	92.0201	22.6692	0.2464

Table 3.13: Comparison between the events in the W decay samples and in the data samples (after subtraction) in the first iteration. The correction factors in Table 3.12 were already applied to the Z decay samples.

while the other samples were subtracted from the data; the results are reported in Figure 3.13. The Wtolnu samples were renormalized accordingly before considering the top control region, where ST and TT were compared with data, after subtracting the other MC contributions; the results are reported in Figure 3.14.

Hadronic recoil (GeV)	Weighted number of WtoLepNu events	Number of data events after subtraction	Ratio data/MC
>200 and ≤300 GeV	7970.9247	4150.9447	0.5208
>300 and ≤400 GeV	1898.3675	1012.5670	0.5334
>400 and ≤500 GeV	531.6101	301.7808	0.5677
>500 and ≤600 GeV	192.3741	66,6926	0.3467
>600 and ≤700 GeV	73.7379	35.1112	0.4762
>700 and ≤800 GeV	26.9260	14.7549	0.5480
>800 and ≤900 GeV	18.6741	4.1984	0.2248
>900 and ≤1000 GeV	6.5079	5.8884	0.9048

Table 3.14: Comparison between the events in the top decay samples and in the data samples (after substraction) in the first iteration. The correction factors in Table 3.12 and Table 3.13 were already applied to the Z decay samples and the W decay samples respectively.

The TT and ST samples were renormalized, and then the whole process was reiterated, in order to refine the normalization process. The resulting plots for the Z mass and transverse momentum for the $Z \to \nu\nu$ control region, and the W mass and the missing transverse energy in the $W \to \mu\nu$ control region, after the two iterations, are shown in Figure 3.4 through Whadcorrettacomp. The Figures also show the hadronic recoil and the number of cleaned jet distribution in the same regions.

After finding the renormalization factors for the Z decay, W decay and top decay samples, the QCD samples were considered, studying the multijet control region: calculating the ratios between the QCD events, and the data events (after subtracting the other renormalized samples), also the renormalization factors for the QCD samples were found; since the other renormalization factors were fixed, this operation did not obviously require an iteration. For this phase the missing energy, instead of the hadronic recoil, was used to study eight regions separately. The ratio between QCD and data samples are reported in Table 3.15, while in Figure 3.8 the difference between the missing energy distribution in the multijet control region before (left) and after (right) the QCD samples renormalization is shown.
In Table 3.16 the resulting renormalization factors for all the MC samples are reported.
In the following pages (Figures 3.9 through Zcorrettacomp27) some variables' distributions in the Z, W and top control regions are shown, with the

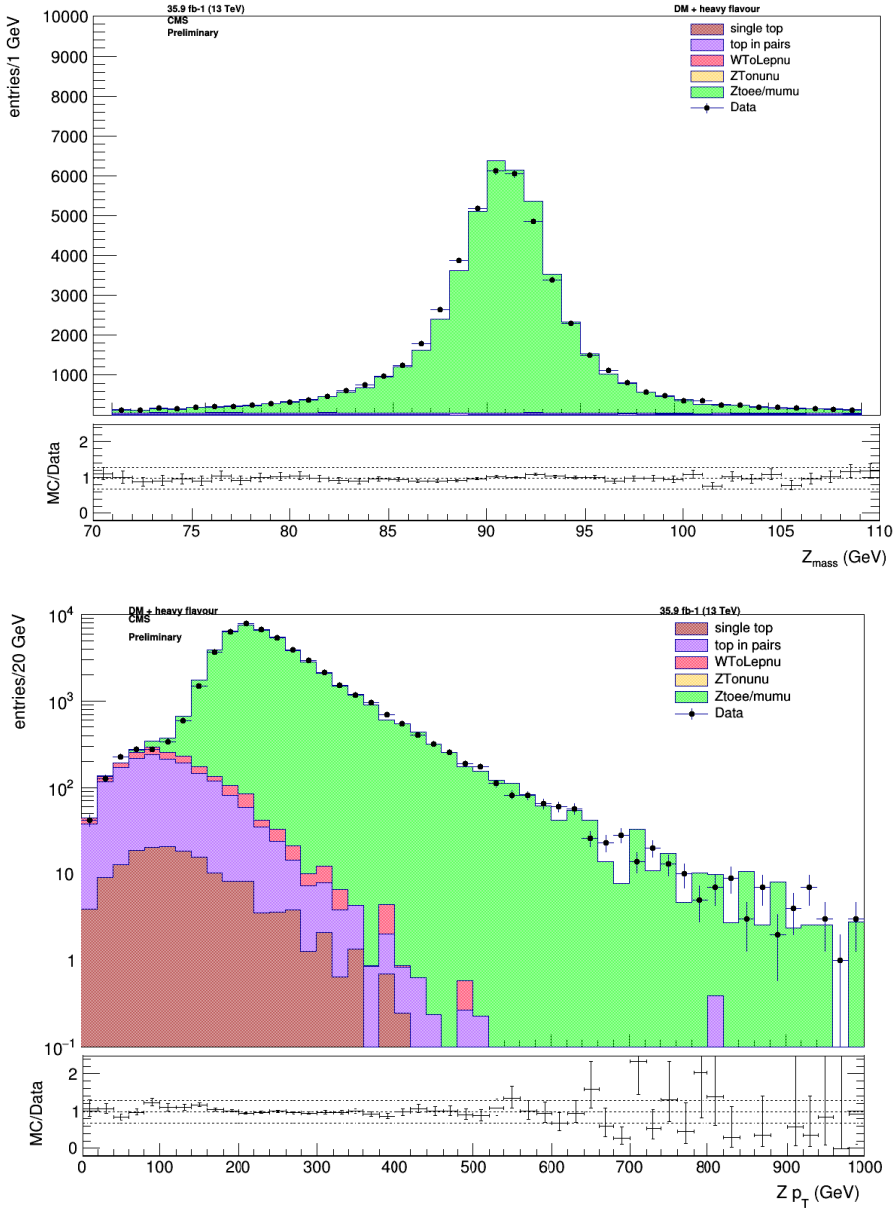

Figure 3.4: Above: Distributions of Z mass (above) and Z transverse momentum (below) after the renormalization. The selection on jets (R1 or R2) was not applied.

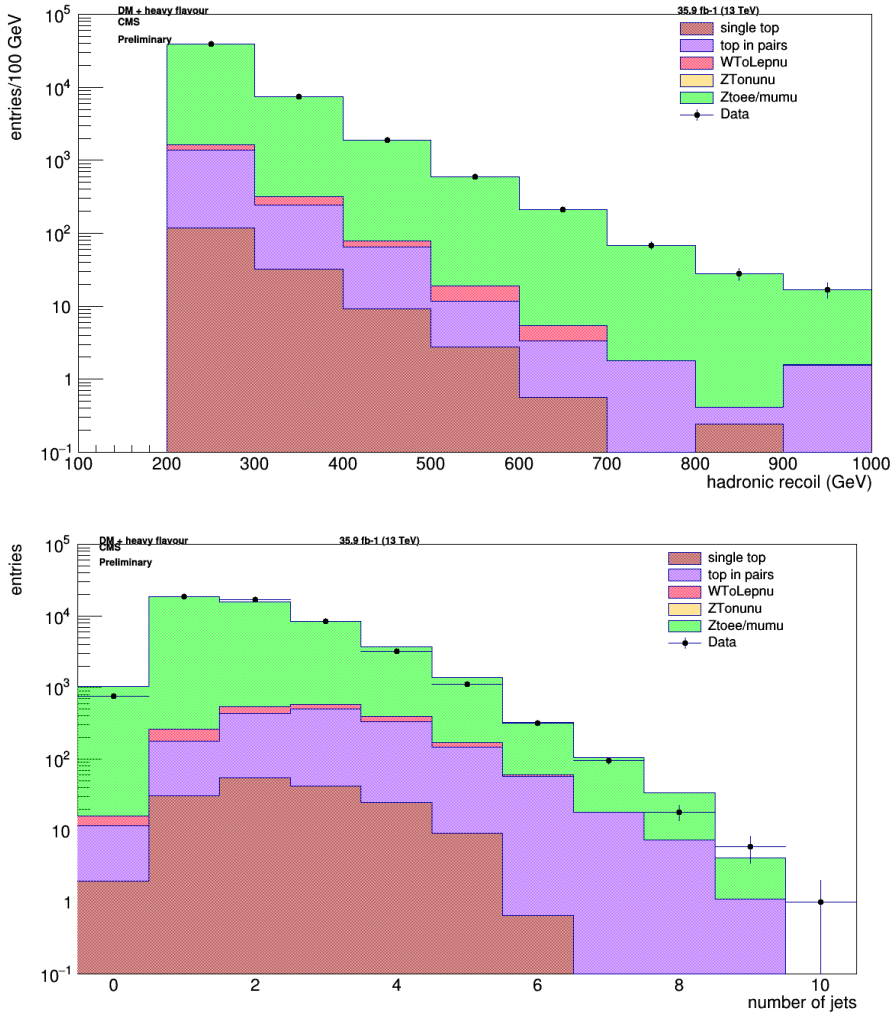

Figure 3.5: Distribution of the hadronic recoil (above) and of the number of jets (below) for the $Z \to \mu\mu$ control region after the renormalization, without the selection on jets (R1 or R2).

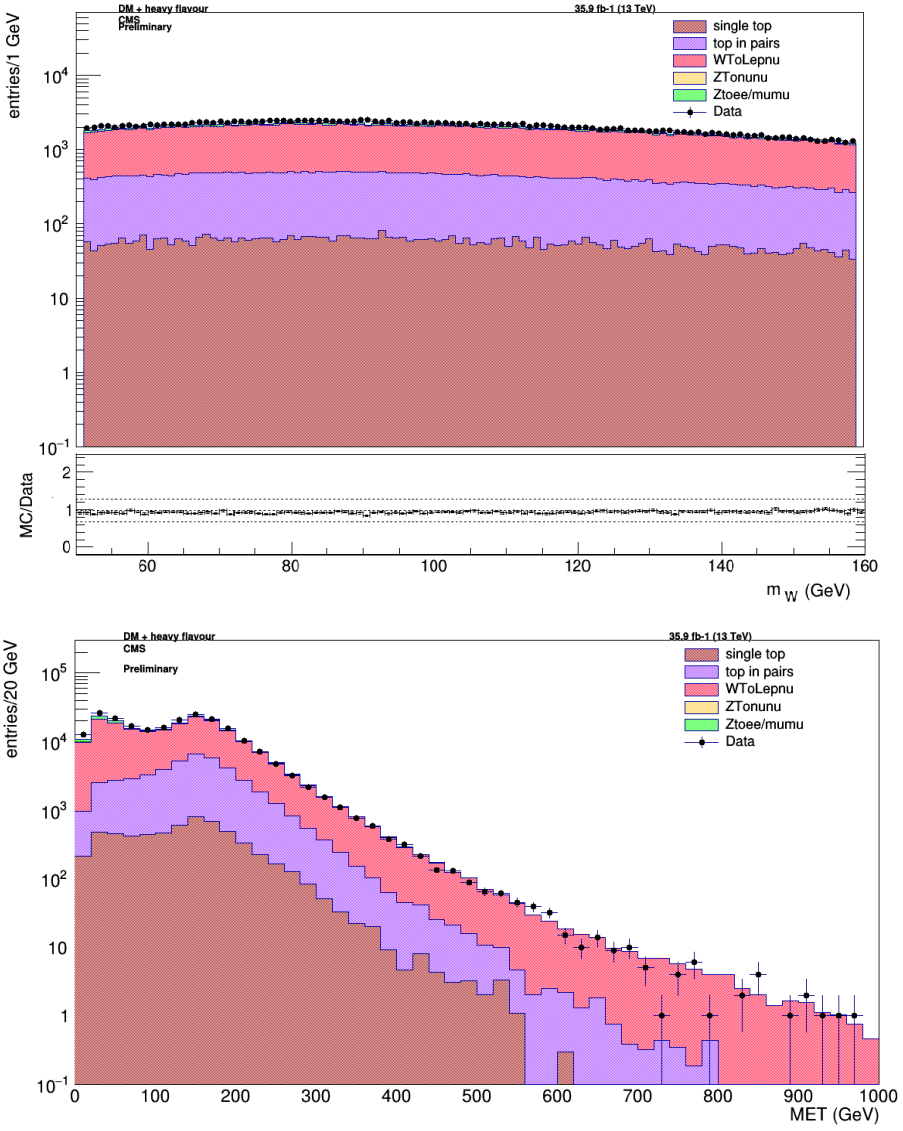

Figure 3.6: Above: Distributions of Z mass (above) and Z transverse momentum (below) after the renormalization. The selection on jets (R1 or R2) was not applied.

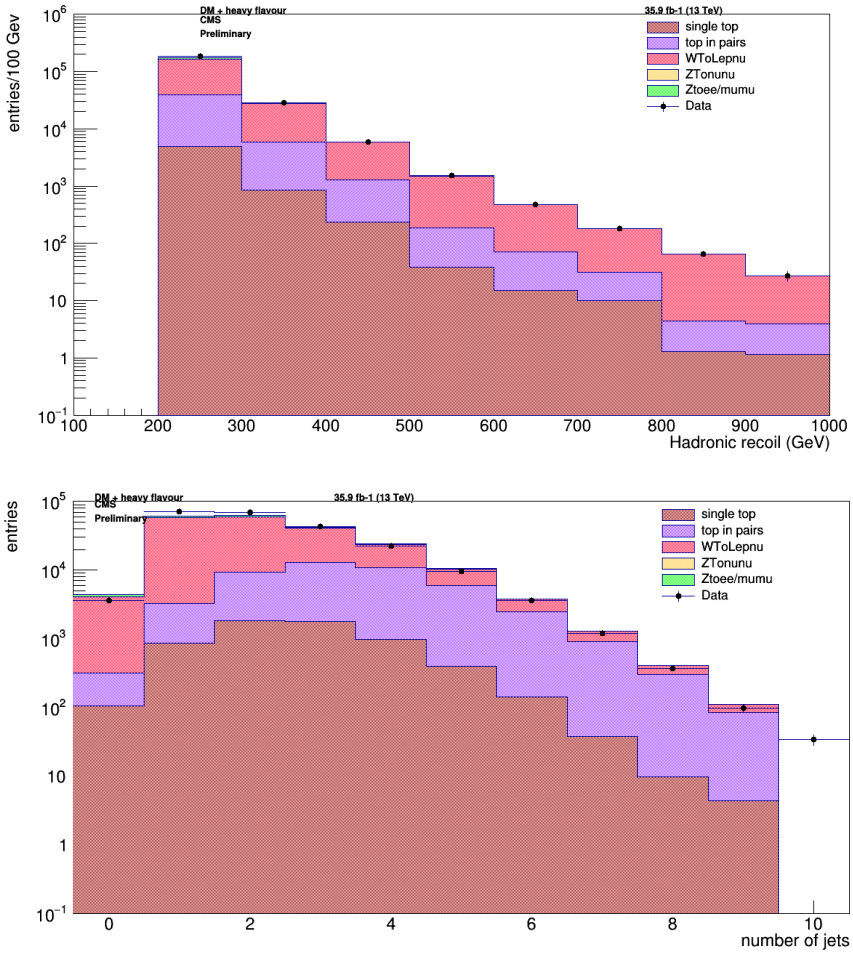

Figure 3.7: Distribution of the hadronic recoil (above) and of the number of jets (below) for the $Z \to \mu\mu$ control region after the renormalization, without the selection on jets (R1 or R2).

Missing energy (GeV)	Weighted number of QCD events	Number of data events after subtraction	Ratio data/MC
>200 and ≤300 GeV	24135	25126.5	1.04
>300 and ≤400 GeV	1753.16	2391.37	1.36
>400 and ≤500 GeV	302.56	420.882	1.39
>500 and ≤600 GeV	61.4114	101.113	1.65
>600 and ≤700 GeV	21.1503	44.8641	2.12
>700 and ≤800 GeV	12.2935	11.1521	0.91
>800 and ≤900 GeV	5.60476	15.9158	2.84
>900 and ≤1000 GeV	2.80238	3.46401	1.24

Table 3.15: Comparison between events in QCD samples and the data samples, after subtraction, both selected with the multijet control region constraints. The right column reports the ratio between the two samples; the last two ratios were not computed, as the number of QCD events is zero.

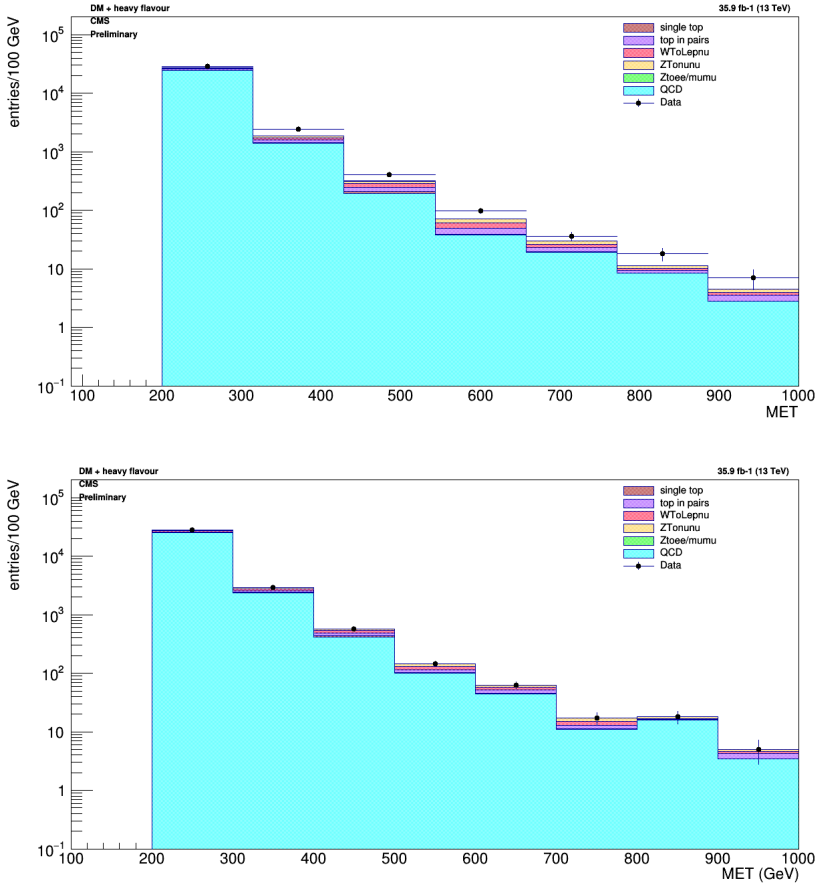

Figure 3.8: Above: distribution of E_T^{miss} in the multijet region before the QCD samples renormalization; below: distribution of E_T^{miss} in the multijet region after the QCD samples renormalization

Missing energy /hadronic recoil (GeV)	Z decays samples	W decays samples	Top decay samples	QCD samples
>200 and ≤300 GeV	0.71	0.52	0.50	1.04
>300 and ≤400 GeV	0.70	0.53	0.50	1.36
>400 and ≤500 GeV	0.66	0.45	0.54	1.39
>500 and ≤600 GeV	0.68	0.45	0.30	1.65
>600 and ≤700 GeV	0.74	0.39	0.43	2.12
>700 and ≤800 GeV	0.56	0.35	0.52	0.91
>800 and ≤900 GeV	0.65	0.32	0.19	2.84
>900 and ≤1000 GeV	0.61	0.25	0.90	1.24

Table 3.16: Renormalization factors for all the MC samples.

application of either the R1 or the R2 selections for jets. The agreement between the MC and data samples for the three control regions appears to be satisfactory also with those additional requirements.

Z control region, R1

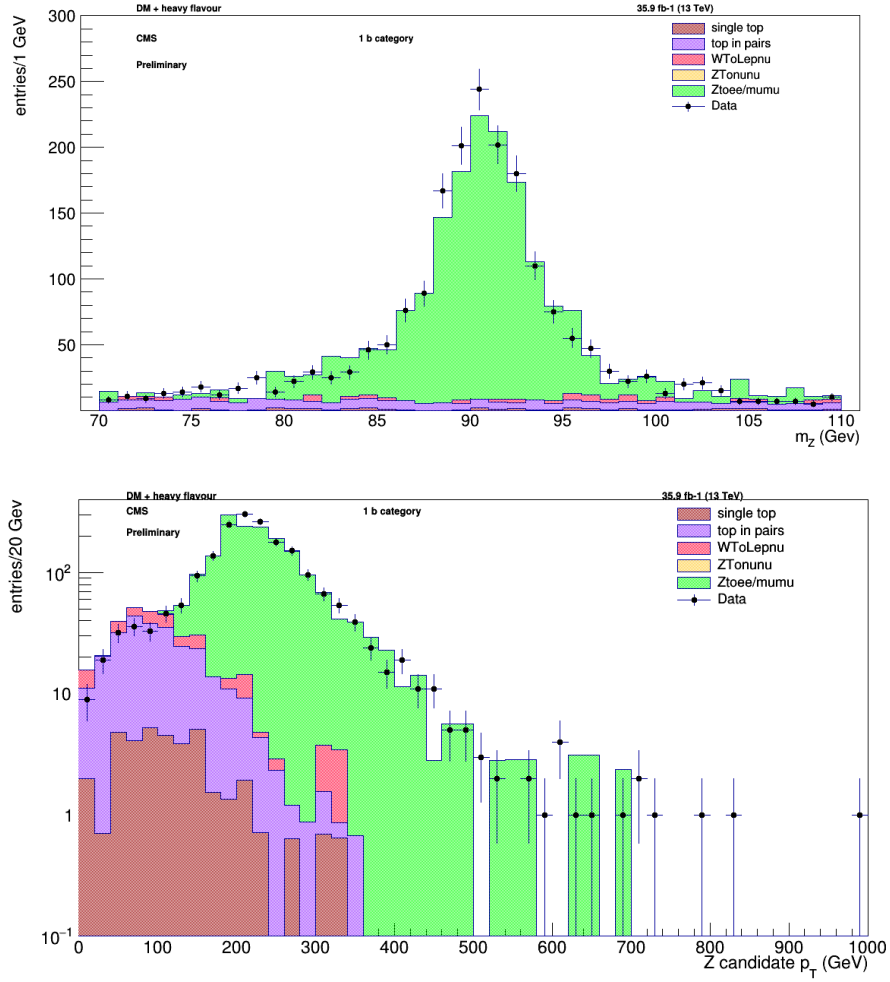

Figure 3.9: Distributions of Z mass (above) and Z transverse momentum (below) after the renormalization, with the 1 b tag selection (R1).

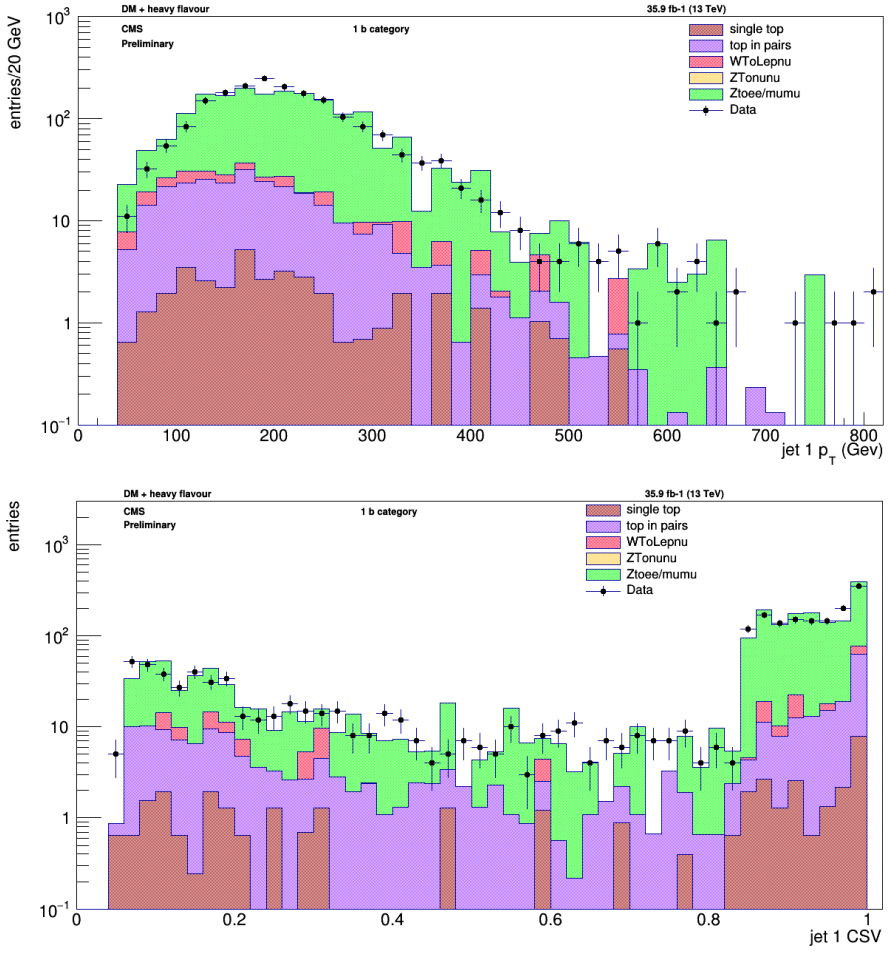

Figure 3.10: Distributions of the the leading jet transverse momentum (above) and CSV (below) after the renormalization, with the 1 b tag selection.

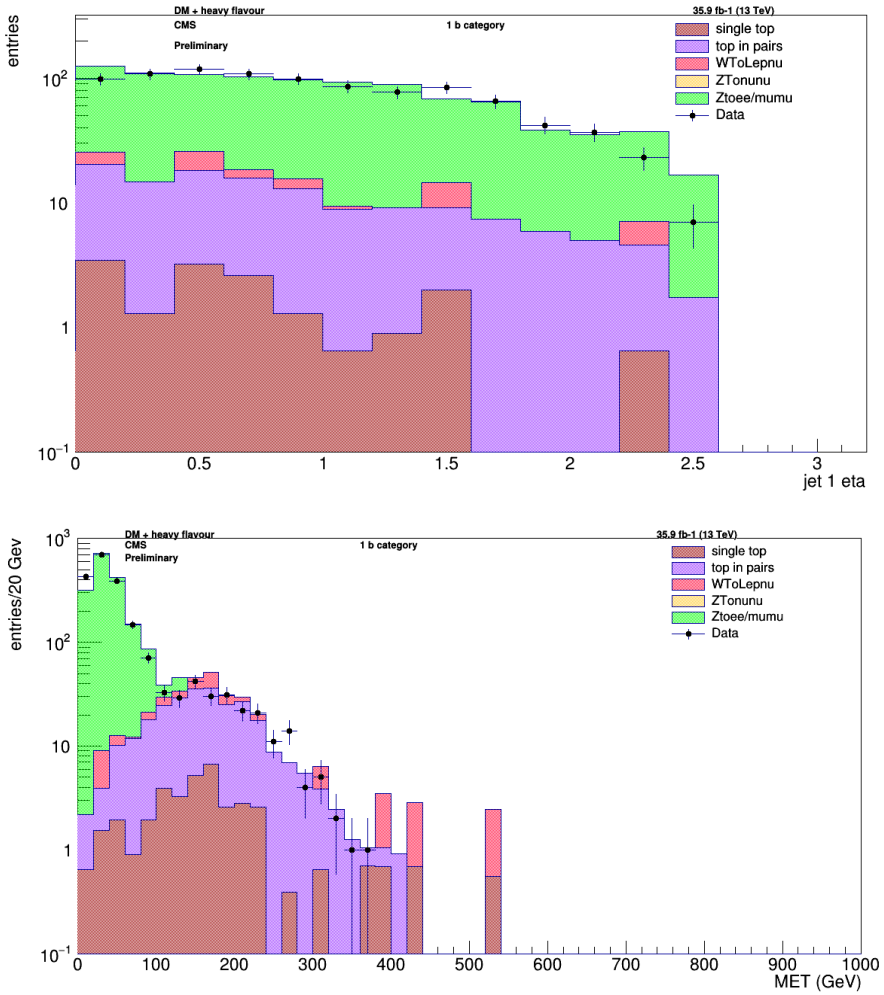

Figure 3.11: Distributions of the leading jet pseudorapidity (above) and of the missing transverse energy (below) after the renormalization, with the 1 b tag selection.

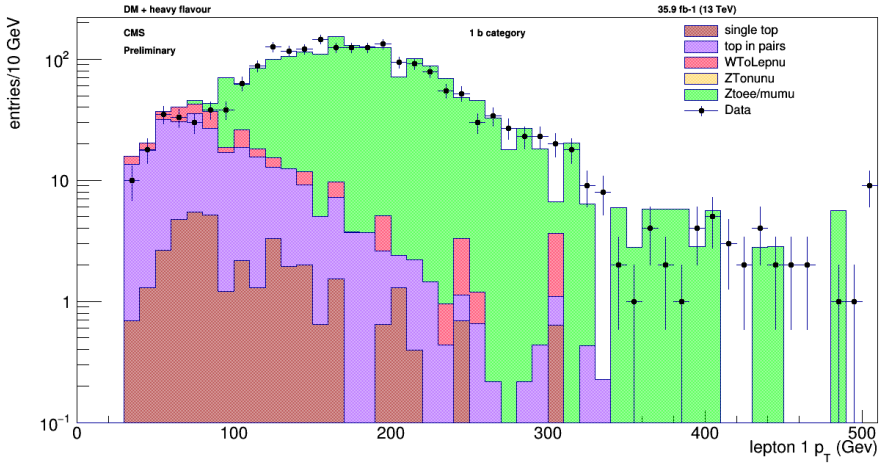

Figure 3.12: Distribution of the leading muon tranverse momentum after the renormalization, with the 1 b tag selection.

Z control region, R2

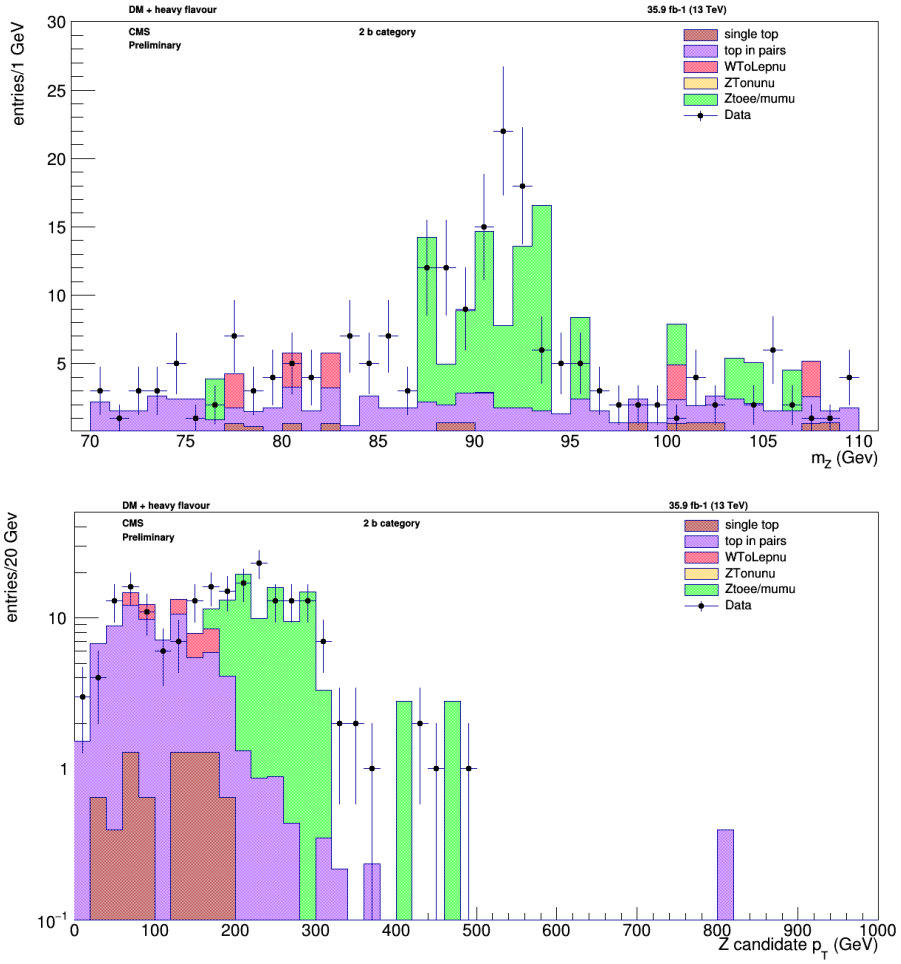

Figure 3.13: Distributions of Z mass (above) and Z transverse momentum (below) after the renormalization, with the 2 b tags selection.

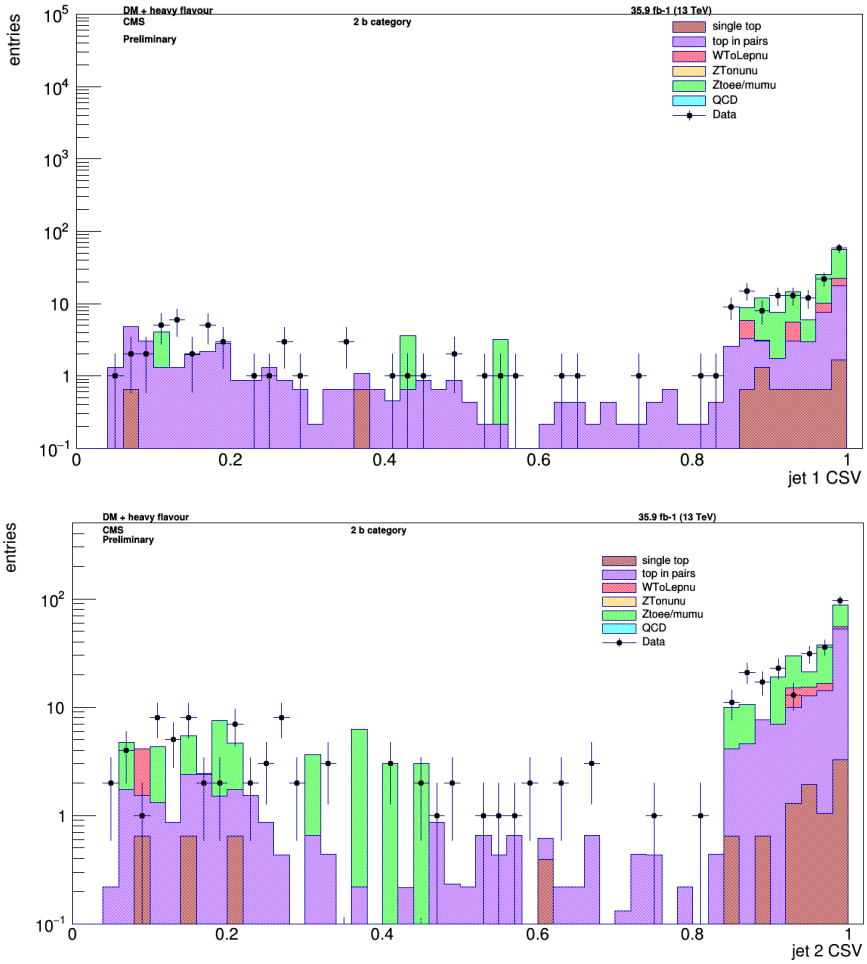

Figure 3.14: Distributions of CSV of the leading jet (above) and of the subleading jet (below) after the renormalization, with the 2 b tags selection.

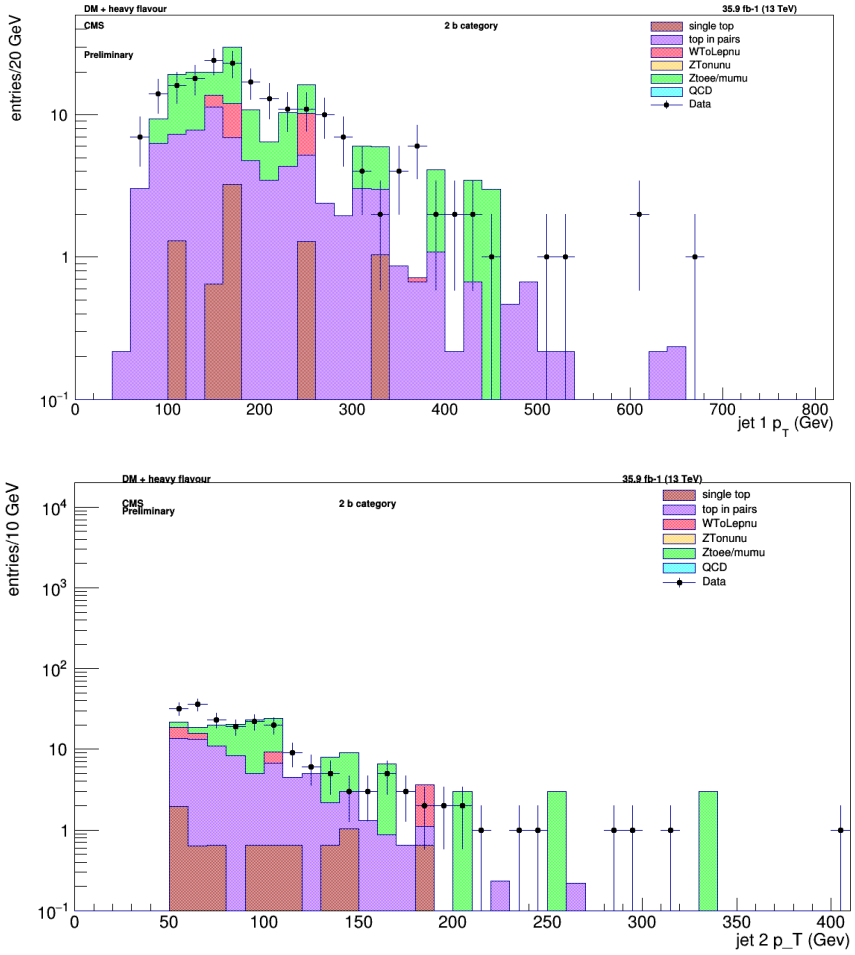

Figure 3.15: Distributions of the transverse momentum of the leading jet (above) and of the subleading jet (below) after the renormalization, with the 2 b tags selection.

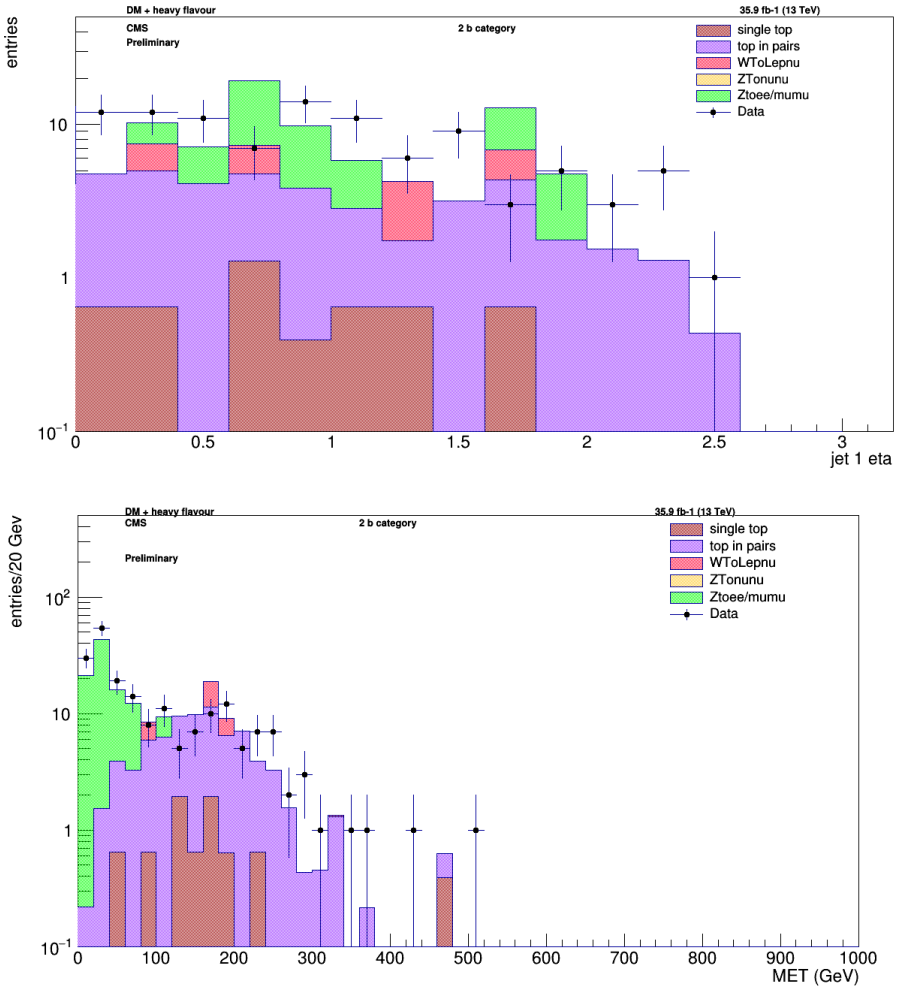

Figure 3.16: Distributions of the pseudorapidity of the leading jet (above) and of the missing transverse energy (below) after the renormalization, with the 2 b tags selection.

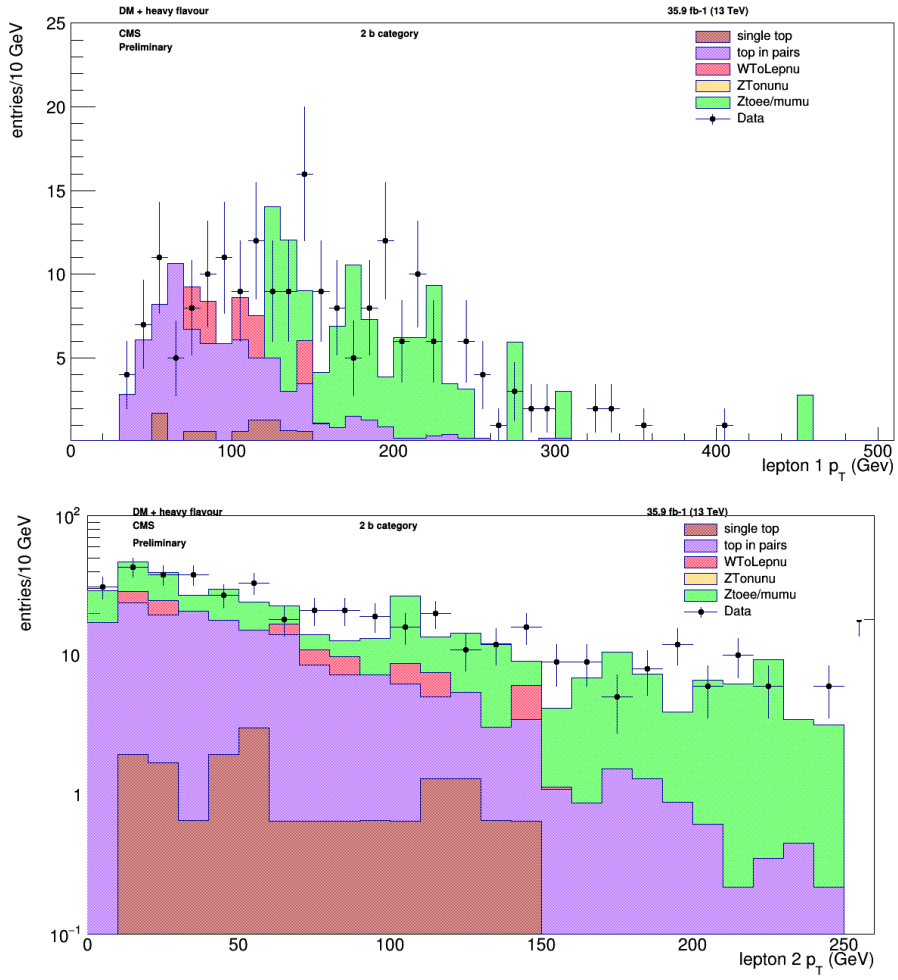

Figure 3.17: Distributions of the transverse momentum of the leading muon (above) and of the subleading muon (below) after the renormalization, with the 2 b tags selection.

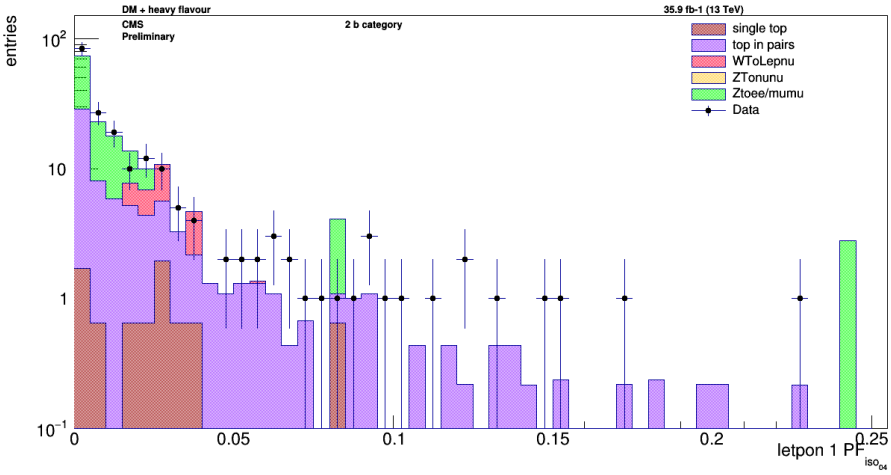

Figure 3.18: Distributions of the isolation of the leading muon after the renormalization, with the 2 b tags selection.

W control region, R1

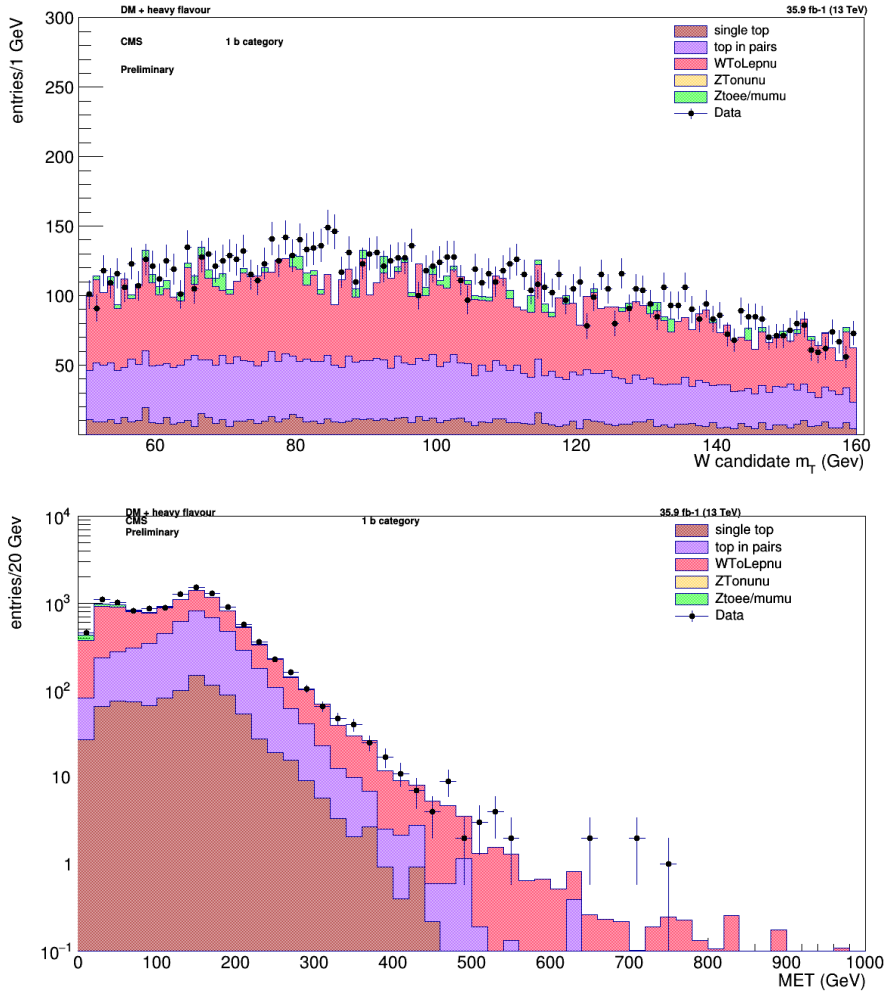

Figure 3.19: Distributions of W mass (above) and missing transverse energy (below) after the renormalization, with the 1 b tag selection.

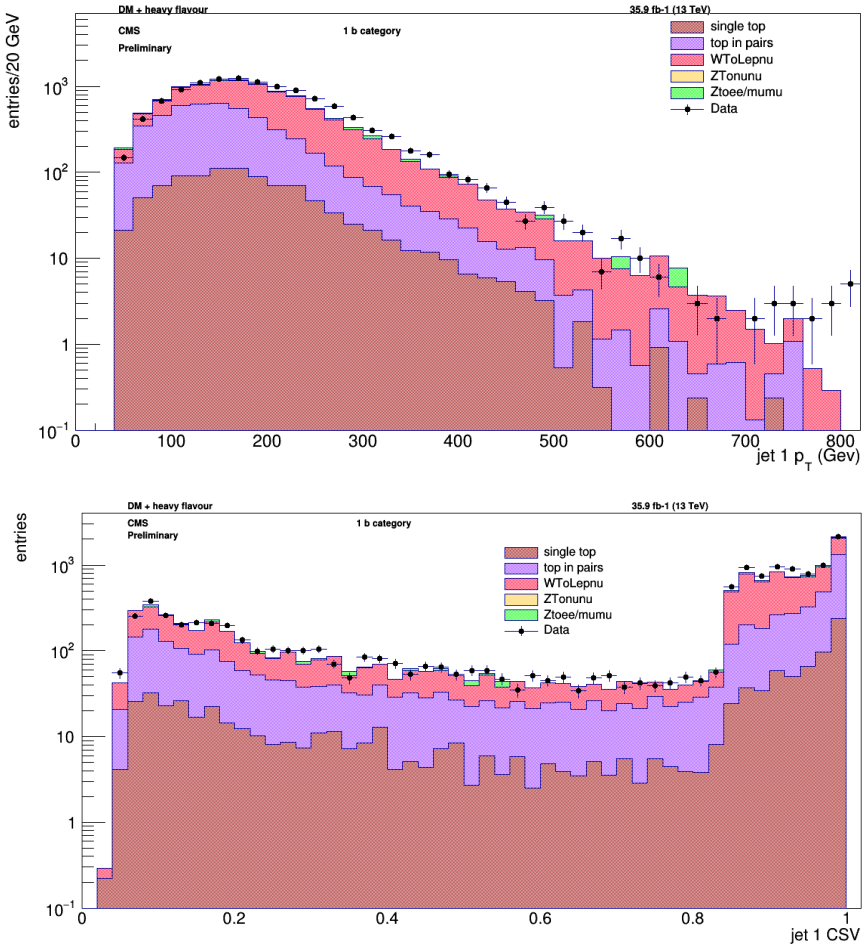

Figure 3.20: Distributions of the transverse momentum (above) and CSV (below) of the leading muon after the renormalization, with the 1 b tag selection.

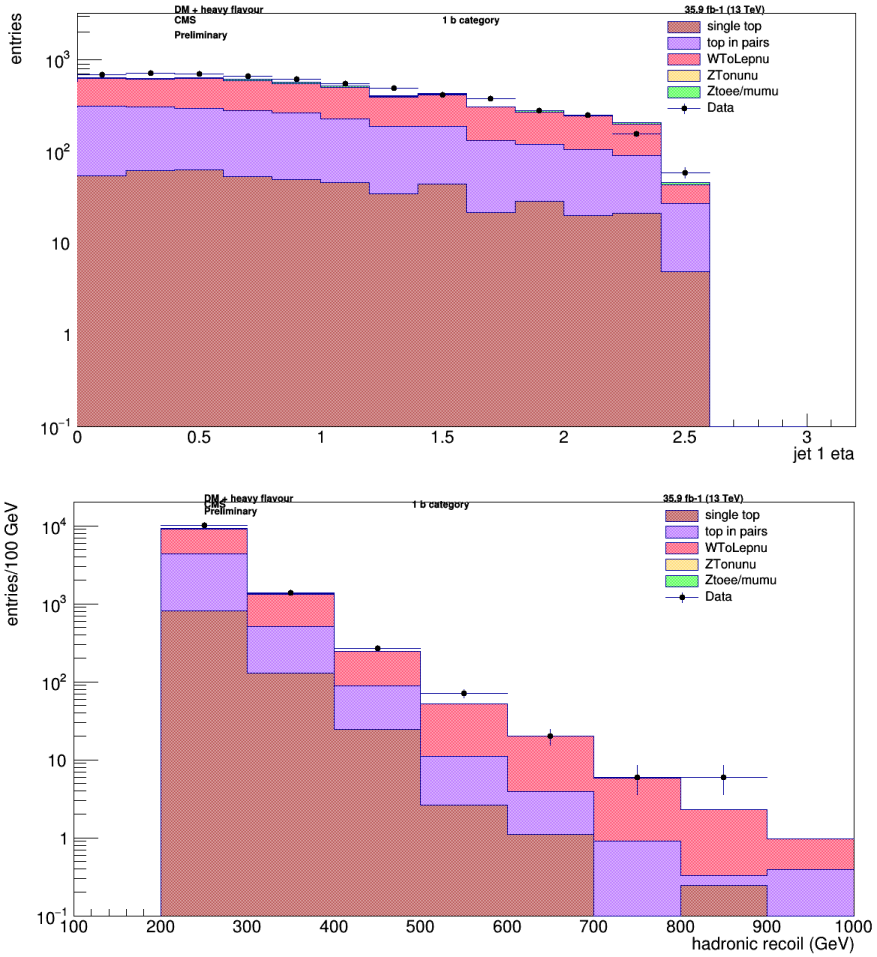

Figure 3.21: Distributions of the pseudorapidity of the leading jet (above) and of the hadronic recoil (below) after the renormalization, with the 1 b tag selection.

W control region, R2

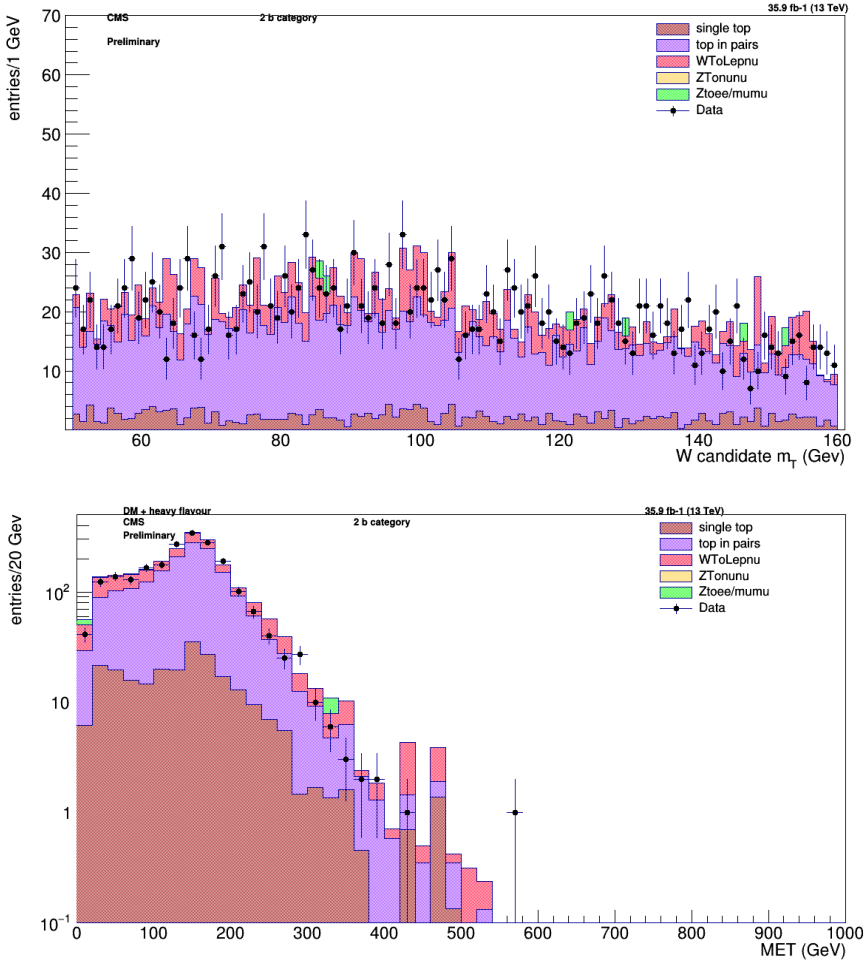

Figure 3.22: Distributions of W mass (above) and missing transverse energy (below) after the renormalization, with the 2 b tags selection.

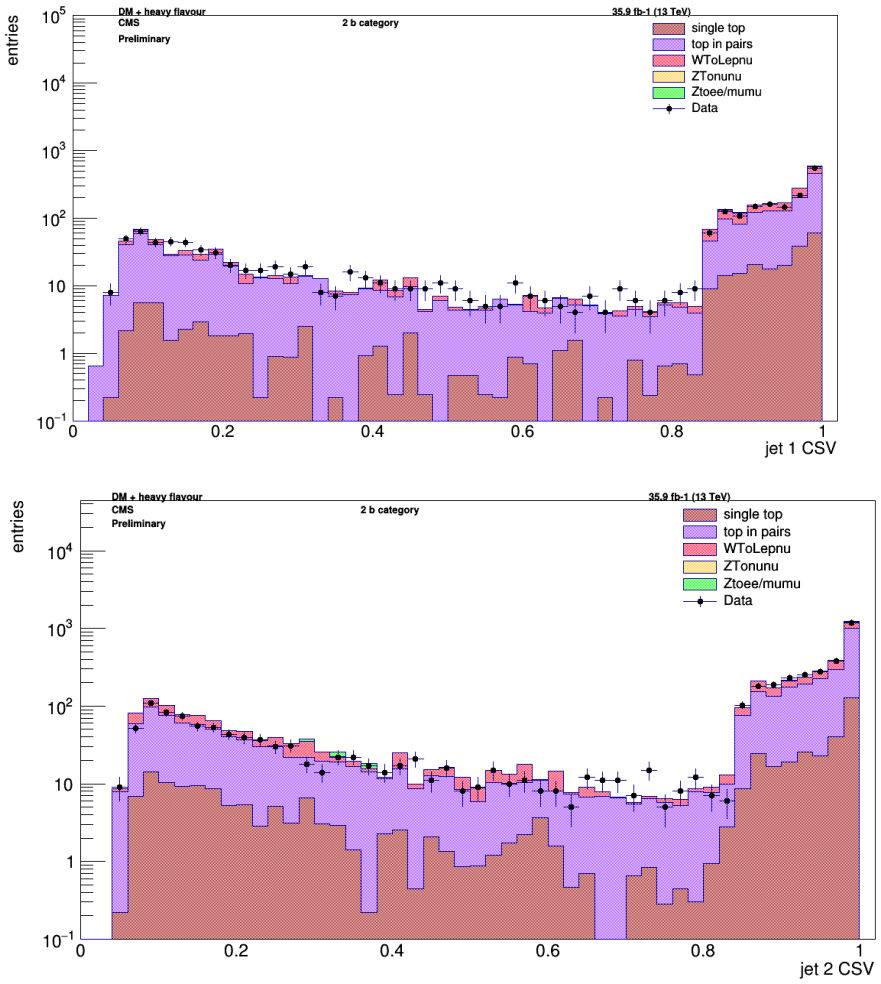

Figure 3.23: Distributions of CSV of the leading jet (above) and of the subleading jet (below) after the renormalization, with the 2 b tags selection.

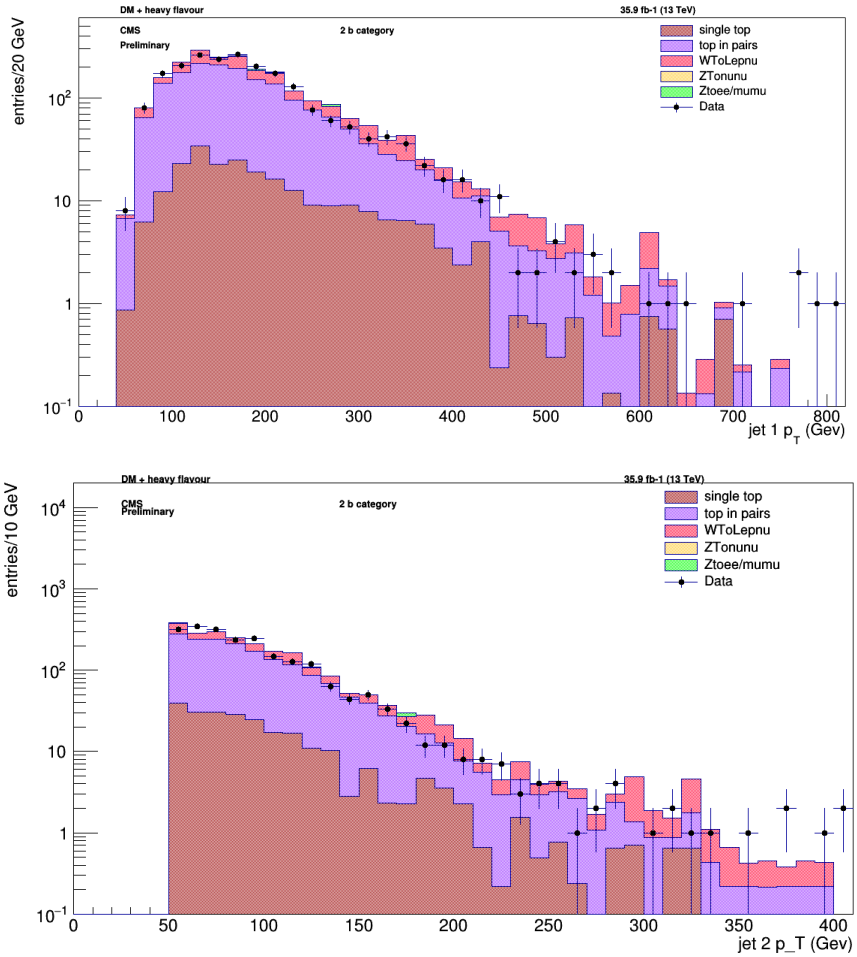

Figure 3.24: Distributions of the transverse momentum of the leading jet (above) and of the subleading jet (below) after the renormalization, with the 2 b tags selection.

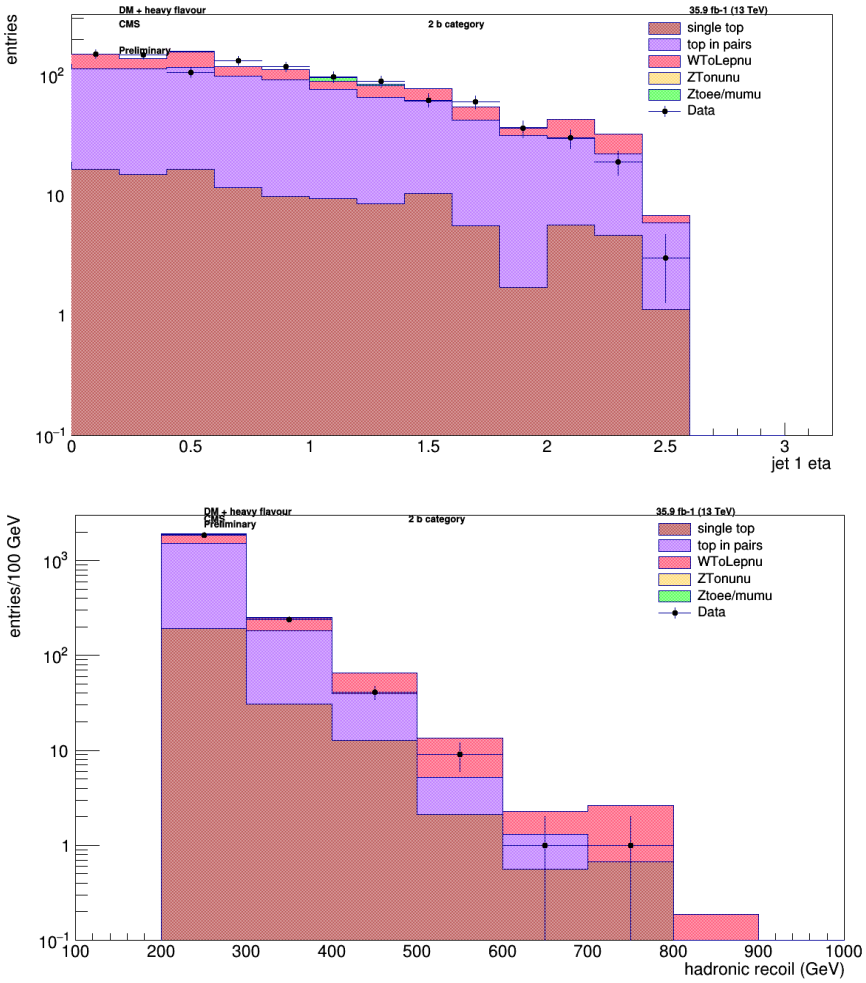

Figure 3.25: Distributions of the pseudorapidity of the leading jet (above) and of the hadronic recoil (below) after the renormalization, with the 2 b tags selection.

Top control region, R1

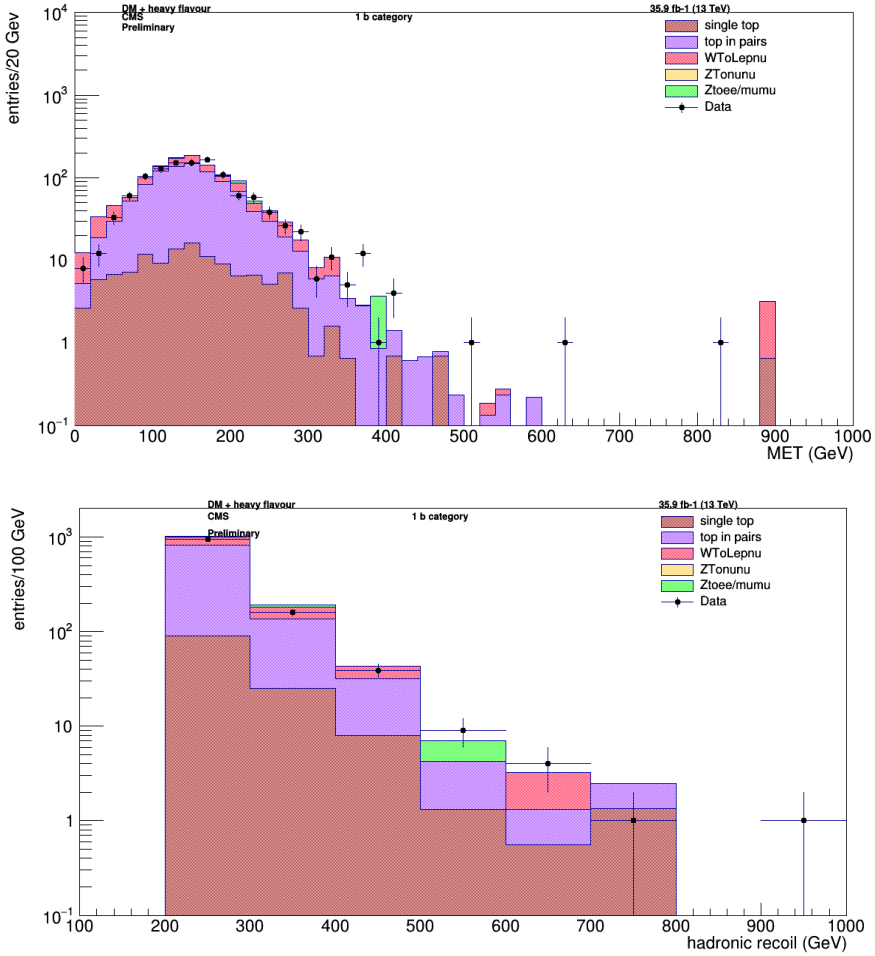

Figure 3.26: Distributions of the missing transverse energy (above) and of the hadronic recoil (below) after the renormalization, with the 1 b tag selection.

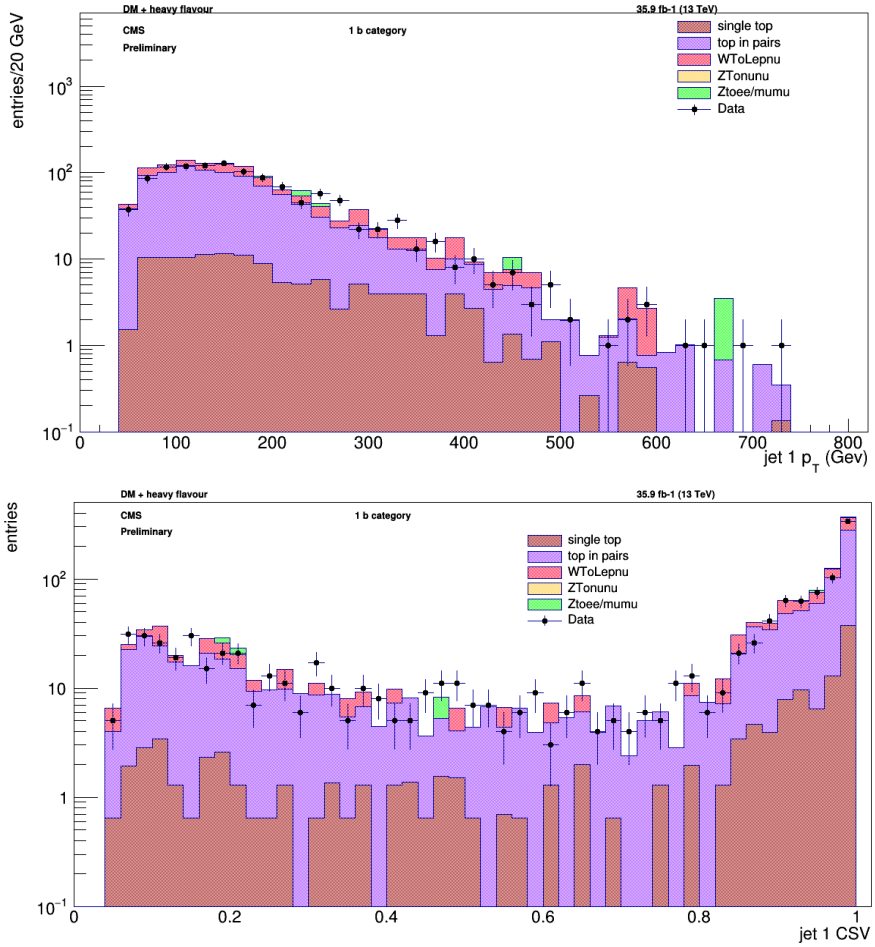

Figure 3.27: Distributions of the transverse momentum (above) and CSV (below) of the leading jet after the renormalization, with the 1 b tag selection.

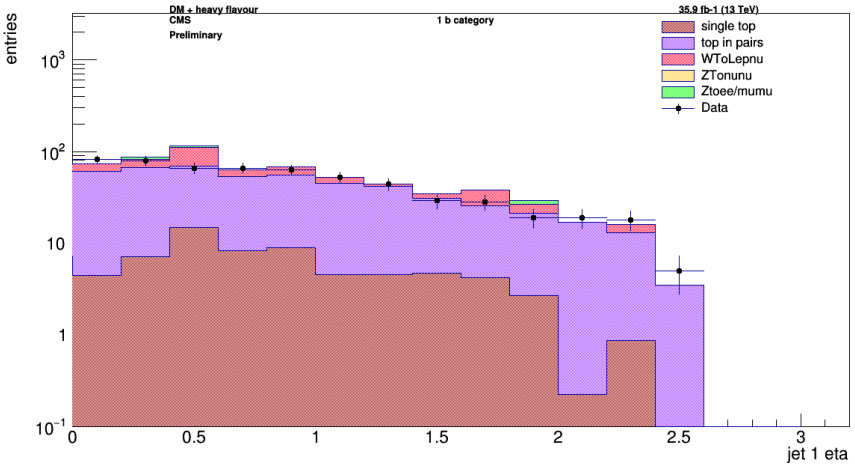

Figure 3.28: Distribution of the pseudorapidity of the leading jet after the renormalization, with the 1 b tag selection.

Top control region, R2

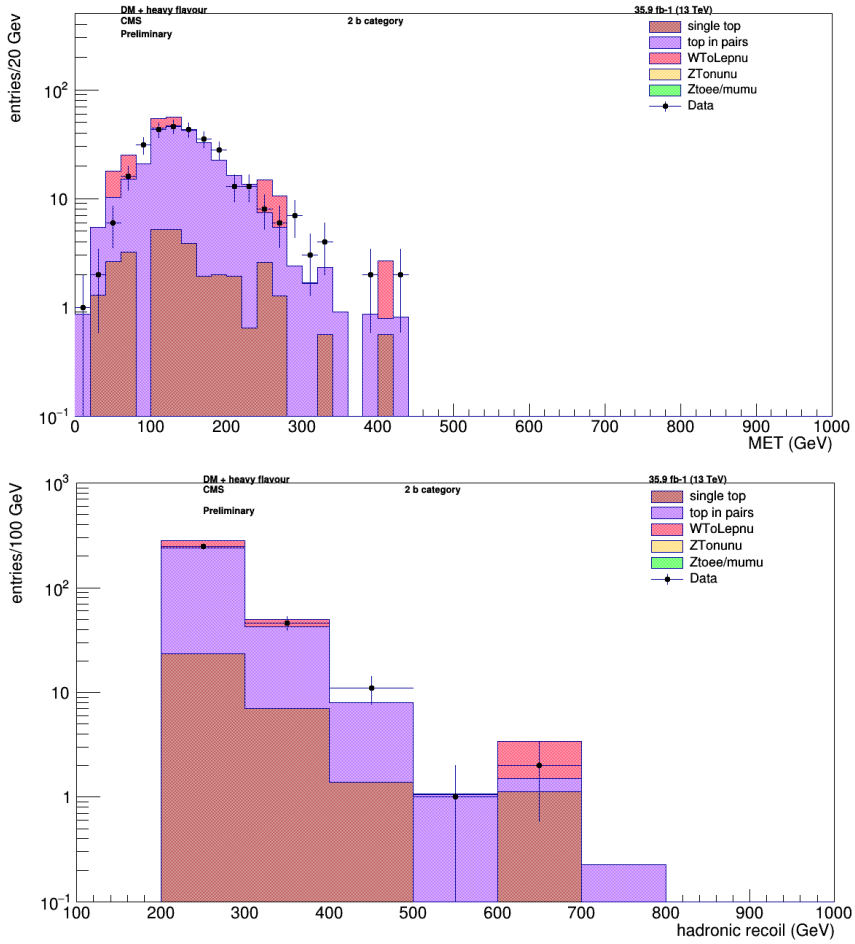

Figure 3.29: Distributions of the missing transverse energy (above) and of the hadronic recoil (below) after the renormalization, with the 2 b tags selection.

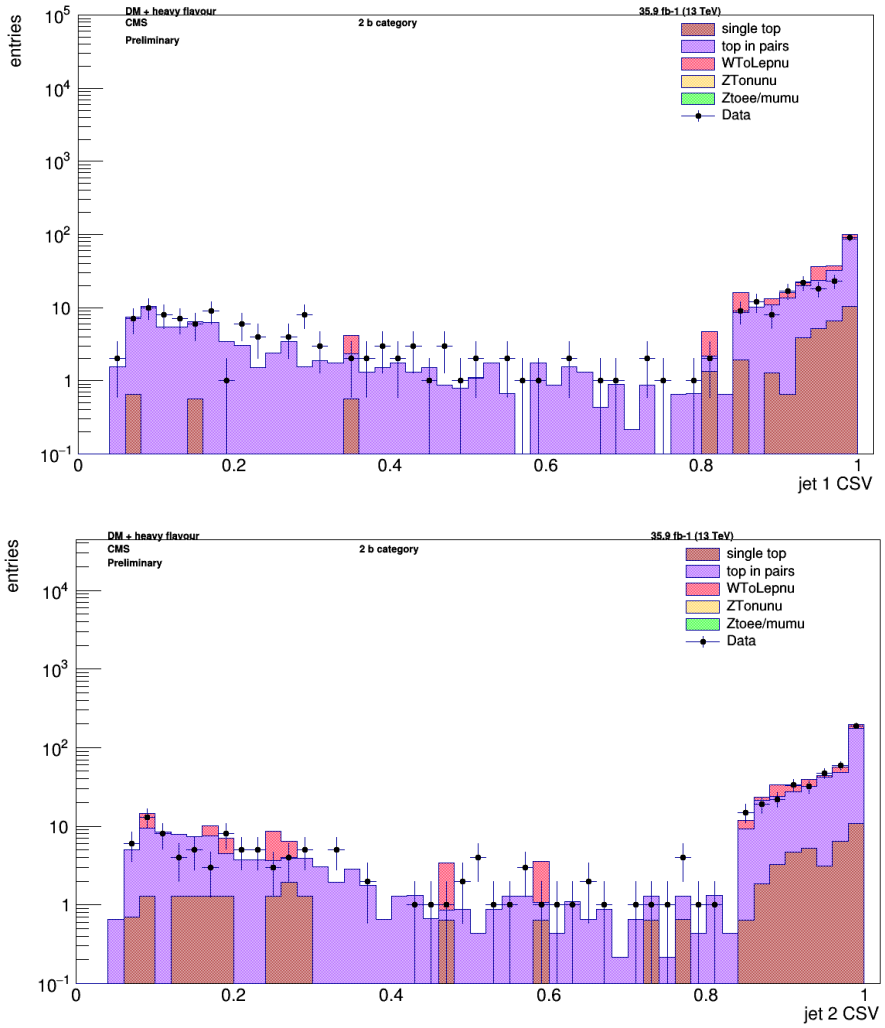

Figure 3.30: Distributions of the CSV of the leading jet (above) and of the subleading jet (below) after the renormalization, with the 2 b tags selection.

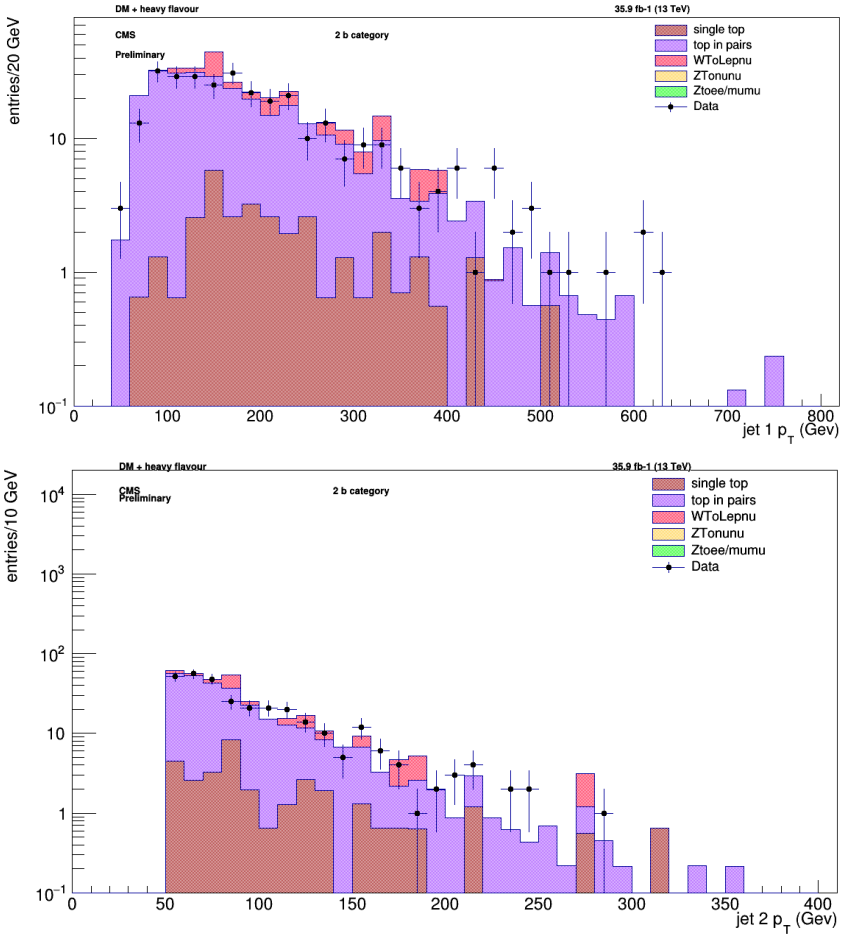

Figure 3.31: Distributions of the transverse momentum of the leading jet (above) and of the subleading after the renormalization, with the 2 b tags selection.

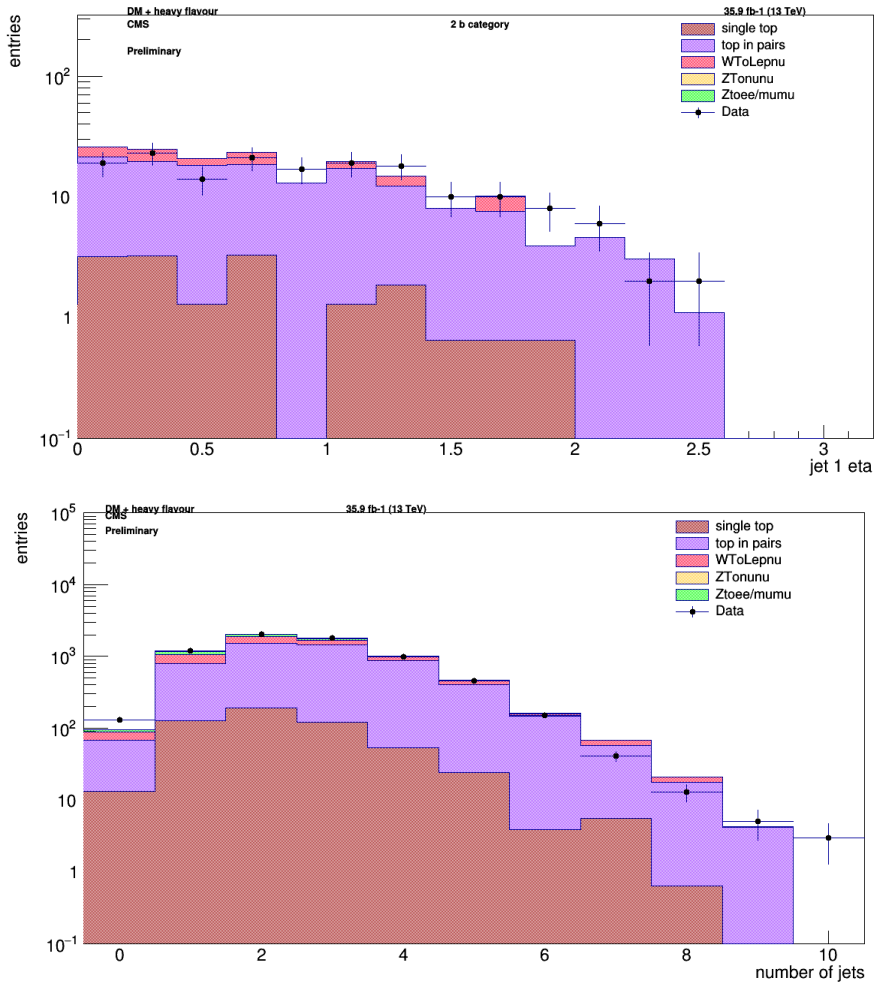

Figure 3.32: Distributions of the pseudorapidity of the leading jet (above) and of the number of cleaned jets (below) after the renormalization, with the 2 b tags selection.

3.4 Signal region

Once the MC simulations were normalized, the signal region was finally considered, whose events were selected by applying the following cuts:

- Events with at least one good charged lepton or photon are vetoed.
- There must be a missing transverse energy $E_T^{miss} > 200$ GeV.
- The condition on the jets are either the R1 or the R2 selection.

The requirements for the signal region are summarized in Table 3.17.

	1 b tag	2 b tag
Charged leptons or photons	veto	veto
E_T^{miss}	>200 GeV	>200 GeV
Jets	R1	R2

Table 3.17: Requirements for the signal region.

Here follow the resulting distributions of missing transverse energy in the signal region (Figure 3.33), with either the R1 or the R2 requirements, and the distribution of other interesting variables (Figures 3.34 - 3.38). While for the distribution of the E_T^{miss} with the 2 b tags selection (right histogram of Figure 3.33) the data seem to be consistent with the MC simulations, when it comes to the 1 b tag selection an excess of signal appears (left histogram of Figure 3.33). Nevertheless, the effect of systematic effects were not considered, hence this phenomenon could disappear after a more thorough analysis.

To complete the present work, a comparison with the expected signal if a DM particle is present (assuming it is a fermion with a mass $M_\chi = 1$ GeV); two cases are considered: the former assuming the mediator is a boson of mass $M_\Phi = 100$ GeV, the latter assuming it is a boson with a much larger mass, $M_\Phi = 10$ TeV. Since the models are much more sensitive to the mediator mass than to the DM particle mass, assuming $M_\chi = 1$ GeV for both cases is not so restrictive. The 2 samples, BBbarDMJets_scalar_Mchi-1_Mphi-100_TuneCUETP8M1_v2_13TeV-madgraphMLM-pythia8-v1 and BBbarDMJets_scalar_Mchi-1_Mphi-10000_TuneCUETP8M1_v2_13TeV-madgraphMLM-pythia8-v1 (respectively for the 100 GeV and the 10 TeV mediator), underwent the same object cleaning and selections that were applied to the background simulations and the data samples to obtain the signal region events. The E_T^{miss} distribution was then superimposed to the data and background, as in Figure 3.39 for the 100 GeV mediator and in Figure 3.40 for the 10 TeV mediator. Just as an exercise, the shapes were compared, and

the model with a 10-TeV-mass mediator seems to have a more similar trend to the data than the model with a 100-GeV-mass mediator, whose number of events decreases more rapidly in the high-energy range ($E_T^{miss} \geq 500$ GeV) for the 1 b tag region.

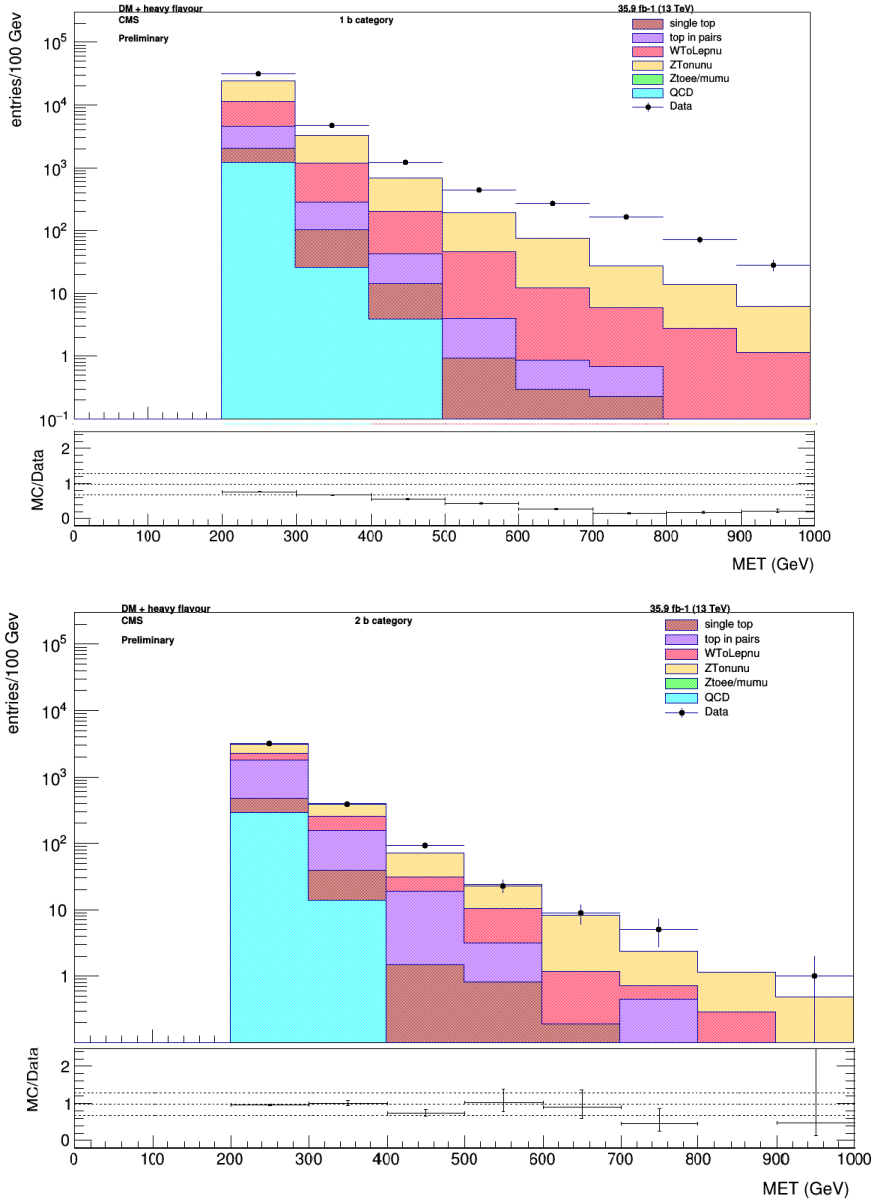

Figure 3.33: Missing transverse energy distribution in the signal region with the 1 b tag selection (above) and the 2 b tags selection (below).

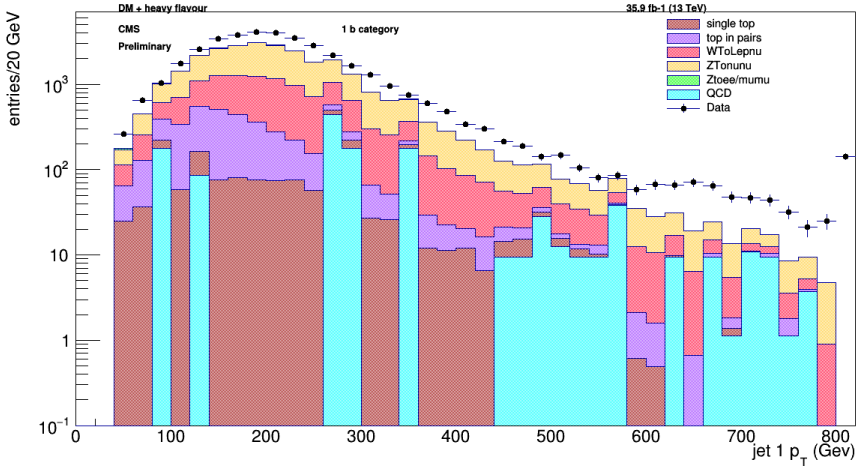

Figure 3.34: Leading jet transverse momentum distribution in the signal region with the 1 b tag selection.

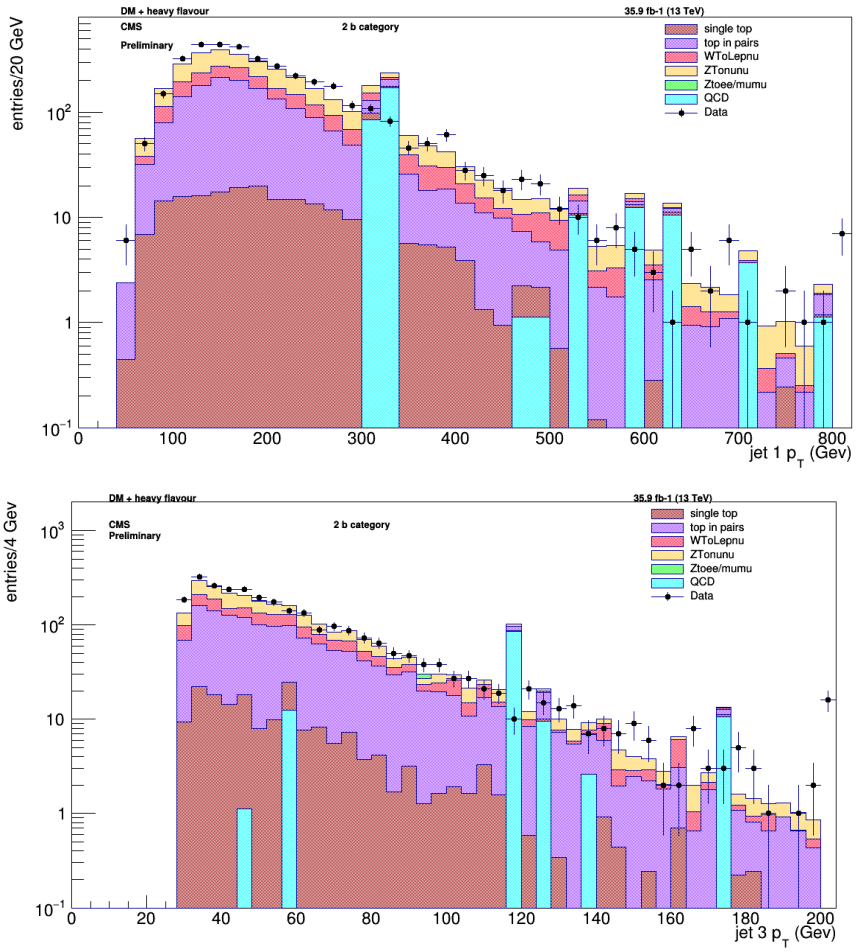

Figure 3.35: Leading (above) and third (below) jet transverse momentum distribution in the signal region with 2 b tags selection for jets.

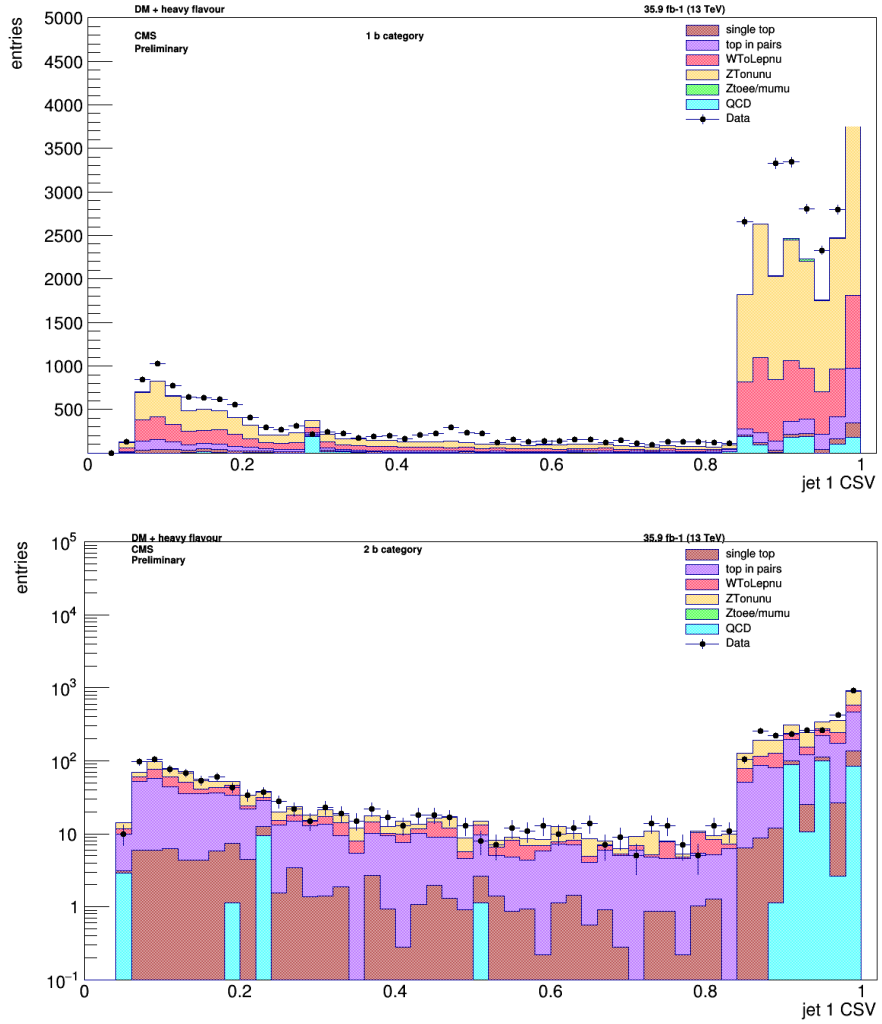

Figure 3.36: Leading jet CSV distribution for the signal region with the 1 b tag (above) and the 2 b tag (below) selection for jets.

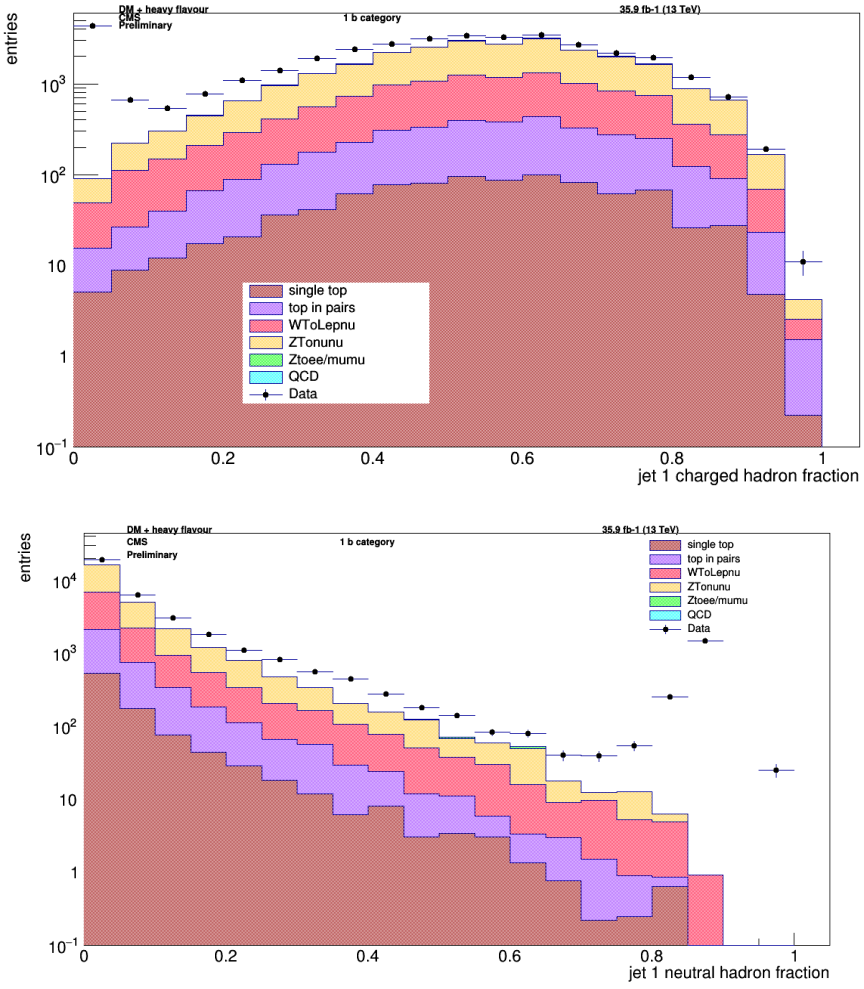

Figure 3.37: Charged (above) and neutral (below) hadronic energy fraction for the leading jet; both histograms refer to the the signal region with the 1 b tag selection for jet.

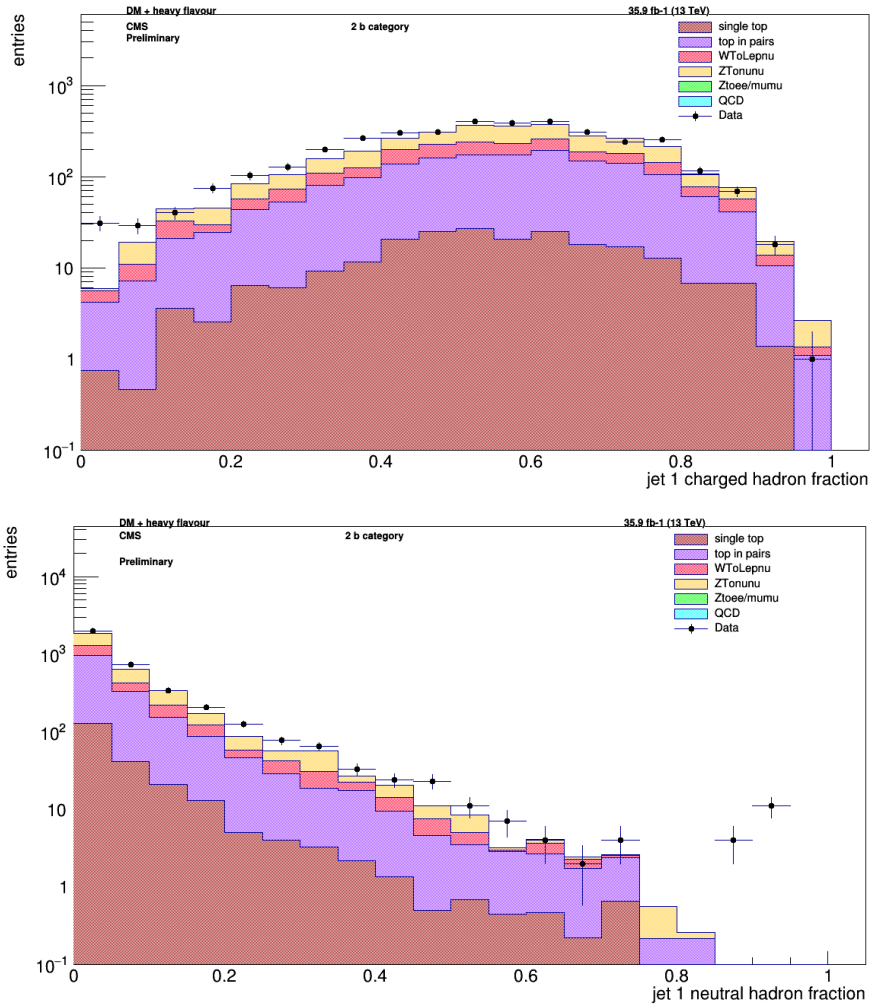

Figure 3.38: Charged (above) and neutral (below) hadronic energy fraction for the leading jet; both histograms refer to the the signal region with the 2 b tag selection for jet.

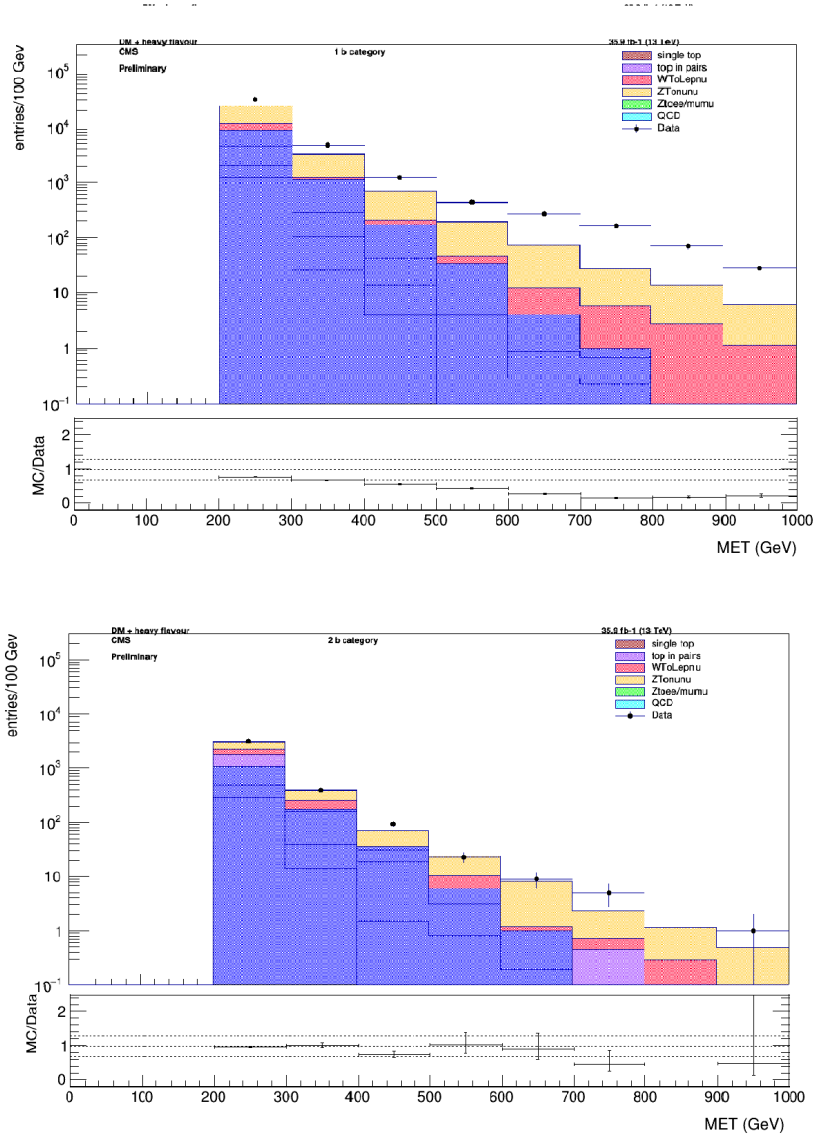

Figure 3.39: Distribution of E_T^{miss} for the MC sample simulating the presence of a fermionic DM particle with a scalar mediator of mass $M_\Phi = 100$ GeV, superimposed in blue color to the plots in Figure 3.33. The sample with the fermionic DM is plotted in arbitrary units.

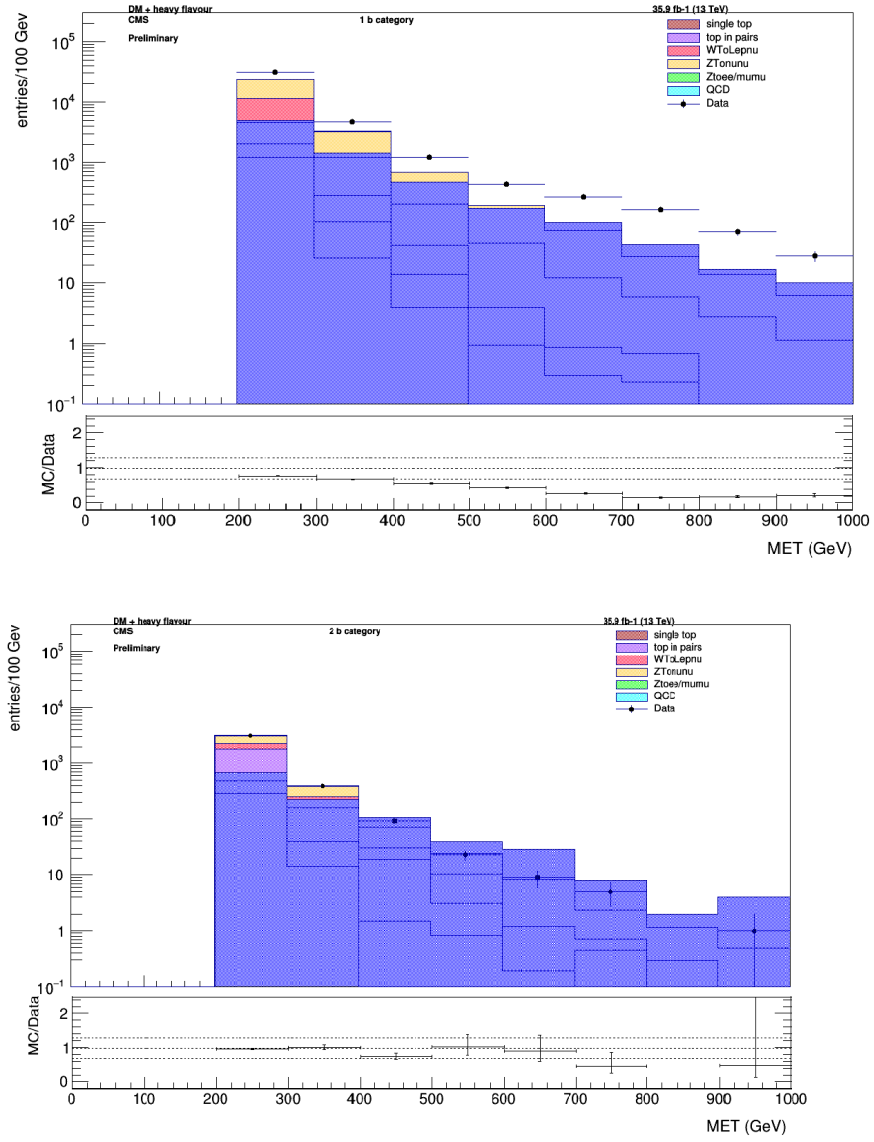

Figure 3.40: Distribution of E_T^{miss} for the MC sample simulating the presence of a fermionic DM particle with a scalar mediator of mass $M_\Phi = 10$ TeV, superimposed in blue color to the plots in Figure 3.33. The sample with the fermionic DM is plotted in arbitrary units.

Conclusions

The purpose of this work was to analyze the CMS data possibly linked to a dark matter signature that were collected in 2016 Run at LHC, and which had never been analyzed before. The data taking reached a luminosity of 35.9 fm^{-1}. which is ~ 16 times higher than the luminosity in the previous study of the CMS collaboration of 2016, and could in principle provide a much better statistics. However, this work was only a first glance at the dataset, and does not claim to be as exhaustive as the CMS Collaboration analysis at all.
During this preliminary analysis a selection of objects to consider was operated, cleaning the jets in order to avoid misidentified objects and filtering the leptons and photons, aiming at keeping only good quality ones. Nevertheless, while the cleaned jet number seem to produce a distribution close to the expected one, the leptons caused some troubles when it came to select events in the Z, W and top control regions: when a veto was applied on additional "good" leptons (other than the requested two muons, one muons, and one muon and one electron respectively), the number of events was much smaller than expected, and even smaller than the number obtained in the CMS 2016 analysis at lower luminosity, which applied the veto, too; the problem was not there when the signal region was considered. Despite looking for possible flaws in the selection codes, the reason for this drastic reduction of events has not been understood yet; to carry out the analysis the control region was investigated without requesting any veto on additional charged leptons/photons. However, probing this effect would be fundamental to continue the analysis.
When the signal region was studied, despite the MC and the data samples seemed to be in good agreement in the control regions after the renormalization process, an excess of events was observed for the 1 b tag selection. Since the study of systematics has not been performed yet, it would be interesting to deepen this part in further analysis. In the case no new physics was found when the systematics are considered, the goal of this kind of analysis would be to set a new exclusion limit for the DM production.
The missing transverse energy distribution in the signal region was finally compared to two models of DM with two different mass mediator, 100 GeV and 10 TeV; the model with the 10 TeV mediator seems to reproduce better

the data trend, if the excess was not excluded by more thorough analyses in the future.

Bibliography

[1] Abazajian, K., Koushiappas, S. M., 2006, Phys.Rev. D74 023527

[2] Abazajian, K. N., and 186 additional authors, 2012, arXiv:1204.5379

[3] Abdurashitov, J. N., et al., 2006, Phys. Rev. C 73, 045805

[4] Abercrombie et al., 2015, arXiv:1507.00966v1

[5] Aguilar, M. et al. (AMS Collaboration), 2013, Phys. Rev. Lett. 110, 141102

[6] Albert, A., Bauer, M., Brooke, J., Buchmueller, O., Cerdeno, D. G., Citron, M., et al., 2017, Phys. Dark Univ. 16, 49-70.

[7] Alcock, C., 2000, Science, Vol. 287, Issue 5450, pp. 74-79

[8] Alcock, C., Allsman, R. A., Alves, D. R., Axelrod, T. S., Becker, A. C., Bennett, D. P., Cook, K. H., Dalal, N., Drake, A. J., Freeman, K. C., Geha, M., Griest, K., Lehner, M. J., Marshall, S. L., Minniti, D., Nelson, C. A., Peterson, B. A., Popowski, P., Pratt, M. R., Quinn, P. J., Stubbs, C. W., Sutherland, W., Tomaney, A. B., Vandehei, T., & Welch, D., 2000, ApJ , 542, 281

[9] Alcock, C., Allsman, R. A., Alves, D. R., Axelrod, T. S., Becker, A. C., Bennett, D. P., Cook, K. H., Dalal, N., Drake, A. J., Freeman, K. C., Geha, M., Griest, K., Lehner, M. J., Marshall, S. L., Minniti, D., Nelson, C. A., Peterson, B. A., Popowski, P., Pratt, M. R., Quinn, P. J., Stubbs, C. W., Sutherland, W., Tomaney, A. B., Vandehei, T., & Welch, D., 2001, ApJ, 550, 169-172

[10] Asztalos, S. J., Rosenberg, L. J, van Bibber, K., Sikivie, P., Zioutas, K., 2006, Annual Review of Nuclear and Particle Science , Volume 56, 293-326

[11] Beaudette, F., 2014, arXiv:1401.8155

[12] Bellomo, N., Bernal, J. L., Raccanelli, A., & Verde, L., 2018,

[13] Bernabei, R., Belli, P., Bussolotti, A., Cappella, F., Caracciolo, V., Cerulli, R., Dai, C. J., d'Angelo, A., Di Marco, A., He, H. L., Incicchitti, A., Ma, X. H., Mattei, A., Merlo, V., Montecchia, F., Sheng, X. D. & Ye, Z. P., 2018, arXiv:1805.10486

[14] Bernabei, R., Belli, P., Cappella, F., Cerulli, R., Dai, C. J., Kuang, H. H., Incicchitti, A., Ma, J. M., Montecchia, F., Nozzoli, F., Prosperi, D. & Ye, Z. P., 2003, Riv. N. Cim. 26 n.1, 1-73

[15] Bertone, G., 2010, *Particle Dark Matter: observations, models and searches*, Cambridge University Press

[16] Bird, S., Cholis, I., Muñoz, J. B., Ali-Haïmoud, Y., Kamionkowski, M., Kovetz, E. D., Raccanelli, A., & Riess, A. G., 2016, Phys. Rev. Lett. 116, 201301

[17] Bocci, A., 2016, *Triggers for LHC*, Summer Student Lecture Programme Course, https://cds.cern.ch/record/2201478

[18] Bovy, J. & Tremaine, S., 2012, The Astrophysical Journal, Volume 756, Number 1

[19] Bringmann, T., Hasenkamp, J., & Kersten, J., 2014, JCAP07 042

[20] Bernabei, R., Belli, P., Cappella, F., Caracciolo, V., Castellano, S., Cerulli, R., Dai, C. J., d'Angelo, A., d'Angelo, S., Di Marco, A., He, H. L., Incicchitti, A., Kuang, H. H., Ma, X. H., Montecchia, F., Prosperi, D., Sheng, X. D., Wang, R. G. & Ye, Z. P., 2013, Eur. Phys. J. C, 73: 2648

[21] Buchmueller, O., Doglioni, C. & Wang, L.T., 2017, Nature Physics volume 13, pages 217-223

[22] Cirelli, M., darkuniverse.uni-hd.de/pub/Main/WinterSchool12Slides/CirelliDM_1.pdf (link consulted on 24th May 2018)

[23] Clowe, D., Bradac, M., Gonzalez, A. H., Markevitech, M., Randall, S. W., Jones, C., & Zaritsky, D. , 2006, Astrophysical Journal, 648(2 II).

[24] CMS Collaboration & LHCb Collaboration, 2015, Nature. 522, 7554, p. 68-72

[25] CMS Collaboration, 2008, JINST 3 S08004, doi:10.1088/1748-0221/3/08/S08004

[26] CMS Collaboration, 2016, *Search for dark matter in final states with an energetic jet, or a hadronically decaying W or Z boson using 12.9 fb^{-1} of data at $\sqrt{s} = 13$ TeV*, CMS PAS EXO-16-037

[27] CMS Collaboration, 2016, *Search for Dark Matter produced in association with bottom quarks*, CMS-PAS-B2G-15-007

[28] CMS Collaboration, 2017, *The CMS Trigger System*, JINST 12 P01020

[29] CMS Colalboration, 2017, *Particle-flow reconstruction and global event description with the CMS detector*, JINST 12 P10003

[30] CMS Collaboration, 2018, *Identification of heavy-flavour jets with the CMS detector in pp collisions at 13 TeV*, JINST 13 P05011

[31] cms.web.cern.ch/news/detector-overview (link consulted on 02nd June 2018)

[32] Cooley, J., 2014, Phys. Dark Univ. volume 4, Sept. 2014, pages 92-97

[33] Dvali, G., 2013, 6th CERN - Latin-American School of High-Energy Physics, Natal, Brazil, 23 Mar - 5 Apr 2011, pp.145-156 (CERN-2013-003)

[34] Essig, R., Jaros, J. A. Wester, W., Hansson A. P., Andreas, S., Averett, T., Baker, O., Batell, B., Battaglieri, M., Beacham, J., Beranek, T., Bjorken, J. D., Bossi, F., Boyce, J. R., Cates, G. D., Celentano, A., Chou, A. S., Cowan, R., Curciarello, F., Davoudiasl, H., deNiverville, P., De Vita, R., Denig, A., Dharmapalan, R., Dongwi, B., Döbrich, B., Echenard, B., Espriu, D., Fegan, S., Fisher, P., Franklin, G. B., Gasparian, A., Gershtein, Y., Graham, M., Graham, P. W., Haas, A., Hatzikoutelis, A., Holtrop, M., Irastorza, I., Izaguirre, E., Jaeckel, J., Kahn, Y., Kalantarians, N., Kohl, M., Krnjaic, G., Kubarovsky, V., Lee, H-S., Lindner, A., Lobarov, A., Marciano, W. J., Marsh, D. J. E., Maruyama, T., McKeen, D., Merkel, H., Moffeit, K., Monaghan, P., Mueller, G., Nelson, T. K., Neil, G. R., Oriunno, M., Pavlovic, Z., Phillips, S., K., Pivovaroff, M. J., Poltis, R., Pospelov, M., Rajendran, S., Redondo, J., Ringwald, A., Ritz, A., Saenboonruang, K., Shuster, P., Shinn, M., Slatyer, T. R., Steffen, J. H., Stepanyan, S., Tanner, D. B., Thaler, J., Tobar, M. E., Toro, N., Upadye, A., Van de Water, R., Vlahovic, B., Vogel, J. K., Walker, D., Weltman, A., Wojtekhowski, B., Zhang, S., & Zioutas, K., 2013, arXiv:1311.0029

[35] Feng, J. L., 2010, arXiv:1003.0904v2

[36] Fermilab website, https://web.fnal.gov/organization/SCS/SitePages/Home.aspx (link consulted on 2nd December 2018)

[37] Frixione, S., Nason, P., & Oleari, C., 2007, arXiv:0709.2092

[38] Geant4 website, geant4.web.cern.ch/

[39] Gelmini, G. B., 2015, arXiv:1502.01320v2

[40] Grachov, O. A., Murray, M. J., Ayan, A. S., Debbins, P., Norbeck, E., Onel, Y., & d'Enterria, D., 2006, AIPConf.Proc.867:258-265

[41] Green, A. M., 2014, arXiv:1403.1198 [gr-qc]

[42] Gunnellini, P., 2013, Proceeding for the 41st ITEP school in Moscow, arXiv:1304.2943

[43] http://people.roma2.infn.it/∼dama/web/ind_nai.html (link consulted on 30th June 2018)

[44] Hu, W., http://background.uchicago.edu/∼whu/intermediate/driving2.html (link consulted on 18th February 2018)

[45] Irastorza, I. G., & Redondo, J., 2018, arXiv:1801.08127v2

[46] LIGO Scientific Collaboration & Virgo Collaboration, 2016, Phys. Rev. Lett. 116, 061102

[47] LIGO Scientific Collaboration & Virgo Collaboration, 2017, Phys. Rev. Lett., 118(22):221101

[48] LSND Collaboration, 2001, Phys.Rev.D64:112007

[49] Malik, S. A., 2012, *Search for Dark Matter at the LHC using Missing Transverse Energy* , presentation at 47th Rencontres de Moriond, Cosmology, La Thuile, Italy, March 10 - 17, 2012

[50] Marshall, Z., 2014, *Defending Your Life (Parts 1, 2 and 3)*, https://atlas.cern/updates/atlas-blog/defending-your-life-part-1 and related links for parts 2 and 3 (link consulted on 2nd December 2018)

[51] Messina, M., 2017, PoS NOW2016, 080.

[52] MiniBooNE Collaboration, 2013, Phys. Rev. Lett. 110, 161801

[53] MiniBooNE DM Collaboration, 2018, arXiv:1807.06137v1

[54] NANOAOD variables webpage, https://cms-nanoaod-integration.web.cern.ch/integration/master/mc80X_doc.html (link consulted several times during the work)

[55] Parker, B. R., *Invisible Matter and the Fate of the Universe*, 1989, Springer US

[56] Peccei, R. D. & Quinn, H. R., 1977, Physical Review Letters 38(25):1440-1443

[57] Planck Collaboration, 2015, arXiv:1502.02114

[58] Planck Collaboration, 2016, A&A 594, A13

[59] Raffelt, G.G., 2008, *Astrophysical Axion Bounds*. In: Kuster M., Raffelt G., Beltrán B. (eds) Axions. Lecture Notes in Physics, vol 741. Springer, Berlin, Heidelberg

[60] Redondo, J., 2017, *Dark Matter and Axions*, ICTP Summer School on Particle Physics, http://indico.ictp.it/event/7968/session/80/contribution/310/material/slides/

[61] Rubin, V. C. & Ford, W. K. Jr., 1970, Astrophysical Journal, vol. 159, p.379

[62] Schneider, P., *Extragalactic Astronomy and Cosmology*, 2006, Springer-Verlag Berlin Heidelberg

[63] Schwarzmeier, J., https://kof.zcu.cz/st/dis/schwarzmeier/galaxy_models.html (link consulted on 12th February 2018)

[64] Sjöstrand, T., Ask, S., Christiansen, J. R., Corke, R., Desai, N., Ilten, P., Mrenna, S., Prestel, S., Rasmussen, C. O., & Skands, P. Z., 2014, arXiv:1410.3012

[65] Tang, Y., 2016, J. Phys.: Conf. Ser. 718 042056

[66] Turner, M. S., 1990, Physics Reports, Volume 197, Issue 2, Pages 67-97

[67] Undagoitia, T. M. & Rauch, L., 2017, arXiv:1509.08767v2

[68] Wagoner, R. V., Fowler, W. A.& Hoyle, F., 1967, Astrophysical Journal, vol. 148, p.3

[69] Wambsganss, J., 2006, arXiv:astro-ph/0604278

[70] Wantz, O., & Shellard, E.P.S., 2010, Phys.Rev.D82:123508, arXiv:0910.1066v3

[71] Webber, B., 2017, *Introduction to Monte-Carlo Techniques*, Summer Student Lecture Programme Course, https://cds.cern.ch/record/2276330?ln=it and https://cds.cern.ch/record/2276454?ln=it

[72] Weinberg, S., 1978, Phys. Rev. Lett. 40 223

[73] Wilczek, F., 1978, Phys. Rev. Lett. 40 279

[74] XENON collaboration, 2015, Phys. Rev. Lett. 115, 091302

[75] Xenon1T website, http://www.xenon1t.org/, (link consulted on 30th June 2018)

[76] Zwicky, F., 1933, Helvetica Physica Acta, Vol. 6, p. 110-127